

**ISTANBUL TECHNICAL UNIVERSITY ★ GRADUATE SCHOOL OF SCIENCE**  
**ENGINEERING AND TECHNOLOGY**

**AN OBSERVATIONAL STUDY OF  
ACCRETING MILLISECOND X-RAY PULSARS:  
FROM ACCRETION TO THE ROTATION POWERED STAGES**

**Ph.D. THESIS**

**Can GÜNGÖR**

**Department of Physics Engineering**

**Physics Engineering Programme**

**Thesis Advisor: Prof. Dr. Kazım Yavuz EKŞİ**

**SEPTEMBER 2016**



**ISTANBUL TECHNICAL UNIVERSITY ★ GRADUATE SCHOOL OF SCIENCE**  
**ENGINEERING AND TECHNOLOGY**

**AN OBSERVATIONAL STUDY OF  
ACCRETING MILLISECOND X-RAY PULSARS:  
FROM ACCRETION TO THE ROTATION POWERED STAGES**

**Ph.D. THESIS**

**Can GÜNGÖR  
(509092102)**

**Department of Physics Engineering**

**Physics Engineering Programme**

**Thesis Advisor: Prof. Dr. Kazım Yavuz EKŞİ**

**Co-advisor: Prof. Dr. Ersin GÖĞÜŞ**

**SEPTEMBER 2016**



**MİLİSANIYE X-IŞINI PULSARLARININ  
GÖZLEMSEL OLARAK İNCELENMESİ:  
KÜTLE AKTARIM EVRESİNDEN RADYO PULSARI EVRESİNE**

**DOKTORA TEZİ**

**Can GÜNGÖR  
(509092102)**

**Fizik Mühendisliği Anabilim Dalı**

**Fizik Mühendisliği Programı**

**Tez Danışmanı: Prof. Dr. Kazım Yavuz EKŞİ  
Eş Danışman: Prof. Dr. Ersin GÖĞÜŞ**

**EYLÜL 2016**



Can GÜNGÖR, a Ph.D. student of ITU Graduate School of Science Engineering and Technology 509092102 successfully defended the thesis entitled “AN OBSERVATIONAL STUDY OF ACCRETING MILLISECOND X-RAY PULSARS: FROM ACCRETION TO THE ROTATION POWERED STAGES”, which he prepared after fulfilling the requirements specified in the associated legislations, before the jury whose signatures are below.

**Thesis Advisor :**      **Prof. Dr. Kazım Yavuz EKŞİ** .....  
Istanbul Technical University

**Co-advisor :**      **Prof. Dr. Ersin GÖĞÜŞ** .....  
Sabancı University

**Jury Members :**      **Prof. Dr. Ahmet Togo GİZ** .....  
Istanbul Technical University

**Assoc. Prof. Abdurrahman Savaş ARAPOĞLU** .....  
Istanbul Technical University

**Prof. Dr. Neşe ÖZDEMİR** .....  
Istanbul Technical University

**Assoc. Prof. Tolga GÜVER** .....  
Istanbul University

**Assoc. Prof. Ünal ERTAN** .....  
Sabancı University

**Date of Submission :**    **15 August 2016**

**Date of Defense :**      **02 September 2016**







*To my family,*



## FOREWORD

After few years of strict studies and researches, I am at the end of my Ph.D. In this thesis, I would like to make albeit a tiny contribution to neutron star science using accreting millisecond X-ray pulsars. But first of all, before all scientific sentences, paragraphs, figures and tables, I would like to express my appreciation to my supervisor Prof. Dr. Kazım Yavuz EKŞİ. When I began to do my Ph.D. as a student who is motivated but far from the subject, he was the one who taught me not only the science, the knowledge and the methodology but also to be an academician respects ethical values.

I would like to extend my thanks to my co-advisor Prof. Dr. Ersin GÖĞÜŞ and Assoc. Prof. Tolga GÜVER for teaching me how observational studies in X-ray band are done and for their everlasting patience on me while working together. I could make my thesis real under favour of them.

I am obligated to Scientific and Technological Research Council of Turkey (TUBITAK) for supporting me as Ph.D student scholar with the project number of 108T210 and 112T105.

During the last year of my Ph.D period, I have worked in Astrophysical Institute and University Observatory, Jena University, Germany, supported by the 2214/A Scholarship of TUBITAK. Hereby, I am grateful to Prof. Ralph NEUHÄUSER and Dr. Valeri HAMBARYAN for letting me have the chance of working together. I also thank TUBITAK for giving this opportunity to me. This Ph.D. Thesis is funded by Scientific Research Projects Unit (BAP) with the project number 38339. I am thankful to BAP.

Last but not least, I would like to thank my parents Jale & Ateş GÜNGÖR and my sister Eda GÜNGÖR for their enormous and unceasing support. I could clearly say that I would never finish this thesis without the feeling of their backing.

September 2016

Can GÜNGÖR  
M.Sc.



## TABLE OF CONTENTS

	<u>Page</u>
<b>FOREWORD.....</b>	<b>ix</b>
<b>TABLE OF CONTENTS.....</b>	<b>xi</b>
<b>ABBREVIATIONS .....</b>	<b>xiii</b>
<b>SYMBOLS.....</b>	<b>xv</b>
<b>LIST OF TABLES .....</b>	<b>xvii</b>
<b>LIST OF FIGURES .....</b>	<b>xix</b>
<b>SUMMARY .....</b>	<b>xxi</b>
<b>ÖZET .....</b>	<b>xxiii</b>
<b>1. INTRODUCTION TO NEUTRON STARS .....</b>	<b>1</b>
1.1 Introduction .....	1
1.2 Mass – Radius Relation.....	1
1.3 Neutron Star Family .....	2
1.4 X-ray Binaries .....	3
1.4.1 Roche lobe geometry.....	4
1.4.2 The Eddington limit.....	5
1.4.3 High mass X-ray binaries .....	6
1.4.4 Low mass X-ray binaries.....	6
1.4.5 Accreting millisecond X-ray pulsars .....	7
<b>2. X-RAY OBSERVATORIES AND DATA ANALYSIS.....</b>	<b>11</b>
2.1 X-ray Missions .....	11
2.2 The Rossi X-ray Timing Explorer .....	11
2.3 The Swift Gamma-Ray Burst Mission .....	12
<b>3. CLASSIFICATION AND SPECTRAL EVOLUTION OF OUTBURSTS ...</b>	<b>15</b>
3.1 Introduction .....	15
3.2 Classification of Outbursts of Aql X-1 .....	16
3.3 Observation and Data Analysis .....	20
3.4 Discussion.....	24
3.4.1 Is the quiescent stage duration related to the different outburst classes?	24
3.4.2 Transition to the propeller stage as the cause of the rapid decay stage ..	24
3.4.3 Irradiation as the parameter inducing different outburst durations and peak fluxes .....	27
3.4.4 Implications of spectral analysis .....	28
<b>4. PARTIAL ACCRETION IN THE PROPELLER STAGE OF AMXPS.....</b>	<b>33</b>
4.1 Introduction .....	33
4.2 Observation and Data Analysis .....	35
4.2.1 Model I: Black body assumption.....	36
4.2.2 Model II: Comptonised black body assumption.....	40

4.3 The Partial Accretion Regime of Outbursts.....	41
4.4 Applications.....	44
4.5 Results and Discussion .....	45
<b>5. CONCLUSION .....</b>	<b>47</b>
<b>REFERENCES.....</b>	<b>49</b>
<b>APPENDICES .....</b>	<b>57</b>
<b>CURRICULUM VITAE.....</b>	<b>66</b>



## ABBREVIATIONS

<b>AMXP</b>	: Accreting Millisecond X-ray Pulsar
<b>ASM</b>	: All-Sky Monitor
<b>BAT</b>	: Burst Alert Telescope
<b>BH</b>	: Black Hole
<b>CCO</b>	: Central Compact Object
<b>DIM</b>	: Disk Instability Model
<b>EoS</b>	: Equation of State
<b>ESA</b>	: European Space Agency
<b>FRED</b>	: Fast Rise Exponential Decay
<b>HETE</b>	: High Energy Transient Explorer
<b>HEXTE</b>	: High Energy X-ray Timing Experiment
<b>HMXB</b>	: High Mass X-ray Binary
<b>HS</b>	: High/Soft
<b>INS</b>	: Isolated Neutron Star
<b>ISS</b>	: International Space Station
<b>LH</b>	: Low/Hard
<b>LIS</b>	: Low Intensity State
<b>LMXB</b>	: Low mass X-ray binary
<b>MAXI</b>	: Monitor of All Sky X-ray Image
<b>MSP</b>	: Millisecond Pulsar
<b>NASA</b>	: National Aeronautics and Space Administration
<b>NS</b>	: Neutron Star
<b>PCA</b>	: Proportional Counter Array
<b>PCU</b>	: Proportional Counter Unit
<b>RPP</b>	: Rotation Powered Pulsar
<b>RXTE</b>	: Rossi X-ray Timing Explorer
<b>SWIFT</b>	: Swift Gamma-ray Burst Mission
<b>SXT</b>	: soft X-ray Transient
<b>WD</b>	: White Dwarf
<b>XRT</b>	: X-ray Telescope
<b>XSPEC</b>	: X-ray Spectral Fitting Package





## SYMBOLS

$\mathbf{R}_c$	: Corotation radius
$\phi_{\mathbf{R}}(\mathbf{r})$	: Critical Potential
$\rho$	: Density
$\dot{\mathbf{M}}$	: Accretion rate
$\omega_*$	: Fastness parameter
$\mathbf{F}$	: Flux; Force
$\mathbf{G}$	: Gravitational constant; Gauss
$\mathbf{l}_h$	: Hard photon compactness
$\mathbf{T}_{\text{diskbb}}(\mathbf{R}_{\text{in}})$	: Inner disk temperature of the disk black body component
$\mathbf{R}_{\text{in}}$	: Inner radius of the disk
$\Omega_K$	: Keplerian angular velocity
$\mathbf{L}$	: Luminosity; Lagrange point
$\mu$	: Magnetic dipole moment
$\mathbf{f}$	: Mass fraction rate
$\mathbf{m}_p$	: Mass of proton
$\mathbf{m}$	: Mass; magnitude
$\mathbf{N}_H$	: Neutral hydrogen column density
$\kappa$	: Opacity
$\tau$	: Optical depth of the corona
$\omega_{\text{orb}}$	: Orbital angular velocity
$\mathbf{P}_b$	: Orbital period
$\mathbf{E}_{\text{pivot}}$	: Pivot energy
$\mathbf{P}$	: Pressure
$\mathbf{P}_{\text{rad}}$	: Radiation pressure
$\mathbf{r}$	: Radius
$\mathbf{R}_L$	: Radius of the light cylinder
$\varepsilon$	: Rest mass energy
$\mathbf{H}$	: Scale-height
$\mathbf{k}_B \mathbf{T}_{\text{bb}}$	: Seed photon temperature
$\mathbf{l}_s$	: Soft photon compactness
$\mathbf{M}_{\odot}$	: Solar mass
$\mathbf{c}$	: Speed of light
$\nu_s$	: Spin frequency
$\mathbf{T}_{\text{bb}}$	: Temperature of the black body component
$\sigma_T$	: Thomson cross-section
$\mathbf{t}_v$	: Time-scale of the outburst decay
$\mathbf{f}_x$	: X-ray mass function



## LIST OF TABLES

	<u>Page</u>
<b>Table 1.1</b> : Accreting millisecond X-ray pulsars.....	<b>9</b>
<b>Table A.1</b> : Best fit parameters of EQPAIR model and the Gaussian line for the 2000 outburst. ....	<b>58</b>
<b>Table A.2</b> : Same as Table A.1 but for the 2010 outburst. ....	<b>59</b>
<b>Table A.3</b> : Same as Table A.1 but for the 2011 outburst. ....	<b>59</b>
<b>Table B.1</b> : Best fit parameters of <i>black body + disk black body + Gauss</i> model for the 2000 outburst of RXTE/PCA data.....	<b>61</b>
<b>Table B.2</b> : Same as Table B.1 but for the 2011 outburst.....	<b>62</b>
<b>Table C.1</b> : Best fit parameters of <i>black body radiation + comptonisation</i> + <i>disk black body + Gauss</i> model for the 2000 outburst of RXTE/PCA data.....	<b>63</b>
<b>Table C.2</b> : Same as Table C.1 but for the 2011 outburst.....	<b>63</b>



## LIST OF FIGURES

	<u>Page</u>
<b>Figure 1.1</b> : A schematic view of NS structure .....	2
<b>Figure 1.2</b> : Mass – radius relation of NSs.....	3
<b>Figure 1.3</b> : Roche potential of a binary system.....	4
<b>Figure 2.1</b> : The Rossi X-ray Timing Explorer. ....	12
<b>Figure 2.2</b> : The Swift Gamma-Ray Burst Telescope. ....	13
<b>Figure 3.1</b> : Long term light curve of Aql X–1 using ASM and MAXI data.....	17
<b>Figure 3.2</b> : ASM and MAXI lightcurves of outbursts and their time derivative..	18
<b>Figure 3.3</b> : The outbursts in the counts/s versus counts/s/day “phase space”.....	19
<b>Figure 3.4</b> : The long-term evolution of Aql X–1 as observed by MAXI between June 2010 to January 2012. ....	21
<b>Figure 3.5</b> : The X-ray spectrum (Obs ID 96440-01-03-04) in the energy range of 3.0 – 30.0 keV.....	22
<b>Figure 3.6</b> : Spectral evolution of Aql X–1 during 2000, 2010 band 2011 outbursts.....	23
<b>Figure 3.7</b> : Outer disk radius versus the peak count-rate of outbursts of Aql X–1.	28
<b>Figure 3.8</b> : Evolution of the scattering optical depth of the corona as a function of unabsorbed source flux.....	29
<b>Figure 3.9</b> : The relation between the compactness parameter $l_h/l_s$ and the optical depth of the corona.....	30
<b>Figure 3.10</b> : Variation of unabsorbed flux of the Gaussian iron line component as a with the EQPAIR model flux. ....	30
<b>Figure 4.1</b> : The X-ray spectrum of Aql X–1 during outburst. ....	36
<b>Figure 4.2</b> : Evolution of spectral parameters during 2000 outburst of Aql X–1.	37
<b>Figure 4.3</b> : Same as Figure 4.2 but for the proportional counter array (RXTE/PCA) data during 2011 outburst of Aql X–1. ....	39
<b>Figure 4.4</b> : the Swift gamma-ray burst mission/X-ray telescope (SWIFT/XRT) light curve of the 2013 outburst of Aql X–1. The time evolution of hardness parameter. ....	40
<b>Figure 4.5</b> : X-ray light curves of the 1997, the 2010, the 2000 and the 2013 outbursts together with the best fit of Eq.4.5 between maximum of outbursts and the knee.....	43
<b>Figure 4.6</b> : X-ray light curves of black body component of the 2000, the 2011 and the 2013 outbursts together with the best fit of Eq.4.5 between the maximum and the knee. ....	44
<b>Figure 4.7</b> : $\dot{M}_*/\dot{M}$ vs the fastness parameter relation of the outbursts of Aql X–1.....	45



**AN OBSERVATIONAL STUDY OF  
ACCRETING MILLISECOND X-RAY PULSARS:  
FROM ACCRETION TO THE ROTATION POWERED STAGES**

**SUMMARY**

Low-mass X-ray binaries (LMXBs) are systems containing a compact object—a white dwarf, a neutron star (NS) or a black hole—and a low mass companion ( $M_c \lesssim 1 M_\odot$ ). The luminosity that we observe, originates mainly from accretion onto the surface of the compact object via Roche lobe overflow from the low mass companion, also called donor star. Since the transferred material has angular momentum due to the rotation of the donor star, the material forms an accretion disk around the compact object rather than to fall directly. Depending on the morphology of the disk angular velocity and the magnetic field of the compact object, different stages of disk – magnetosphere interaction, are expected. These stages can be summarised as; (i) The *accretion* stage in which the inner radius of the disk,  $R_{in}$ , is smaller than the corotation radius, resulting the most (if not all) of the infalling mass flux to reach to the polar cap of the NS. (ii) The *propeller* stage in which  $R_{in} > R_c$  resulting with none (if not a small fraction) of the inflowing mass to reach the surface of the NS due to centrifugal barrier formed by the rapidly rotating magnetosphere. (iii) The *radio pulsar* stage in which the  $R_{in}$  is even further away from the NS, possibly larger than the light cylinder radius. Millisecond pulsars (MSPs) are NSs with the rotation period of 1 – 10 milliseconds. These object are thought as the result of accretion in LMXBs since the material also transfers angular momentum and causes *spin up* process of the NS.

Accreting millisecond X-ray pulsars (AMXPs) which is a subclass of LMXBs are very important objects for studying the stages of disk – magnetosphere interaction as these objects may show different stages in an observable duration. AMXPs show cyclic outbursts in their X-ray light curves. A typical X-ray light curve of an outburst of an AMXP has a fast rise and an exponential decay phases. Most of the light curves show a *knee* where the flux goes from the slow decay stage to the rapid decay stage. This knee may be linked to the transition from the accretion stage to the propeller stage. Since, after the knee, the X-ray luminosity of the source is still higher than its quiescent level, the accretion from inner disk must be continuing in the propeller stage with a lower fraction than in the accretion stage. The X-ray does not only arise from accretion onto the poles but the inner parts of the disk may also contribute to the total X-ray luminosity. To infer what fraction ( $f$ ) of the inflowing matter accretes onto the NS, the emission originating from the disk should be first eliminated and a light curve of X-ray emission of the magnetic poles must be obtained.

In this study, to clarify the propeller effect and the connection between the outbursts and the stages of the disk magnetosphere interaction, firstly, outburst classes in these systems are investigated. Since one of the most well known AMXP, Aql X-1 is a very bright source in the X-ray band and has frequent outbursts ( $\sim 1$  per year), a broad classification of all outbursts detected with the all-sky monitor (ASM) on the Rossi X-ray timing explorer (RXTE) and the monitor of all sky X-ray image (MAXI) aboard

the international space station (ISS) are presented. According to new classification method based on the duration and the maximum flux, three types of outbursts of Aql X-1 are identified; *long-high*, *medium-low*, and *short-low*. Then, the trends in the “phase-space” of flux derivative versus flux to demonstrate the differences in the three identified outburst types are analysed. Also spectral modelling of the observations of Aql X-1 performed by the proportional counter array (PCA) onboard RXTE during the 2000 and the 2011 outbursts of the long-high class and the 2010 outburst of the medium-low class, are executed. As a spectrum model, a hybrid thermal/non-thermal hot plasma emission model (*EQPAIR* in XSPEC) together with a Gaussian component to model the Fe K $\alpha$  emission line is used. Time histories of the source flux and the parameters; optical depth of the corona ( $\tau$ ), the seed photon temperature ( $kT_{\text{bb}}$ ) and the hard state compactness ( $l_{\text{h}}$ ) for these three outbursts are constructed. As a result of this work, it is shown that the physical parameters of either class reaches the same values throughout the outbursts, the only difference being the maximum flux. In light of this, it is argued that irradiation is the dominant physical process leading to the different classes of outbursts.

Moreover, a new method is provided to infer the fraction of the accreting matter onto the NS pole to the mass rate transferring from outer layers of the disk to the inner disk ( $f \equiv \dot{M}_*/\dot{M}$ ), as a function of the fastness parameter ( $\omega_*$ ) from the observational data, assuming the knee in the decay phase of X-ray light curve is due to the transition from accretion to the propeller stage. In this method, X-ray luminosities are transformed to the mass fraction,  $f$ , and the time scale of outburst is converted to fastness parameter,  $\omega_*$ . It allows different types of outbursts of an AMXP to be compared in  $f - \omega_*$  space which is universal for a unique system.

All RXTE/PCA observations covering the 2000 and the 2011 outbursts and the Swift gamma-ray burst mission/X-ray telescope (SWIFT/XRT) data during the 2013 outburst of Aql X-1 are analysed using a combination of *blackbody* representing hot spot on the NS, *disk blackbody* representing the contribution of inner disk layers and a *Gaussian* model for the iron line. We obtained the X-ray light curves only due to accretion onto the poles. As a result, applying our technique,  $f = f(\omega_*)$  is obtained for the system and showed that the outbursts having different luminosities and durations follow the same trend.

The structure of this thesis is as follows: In Chapter 1, brief information about NS physics and NS family is given. The physical background of X-ray binaries and more specifically AMXPs is also presented in this section. In Chapter 2, X-ray observatories whose data are used in this study are enucleated. In Chapter 3, the classification of outbursts of AMXPs is expressed and a unique classification method developed for Aql X-1 is presented. Via spectral modelling of RXTE data for each type, differences between these types are discussed. In Chapter 4, the physics of disk – magnetosphere interaction is described and a new method is presented to explore partial accretion in the propeller stage. Applications of our method are also given in Chapter 4. Finally, all of the results are discussed and the study is concluded in Chapter 5.



**MİLİSANİYE X-IŞINI PULSARLARININ  
GÖZLEMSEL OLARAK İNCELENMESİ:  
KÜTLE AKTARIM EVRESİNDEN RADYO PULSARI EVRESİNE**

**ÖZET**

Düşük kütleli X-ışını çiftleri, bir bileşeni tıkız nesne – beyaz cüce, nötron yıldızı ya da kara delik – diğer bileşeni ise Güneş kütesinden daha düşük kütleli bir yıldız ( $M_c \lesssim 1 M_\odot$ ) olan, birbirlerine kütle çekimsel olarak bağlı ve ortak kütle merkezi etrafında dolanan çift sistemlerdir. Bu tür sistemlerde gözlenen ısıtmanın kaynağı düşük kütleli bileşenden tıkız nesne üzerine aktarılan kütlenin çekimsel potansiyel enerjisinin X-ışın akısına dönüşmesidir. Düşük kütleli yıldız, evrimi sonucunda kendi eşpotansiyel yüzeyini doldurur ve birincil Lagrange noktasından tıkız nesnenin eşpotansiyel yüzeyi içerisine madde aktarır. Bu mekanizma Roche Lob taşması olarak isimlendirilir. Kütle aktarımı yapan yıldızın kendi eksen etrafında dönmesi ve kütle merkezi etrafında dolanması kaynaklı sahip olduğu açısal momentumunun sonucu olarak, aktarılan madde doğrudan tıkız nesne üzerine düşmek yerine etrafında bir toplanma diski oluşturur. Tıkız nesnenin manyetik alanı, açısal dönme hızı ve etrafında oluşan diskin morfolojisi, kütle aktarımının gerçekleşip gerçekleşmeyeceğini veya nasıl gerçekleşeceğini belirler. Bu olguya disk–manyetosfer etkileşiminin evreleri denir. Disk–manyetosfer etkileşim evreleri şu şekilde özetlenebilir;

(i) *Kütle aktarım evresi:* Eğer toplanma diskinin iç yarıçapı,  $R_{in}$ , eşdönme yarıçapından, küçük ise madde, manyetik alan çizgilerini takip ederek nötron yıldızının manyetik kutuplarına akar.

(ii) *Pervane evresi:* Eğer diskin iç yarıçapı eş dönme yarıçapından büyük ışık silindiri yarıçapından, küçük ise diskin dış kısımlarından diskin iç kısımlarına doğru taşınan maddenin tamamı merkezkaç bariyerinden dolayı yıldız üzerine düşemez, fakat bir kısmı manyetik kutuplara akabilir. Bu aşamada yıldız üzerine düşen madde miktarı kütle aktarım aşamasına göre oldukça düşük olduğu için X-ışını akısında düşüş gözlemlenmesi beklenir.

(iii) *Radyo pulsarı evresi:* Eğer diskin iç yarıçapı ışık silindiri yarıçapından büyük ise disk ve manyetosfer arasında herhangi bir etkileşim söz konusu değildir ve kütle aktarımı gerçekleşmez. Dolayısıyla bu aşamada gelen X-ışını akısı, akan maddenin gravitasyonel enerjisi kaynaklı değildir. Bu evredeki X-ışın akısının kaynağı nötron yıldızı dönme hızının yavaşlaması yani dönme kinetik enerjisi kaybıdır.

Milisanıye Pulsarları, 1 – 10 milisanıye mertebesinde dönme dönemine sahip görece yaşlı nötron yıldızlarıdır. İzole bir nötron yıldızı oluşumundan itibaren açısal momentum kaybeder. Çift yıldız sistemlerinde ise nötron yıldızı kütle aktarımı neticesinde açısal momentum kazanır. Bu süreç, tüm yaşamı boyunca üzerine madde aktarımı gerçekleşmiş bir milisanıye pulsarının milyar yıllık evrimidir. Yıldız bu milyar yıllık evrim boyunca disk – manyetosfer etkileşim evrelerini geçirir.

Düşük kütleli X-ışın çiftlerinin bir alt dalı olan kütle aktarımlı milisanıye pulsarları, milyar yıllık bu evrim sürecini, gözlenebilir zaman aralıklarında çevrimsel olarak

tekrarladıkları için nötron yıldızı disk etkileşimin evrelerinin – *kütle aktarımı*, *pervane*, *radio pulsarı* – anlaşılması adına eşi bulunmaz birer laboratuvar niteliği taşırlar. Kütle aktarımlı milisaniye pulsarları X-ışın ışık eğrilerinde çevrimsel parlamalar gösterirler (Aql X-1 örneğinde yaklaşık her yıl bir parlama). Tipik bir çevrim, X-ışını ışık eğrisinde, sakin evre (quiescent) ve parlama (outburst) evresi olarak iki ayrı bölümden oluşur. Parlamalar, hızlı akı artışı ve üstel bir iniş kolu olarak kendini gösterirler. Çoğu parlamanın iniş kolunda akı azalış hızının birden arttığı bir kırılma mevcuttur. Bu kırılma, bazı çalışmalarda kütle aktarım aşamasından pervane aşamasına geçiş olarak yorumlanmıştır. X-ışın ışık eğrisinde görülen bu kırılmadan sonraki akı değerinin hala sakin evre akı değerinden yüksek olduğu düşünülürse madde aktarımının kütle aktarım evresindeki kadar yüksek miktarda olmasa da hala devam ettiği sonucuna varılır. Gözlenen X-ışın akısının büyük bir çoğunluğu nötron yıldızı kutuplarına akan maddenin kütle çekimsel potansiyel enerjisinden kaynaklansa da diskin iç kısımlarının da bu akıya katkısı vardır. Başka bir deyişle, gözlenen akı kutuplardan ve diskin iç kısımlarından gelen toplam akıdır. Pervane aşamasında diskin dış kısımlarından iç kısımlarına taşınan maddenin ne kadarlık bir kısmının ( $f \equiv \dot{M}_*/\dot{M}$ ) yıldızın kutuplarına yağdığının gözlemsel yollarla araştırılabilmesi için önce kutuplardan gelen akı toplam akıdan ayrıştırılarak sadece kutuplardan gelen akı için X-ışın ışık eğrisi oluşturulmalıdır.

Bu tez çalışmasında, kütle aktarımlı milisaniye pulsarlarında disk – manyetosfer etkileşim evrelerinin X-ışın ışık eğrisiyle ilişkilendirilmesi, özellikle pervane aşamasında yıldız üzerine yağın kütle miktarının diskin dış kısımlarından iç kısımlarına taşınan madde miktarına oranının hesaplanması ve farklı sistemlerde bu mekanizmanın nasıl işlediğinin araştırılması amaçlandı. İlk olarak en bilinen kütle aktarımlı milisaniye pulsarlarından biri olan Aql X-1’in parlamaları incelendi. Aql X-1, parlamaları X-ışını uyduları aracılığıyla 20 yılı aşkın bir süredir takip edilen, X-ışında parlak ve her yıl parlama gösteren bir kaynak olması sebebiyle parlama sınıflarının araştırılması için oldukça uygun bir kaynaktır. Öncelikle, *Rossi X-ray timing explorer* (RXTE) X-ışın uydusu üzerine konuşlanmış *all-sky monitor* (ASM) ve *uluslararası uzay istasyonu* (ISS) üzerine konuşlanmış *monitor of all-sky X-ray image* (MAXI) dedektörlerinden Aql X-1’a ilişkin tüm parlaklık verisi kullanılarak 20 yıllık X-ışın ışık eğrisi oluşturuldu. Daha sonra, parlamaların morfolojik olarak karşılaştırması adına, bu süreçte görülen tüm parlamalar, başlangıç zamanlarına göre kalibre edilerek üst üste çakıştırıldı. Bunun sonucunda, Aql X-1’da görülen parlamaların, *zaman – akı* uzayında geliş güzel dağılmak yerine, ulaştıkları maksimum akı değerleri ve parlama sürelerine göre üç ana sınıfta toplandıkları görüldü; (i)  $\sim 50 - 60$  gün süren ve  $\sim 37 - 61$  cnt/s akı değerine ulaşan parlamalar. (ii)  $\sim 40 - 50$  gün süren ve  $\sim 13 - 25$  cnt/s akı değerine ulaşan parlamalar. (iii)  $\sim 20$  gün süren ve  $\sim 17 - 25$  cnt/s akı değerine ulaşan parlamalar. Belirlenen bu üç sınıf arasındaki farkların daha detaylı ortaya çıkarılabilmesi için parlamaların akı değerlerinin zaman türevinin evrimi ve akı – akı türevi faz–uzayındaki davranışı incelendi. Bu sınıfların arkasındaki fizik ancak gözlemlerin detaylı analizleri sonuçları çıkarılabilir. Bu noktada, Aql X-1’in i. sınıfa ait 2000 ve 2011 parlamalarının ve ii. sınıfa ait 2010 parlamasının RXTE/*proportional counter array* (PCA) verisinin tayfsal analizi yapıldı. Tayf modeli olarak XSPEC tayf analiz programında tanımlı olan, ısısal ve ısısal olmayan sıcak plazma salmasını birlikte temsil eden EQPAIR modeli kullanıldı. Bu modele ayrıca, salma demir (Fe K $\alpha$ ) çizgisini temsil eden Gauss bileşeni eklendi. Tayf analizi sonucunda bu üç parlamanın ışık eğrisi ve

modelde kullanılan serbest parametrelerin – korona optik derinliği ( $\tau$ ), kaynak foton karacisim sıcaklığı ( $kT_{bb}$ ) ve X-ışın sertlik oranı ( $I_h$ ) – zaman içerisindeki evrimleri elde edildi. Bu çalışmanın sonucunda, maksimum akı değerleri ve süreleri farklı olan bu üç parlama grubu için, fiziksel parametrelerin zaman içerisinde aynı trendi takip ettikleri görüldü. Bu bilginin ışığında farklı sınıflara ait parlamaların aynı fiziksel olgunun farklı şiddetlerde gerçekleştiği sonucuna ulaşıldı.

Bu tez çalışmasında ayrıca, disk – manyetosfer etkileşim evrelerinden pervane evresine yoğunlaşıldı ve parlamaların X-ışın ışık eğrileri iniş kolunda görülen kırılmanın kütle aktarımı aşamasından pervane aşamasına geçiş olduğu kabulü yapılarak, bu evrede yıldız üzerine yağın madde miktarının diskin iç kısımlarına aktarılan madde miktarına oranını, sadece, yıldızın dönme frekansının diskin iç kısımlarındaki Kepler frekansına oranı olan boyutsuz bir parametreye (*dönme hızı* parametresi,  $\omega_*$ ) bağlı bir fonksiyon olarak ( $f = \dot{M}_*/\dot{M} = f(\omega_*)$ ) belirlenmesini sağlayan bir yöntem geliştirildi. Bu yöntemde, X-ışın ısıtma değerleri kütle oranı  $f$ 'e, parlamanın zaman ölçeği ise dönme hızı parametresine dönüştürülerek parlamanın ışık eğrisi birimsiz  $f - \omega_*$  uzayında temsil edildi. Bu da, farklı maksimum parlaklık değeri ve farklı sürelerle sahip parlamaların karşılaştırılabilmesi olanağı sağlamaktadır.

Bu tez çalışması kapsamında, Aql X-1'in 2000 ve 2011 parlamalarının RXTE/PCA dedektöründen alınan verisinin ve 2013 parlamasının *Swift gamma-ray burst mission/X-ray telescope* (SWIFT/XRT) dedektöründen alınan verisinin tayfsal analizi yapıldı. Tayf modeli olarak, manyetik kutuplardan gelen akıyı temsil eden *karacisim*, ısıtılmış diskin iç bölgesinden gelen katkıyı temsil eden *disk karacisim* ve demir çizgisini temsil eden *Gauss* modellerinin kombinasyonu kullanılarak sadece manyetik kutuplardan, başka bir deyişle sadece yıldız yüzeyine akan maddenin kütleçekimsel potansiyel enerjisinden kaynaklı akı için ışık eğrisi oluşturuldu. Elde edilen bu ışık eğrilerine geliştirdiğimiz model uygulanarak bu üç parlama için  $f = f(\omega_*)$  elde edildi ve sonuç olarak farklı şiddet ve sürelerde gerçekleşen bu üç parlamanın  $f - \omega_*$  uzayında aynı evrimi geçirdikleri ve tek bir sistem için  $f$  fonksiyonunun evrensel bir fonksiyon olması gerektiği tartışıldı.

Bu tez çalışmasının planı şu şekildedir: 1. bölümde nötron yıldızları, nötron yıldızı ailesi, X-ışın çiftleri ve daha spesifik olarak kütle aktarımlı milisaniye pulsarlarının fiziksel yapısı hakkında temel bilgi verildi. 2. bölümde ise bu tez çalışması kapsamında verileri kullanılan X-ışın gözlemevleri tanıtıldı. 3. bölümde milisaniye X-ışını pulsarlarında görülen parlamaların kaç farklı şekilde gerçekleştiği incelendi ve Aql X-1'in parlamaları için geliştirilen yeni bir sınıflama tanıtıldı. Bu konuda ayrıca, tayfsal modelleme yardımıyla farklı sınıfların arasındaki fiziksel ilişkiler araştırıldı. 4. bölümde, pervane aşamasında nötron yıldızının manyetik kutuplarına yağın madde miktarının gözlemsel yöntemlerle hesaplandığı yeni bir yöntem tanıtıldı ve bu yöntemin farklı parlamalara uygulamaları sunuldu. Son olarak, elde edilen tüm bulgular ve araştırılan yöntemler 5. bölümde özetlendi.



# 1. INTRODUCTION TO NEUTRON STARS

## 1.1 Introduction

Neutron stars (NSs) are the most impressive objects in the universe with very high internal densities as exceeding  $10^{15} \text{ g/cm}^3$  that is much higher than experimental limits. They are formed in core-collapse supernova explosions. A typical NS has a radius of  $\sim 10 \text{ km}$  and a mass of  $\sim 1.5$  solar masses ( $M_{\odot}$ ) [1].

One year after the existence of neutron was discovered by Sir James Chadwick [2] in 1932, existence of NSs were proposed by Walter Baade & Fritz Zwicky as the outcome of supernova explosions [3]. Antony Hewish & Samuel Okoye discovered very high radio brightness from the center of Crab nebula and the first radio pulses by a pulsar with the period of 1.337 s were detected by Jocelyn Bell & Antony Hewish in 1967 [4]. NSs are very important objects to understand the equation of state (EoS) of ultra dense matter, superfluidity, superconductivity, strong magnetic fields, gravitational waves, X-ray binary systems and accretion mechanism etc.

## 1.2 Mass – Radius Relation

NS structure is composed of three main domains. The outermost region is the *atmosphere* which is a plasma with few millimeters thickness. Below the atmosphere, the *crust* is located which is formed of atomic nuclei, free electrons, protons and neutrons. The innermost part of a NS is the *core* which is partially understood. In Figure 1.1, a schematic view of NS structure is presented. One of the possible main contribution of NS studies to basic physics is to search for EoS in ultra high density regimes. In this point mass and radius estimations of NSs become crucial. In 1939, J. R. Oppenheimer & G. M. Volkoff [6] and independently R. C. Tolman [7] derived the hydrostatic equilibrium equation within the general relativity. This equation is called

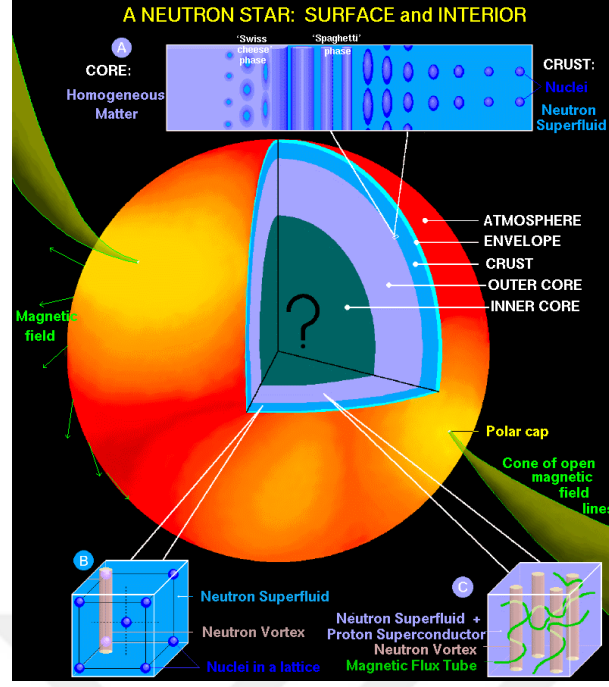


**Figure 1.1** : An schematic impression of NS structure by the Ref. [5].

TOV equation from the initials of the authors;

$$\frac{dP}{dr} = -\frac{Gm(r)\rho(r)}{r^2} \left[ 1 + \frac{4\pi r^3 P(r)}{mc^3} \right] \left[ 1 + \frac{P(r)}{\rho(r)c^2} \right] \left[ 1 - \frac{2Gm(r)}{rc^2} \right]^{-1}. \quad (1.1)$$

To calculate the total mass and the radius of a star, we add EoS;

$$P = P(\rho) \quad (1.2)$$

and the equation that describes the mass of a shell with  $dr$  thickness and  $\rho(r)$  density;

$$\frac{dm(r)}{dr} = 4\pi r^2 \rho(r) \quad (1.3)$$

to TOV equation. On the other hand, in the ultra high density regimes ( $\rho > 10^{14} \text{ gr/cm}^3$ ), the EoS is not well constrained and many different types of EoS exist in literature. In Figure 1.2, we show several mass - radius relations of NSs obtained for different EoS provided by Ref. [8].

### 1.3 Neutron Star Family

Many different classes of NSs had been identified in nature mainly categorized according to their radiation processes and spin period evolution. The largest populated NS class is the rotation powered pulsars (RPPs). They are NSs spinning down and their luminosities originates from rotational kinetic energy loss. They show pulsations

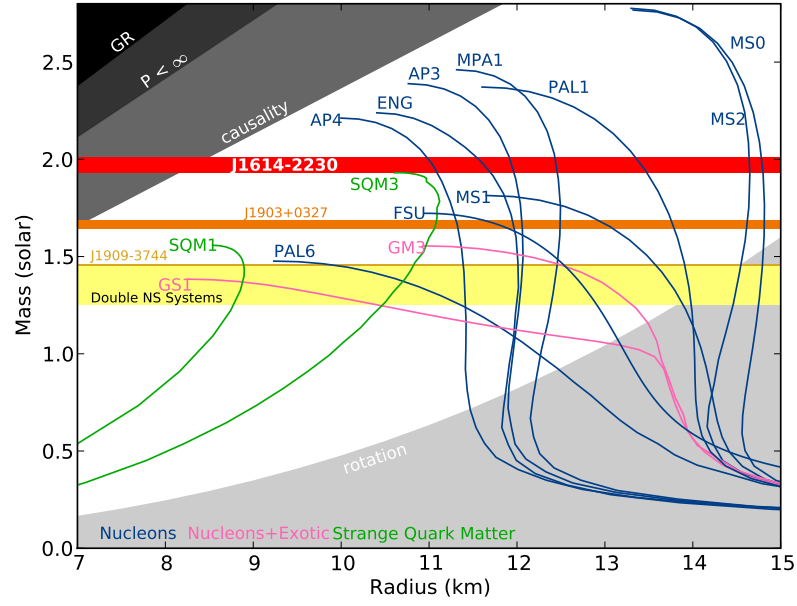


**Figure 1.2** : Mass – radius relation of NSs. from Ref. [8].

in broad band from radio to gamma ray. Another class of NSs is magnetar in which the main source of radiation is the energy stored in their very high magnetic field up to  $10^{14} - 10^{16}$  G. Bright X-ray sources with no energy release in other bands, called central compact objects (CCOs), are located close to the centers of young supernova remnants. Their periods and period derivatives were estimated indicating low magnetic fields ( $\sim 10^{10} - 10^{11}$  G). Isolated neutron stars (INSs) which show similar emission properties, only emit in the soft X-ray band with very faint optical/UV counterpart, as CCOs except that they are not situated in supernova remnants or nebulae. (see Ref. [9] for a review about NS classes).

#### 1.4 X-ray Binaries

The large majority of stars in the universe are members of binary systems. Binary systems with a compact object – black hole (BH), NS or white dwarf (WD) – radiate mainly via accreting material onto compact object from the companion, also called *donor* star, and the gravitational potential energy of the infalling material provides the observed luminosity [10]. Depending on the system configuration, accretion mechanism is wind and/or Roche lobe overflow. X-ray binaries are categorized based on the X-ray luminosity,  $L_X(2 - 10 \text{ keV})$ , in the unit of optical luminosity,  $L_{\text{opt}}(300 - 700 \text{ nm})$ , by the authors of Ref. [11]. This also indicates the mass of the

companion star. If the ratio of  $L_X(2 - 10)/L_{\text{opt}}(300 - 700)$  is fewer than 10, then, the system is named as high mass X-ray binary (HMXB) in which the companion star is an OB type star. If the ratio is greater than 10, the system is called LMXB with a lower massive companion than one solar mass ( $M_* < 1 M_{\odot}$ ).

#### 1.4.1 Roche lobe geometry

Roche lobe is a geometrical boundary of the orbiting matter in a binary system in which all points on the boundary surface have the same critical potential value. In other words, Roche lobe is the equivalent potential surface of a binary system with the critical potential in vector form;

$$\phi_R(r) = -\frac{GM_1}{|r - r_1|} - \frac{GM_2}{|r - r_2|} - \frac{1}{2}(\omega_{\text{orb}} \times r)^2. \quad (1.4)$$

where  $G$  is the gravitational constant,  $M_1$  and  $M_2$  are the masses of primary and the secondary stars, respectively,  $r_1$ ,  $r_2$  and  $r$  are the radius vectors of primary, secondary and the point on the Roche surface, based on the gravitational center, lastly  $\omega_{\text{orb}}$  is the orbital angular velocity. The first two terms of Eq.1.4 are the gravitational terms and the last is the centrifugal term. This equation describes a tear drop shape around each companion as can be seen from Figure 1.3 [12].  $L_1$ ,  $L_2$  and  $L_3$  shown in Figure 1.3 are the Lagrange points of the system in which the total force acting on a test particle at these points is zero. There are totally 5 Lagrange points in a binary system with those two,  $L_4$  and  $L_5$ , perpendicular to the radius vector connecting the companions and at the center of those two closed region shown in figure 1.3.

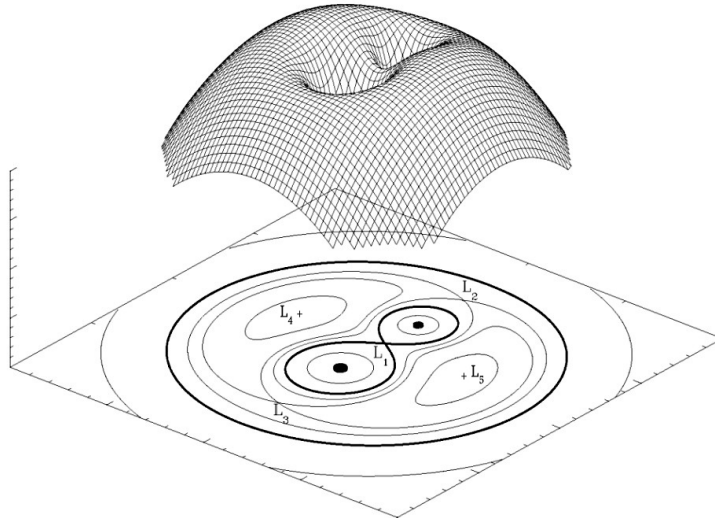


**Figure 1.3 :** Roche potential of a binary system [12].



If none of the stars fills its Roche lobe, the system is called *detached* and the accretion can occur only via stellar winds if they have strong winds such as OB type stars have. This phenomena is called *wind accretion*. One of the companion stars fills its Roche lobe during its evolutionary lifetime as a result of enlarging volume, then the star loses its spherical shape and becomes tear drop shaped as same as its Roche lobe. This form is determined by the mass ratio of the binary system,  $q = M_2/M_1$ . The matter in the Roche lobe of the enlarged star is transferred from the point of  $L_1$ . This is called *Roche lobe overflow*. Since the material has angular momentum sourced by the rotation of the donor star, the accreting matter does not fall onto the primary star directly but forms an accretion disk around it.

### 1.4.2 The Eddington limit

The Eddington limit, also called Eddington luminosity, is the maximum luminosity of a radiating object. It is determined by the balance of the *gravitational force* supposing that a small cloud with the mass of  $m$  and the opacity of  $\kappa$  is located at the distance of  $R$  from the center of the radiating object,

$$F_{grav} = \frac{GMm}{R^2} \quad (1.5)$$

where  $G$  is the gravitational constant,  $M$  and  $L$  are the mass and the total luminosity of the radiating object, respectively, with the *radiation force*,

$$F_{rad} = P_{rad}\kappa m \quad (1.6)$$

where  $P_{rad}$  is the radiation pressure,

$$P_{rad} = \frac{L}{c} \frac{1}{4\pi R^2}. \quad (1.7)$$

Balancing two forces gives us the Eddington luminosity which is a function only of the mass of radiating object;

$$L_{Edd} = \frac{4\pi GMc}{\kappa}. \quad (1.8)$$

If the accreting material is mostly ionized hydrogen and the Thomson scattering plays the main role on opacity, then a good approximation would be  $\kappa = \sigma_T/m_p$ , where  $\sigma_T$  is the Thomson cross-section and  $m_p$  is the mass of proton. Thus, Eddington luminosity can be written as follows;

$$L_{Edd} = \frac{4\pi GMcm_p}{\sigma_T}. \quad (1.9)$$

This allows us to calculate a maximum mass accretion rate on a compact object from its surrounding. The luminosity caused by mass accretion of  $\dot{M}$ , with the rest mass energy of  $\varepsilon$  is  $L = \varepsilon \dot{M} c^2$ . Equalizing this luminosity to  $L_{Edd}$ , Eddington accretion rate is written as follows;

$$\dot{M}_{Edd} = \frac{4\pi G M m_p}{\varepsilon c \sigma_T}. \quad (1.10)$$

### 1.4.3 High mass X-ray binaries

HMXBs are a type of X-ray binaries with a high mass ( $M_* \gtrsim 10 M_\odot$ ), mostly OB type and relatively young companions. These are highly eccentric systems with orbital periods longer than 1 day due to high binary separation. Since the OB type stars have very powerful winds driven by radiation pressure, the mass transfer mechanism in these systems is mainly wind accretion. In few systems, such as Cen X-3 [13], accretion can also proceed via Roche lobe overflow [14] with very short time-scale which makes it hard to detect. HMXB systems with NSs show X-ray pulsations because of accreting material onto NSs. NSs in these systems have strong magnetic fields ( $\sim 10^{12} G$ ) and the spin frequencies of them are below 15 Hz.

### 1.4.4 Low mass X-ray binaries

LMXBs are X-ray binary systems in which one of the companions is a compact object and the other is a late type low mass star ( $M_* \lesssim 1 M_\odot$ ) which fills its Roche lobe. Since late type stars do not eject matter via strong stellar winds, the accretion mechanism in these systems is realised via Roche lobe overflow. The gravitational potential energy of infalling material onto the NS is the source of the luminosity that we observe in which almost all of the energy is in the X-ray band with very low optical tail. The NSs in these systems have relatively low magnetic fields ( $\sim 10^8 - 10^{11} G$ ) indicating that they are old systems. Their magnetic field has been decreased in time by accretion force [15]. As a result of low magnetic field, some of them show type I X-ray bursts that are the instant H and He thermonuclear fusions reaching Eddington luminosity. This property allows to estimate the distance of the source with relatively low errors.

After the first detection of a millisecond pulsar (MSP) in an old system [16] which seems to disagree with the view that NSs are born with the fastest rotation period and slow down in time via angular momentum loss, the effect of the accretion mechanism

on spin up of the rotation of the NSs to milliseconds has been suggested [17, 18]. This is called “recycling scenario” and it is described that LMXBs are possible incubators of MSPs.

#### 1.4.5 Accreting millisecond X-ray pulsars

AMXP family is a subset of LMXBs but differs showing pulsations in their X-ray light curves. Total number of the AMXPs is a low fraction among all LMXB systems. It is not clear yet why not all LMXBs show X-ray pulsations. The X-ray light curves of AMXPs consist of quiescent and outburst phase in which the accretion phenomena and the disk magnetosphere interactions are directly related to these phases. With these specialities, they have the characteristic of laboratory to investigate the mass and angular momentum transfer from accretion disk to NS and to understand the connection of young radio pulsars with the old millisecond radio pulsars.

##### *Discovery of Accreting Millisecond X-ray Pulsars*

In 1998, Wijnands & van der Klis [19] reported the discovery of pulsations in transient X-ray burster, *SAX J1808.4–3658* with the frequency of  $\nu=401$  Hz. Even though this source was discovered in 1996 [20], the coherent X-ray pulsations were detected during the 1998 outburst by Wijnands & van der Klis using the RXTE observations. This object possibly will act like a millisecond radio pulsar when the accretion terminates completely. Markwardt et al. [21] observed pulsations at 435 Hz just after the discovery of the second AMXP, *XTE J1751–305*, by RXTE in 2002. This object is one of the six sources that do not show type I bursts, among all AMXPs. Then, the distance of *XTE J1751–305* was not obtained precisely. One of the AMXPs that RXTE discovered is *XTE J0929–314* with 185 Hz coherent pulsation. The pulsations of this source were detected during the 2002 outburst [22]. The fourth AMXP, *XTE J1807–294*, was discovered by Markwardt et al. in 2003 using RXTE observation [23]. This source has very short orbital period with the value of 40.1 min. Falanga et al. (2005) [24] showed that the companion star should have mass less than  $0.022 M_{\odot}$  using INTEGRAL, XMM–Newton and RXTE observations, simultaneously. In 2003, the fifth AMXP, *XTE J1814–338*, was discovered by Markwardt et al. [25]. This source has pulsations with 314 Hz frequency and the orbital period of 4.3 hr indicating that the companion star is more massive than  $0.17 M_{\odot}$ . *IGR J00291–5934* was discovered

by INTEGRAL in 2004 by Eckert et al. [26]. This source is the fastest AMXP with pulsation frequency of 599 Hz. No type-I bursts have been detected in the observations of IGR J00291+5934, yet. Another X-ray burst source, *HETE J1900.1–2455*, was detected by the high energy transient explorer (HETE). Morgan et al. (2005) [27] published the discovery of pulsations at 377 Hz using the observation of RXTE. This source differs from the other AMXPs due to its intermittent character. Its pulsations persisted until the 20th day of the 2005 outburst, and disappeared and reappeared during the outbursts in the next 2.5 years. Such intermittent sources are important for understanding the discrepancy between non-pulsating LMXB and AMXPs. After the discovery of *Swift J1756.9–2508* in 2007, detailed RXTE observations showed that this source shows pulsations with the frequency of 182 Hz [28]. This source is another ultra compact AMXP with 54.7 min orbital period. *Aql X–1* is the second intermittent source with 550.27 Hz pulsations. Remarkably, the pulsations were detected only for 120 s by RXTE in the maximum of the 1998 outburst over 10 years of observations. Even if the pulsations were observed for a short episode, still the accretion-powered origin of the pulsations is the most reasonable explanation [29]. *Aql X–1* has a quite bright optical counterpart, V1333 *Aql*, with the B band magnitude of  $17^m$ , discovered in 1978 [30]. Gavril et al. (2006) reported coherent pulsations of *SAX J1748.9–2021* [31]. This source had never showed pulsations after its discovery in 1998 until the 2005 outburst. The total number of intermittent systems among all AMXPs is three; *HETE J1900.1–2455*, *Aql X–1* and *SAX J1748.9–2021*. In 2010, Altamirano et al. presented the discovery of 206 Hz pulsations of *NGC 6440 X–2* from RXTE data during 2009 outburst [32]. This source is a member of ultra compact AMXPs with 0.95 hr orbital period. INTEGRAL discovered a new X-ray source, *IGR J17511–3057*, in 2009 and the system was classified as AMXP after the detection of 245 Hz pulsations by Markwardt et al. (2009) using RXTE [33]. *Swift J1749.4–2807* was first observed by the Swift gamma-ray burst mission/burst alert Telescope (SWIFT/BAT). These observations showed a high level of activity which is the reason why this source is identified as “burst-only” accreting neutron star binary. Altamirano et al. (2010) reported the detection of pulsations at 518 Hz in RXTE/PCA observations [34]. A powerful second harmonic at 1036 Hz was detected by Bozzo et al. (2010) [35]. In 2011, a new X-ray source, *IGR J17498–2921*, discovered by INTEGRAL, showed the pulsations at 401 Hz and its orbital period has been estimated

as 3.8 hr [36]. This source also shows Type-I bursts which reach Eddington limit indicating that the distance is 7.6 kpc [37]. Another AMXP is *IGR J18245–2452* discovered by INTEGRAL in 2013 [38]. This source is a member of the globular cluster M28 at distance of 5.5 kpc. The coherent pulsations were detected at 254 Hz via XMM–Newton observations during its outburst phase. The importance of this source is that IGR J18245–2452 is the first AMXP known to switch from radio millisecond pulsar. This knowledge comes from the past observations of the globular cluster M28 that a radio millisecond pulsar (PSR J1824–2452I) is located in the same region. In Table 1.1, some properties of known AMXPs are listed (for more details see the review by Patruno & Watts 2012 [39]).  $\nu_s$  is the spin frequency in Hz,  $P_b$  is the orbital period in hours and  $M_{c,min}$  is the minimum mass of the companion in the unit of solar mass, assuming that the neutron star mass is  $1.4 M_\odot$ . The last column shows the type of the companion stars where BD is brown dwarf, He WD is helium cored white dwarf, C/O WD is carbon oxygen cored white dwarf, MS is main sequence star and subG is sub giant.

**Table 1.1** : Accreting millisecond X-ray pulsars.

Source	$\nu_s$ (Hz)	$P_b$ (hr)	$f_x$ ( $M_\odot$ )	$M_{c,min}$ ( $M_\odot$ )	Companion Type
SAX J1808.4–3658	401	2.01	$3.8 \times 10^{-5}$	0.043	BD
XTE J1751–305	435	0.71	$1.3 \times 10^{-6}$	0.014	He WD
XTE J0929–314	185	0.73	$2.9 \times 10^{-7}$	0.0083	C/O WD
XTE J807–294	190	0.67	$1.5 \times 10^{-7}$	0.0066	C/O WD
XTE J1814–338	314	4.27	$2.0 \times 10^{-3}$	0.17	MS
IGR J00291+5934	599	2.46	$2.8 \times 10^{-5}$	0.039	BD
HETE J1900.1–2455	377	1.39	$2.0 \times 10^{-6}$	0.016	BD
Swift J1756.9–2508	182	0.91	$1.6 \times 10^{-7}$	0.007	He WD
Aql X–1	550	18.95	N/A	0.6 <sup>a</sup>	MS
SAX J1748.9–2021	442	8.77	$4.8 \times 10^{-4}$	0.1	MS/SubG ?
NGC6440 X–2	206	0.95	$1.6 \times 10^{-7}$	0.0067	He WD
IGR J17511–3057	245	3.47	$1.1 \times 10^{-3}$	0.13	MS
Swift J1749.4–2807	518	8.82	$5.5 \times 10^{-2}$	0.59	MS
IGR J17498–2921	401	3.84	$2.0 \times 10^{-3}$	0.17	MS
IGR J18245–2452	254	11.03	$2.3 \times 10^{-3}$	0.17	MS

$\nu_s$  is the spin frequency,  $P_b$  the orbital period,  $f_x$  is the X-ray mass function,  $M_{c,min}$  is the minimum companion mass for an assumed NS mass of  $1.4 M_\odot$ . The companion types are: WD = White Dwarf, BD= Brown Dwarf, MS = Main Sequence, SubG = Sub-Giant, He Core = Helium Star [39].

<sup>a</sup> The donor mass is inferred from photometric data and does represent the most likely mass.



## **2. X-RAY OBSERVATORIES AND DATA ANALYSIS**

### **2.1 X-ray Missions**

The investigations on X-ray sources stepped into a new age with the first X-ray astronomy purposed satellite; UHURU, also known as small astronomical satellite 1 (SAS-1) launched on December 12, 1970 by the national aeronautics and space administration (NASA). There are few ongoing X-ray missions such as; the XMM-Newton observatory and the INTEGRAL by European space agency (ESA), the Swift and the Chandra observatories by NASA. There are also past missions in which their data are available on archives such as RXTE. In the context of this thesis we used the data obtained by RXTE and SWIFT. In the next two sections, brief information about these two instruments is given as compiled from Ref. [40] and Ref. [41].

### **2.2 The Rossi X-ray Timing Explorer**

RXTE was launched on December 30, 1995 by NASA to its orbit around earth with the altitude of 580 km. Although it has been deactivated on January 5, 2012, 16 years public data are still accessible on archive [40]. RXTE has three detectors, the proportional counter array (PCA), the high energy X-ray timing experiment (HEXTE) and the all sky monitor (ASM). In Figure 2.1, a schematic view of RXTE with the instruments aboard it is presented.

The ASM scans almost 80% of whole sky in the energy range of 1.3 – 12.1 keV during one period of RXTE in its orbit with three wide angle proportional counters. It is very useful for following long term evolution and outburst properties of bright sources. In this thesis, we have benefited from the ASM data for obtaining light curve of Aql X-1 overall the lifetime of RXTE.

The PCA is composed of five proportional counter units (PCUs) with 256 energy channels responsive to the energy range of 2 – 60 keV. The most sensitive energy range of the PCUs is 3 keV to 30 keV. This range is used to extract spectra that we

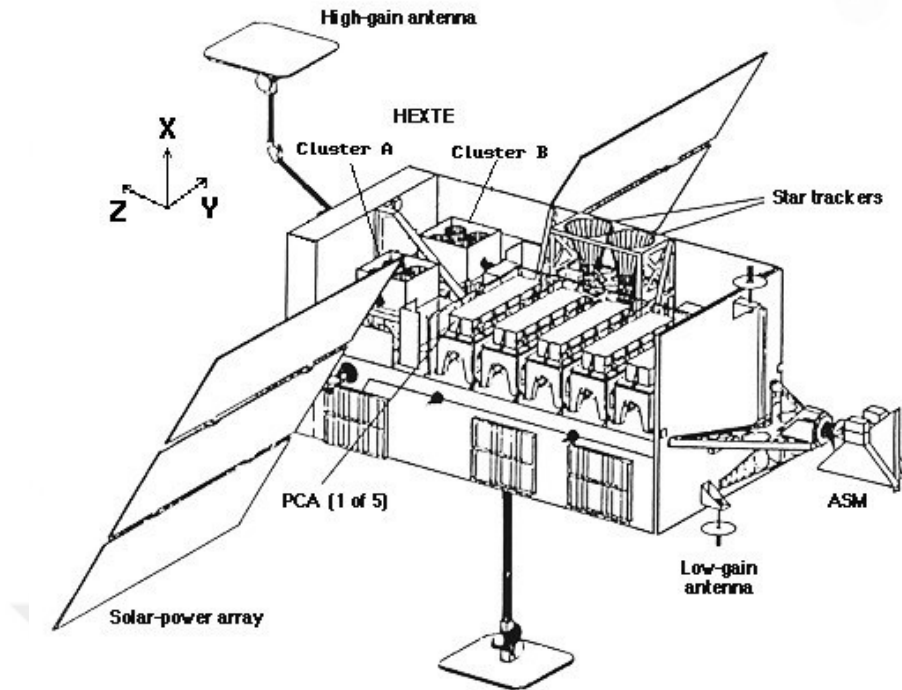


**Figure 2.1 :** The Rossi X-ray Timing Explorer.

analysed. It has the photon collecting area of  $\sim 6500 \text{ cm}^2$ . The time resolution of the PCA is  $1 \mu\text{s}$  which makes this instrument suitable for timing investigations.

The HEXTE consists of two clusters each containing four scintillation detectors. It has the energy range of  $15 - 250 \text{ keV}$ . The data obtained from the HEXTE and the PCA together, allows to create spectra from  $2 \text{ keV}$  to  $250 \text{ keV}$ .

### 2.3 The Swift Gamma-Ray Burst Mission

The Swift gamma-ray burst mission (SWIFT) which has been developed by a collaboration of United States, United Kingdom and Italy and lead by the principal investigator Neil Gehrels, NASA Goddard Space Flight Center, was launched on November 20, 2004 aimed mainly to focus on gamma ray burst studies. It is operated by Pennsylvania State University. Three instruments are aboard on SWIFT whose main property is to point and focus very quickly ( $\sim 50 \text{ s}$ ); the Burst Alert Telescope (BAT), the X-ray Telescope (XRT) and the Ultraviolet/Optical Telescope (UVOT). In Figure 2.2, the structure of SWIFT with three instruments on-board is shown.

The BAT has the mission of detecting gamma ray bursts and compute their location. Its collecting area is  $5200 \text{ cm}^2$  and the energy range is  $15 - 150 \text{ keV}$ .



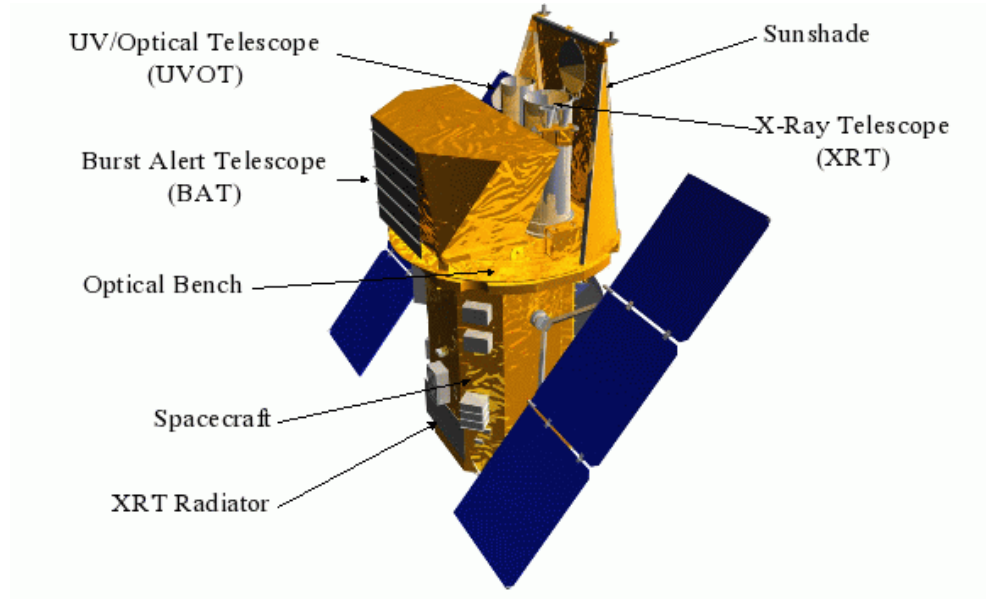


**Figure 2.2 :** The Swift Gamma-Ray Burst Telescope.

The XRT is the X-ray mirror telescope providing the spectra in the energy range of 0.2 – 10 keV. This instrument has the ability to obtain data in three different observation modes; the photodiode mode with 0.14 ms time resolution in which the aim is to obtain timing information of bright objects with high time accuracy, the windowed timing mode with 2.2 ms time resolution and one dimension position information and spectroscopy, the photon counting mode with full imaging and spectroscopic information but only 2.5 s time resolution. In this thesis, only XRT data in window timing mode is used to obtain the X-ray spectra of Aql X-1.

The UVOT is 30 cm ultraviolet and optical telescope sensitive to the wavelength range of 170 – 650 nm oriented parallel to the XRT.



### 3. CLASSIFICATION AND SPECTRAL EVOLUTION OF OUTBURSTS

#### 3.1 Introduction

AMXPs show cyclic outbursts in their X-ray light curves. The X-ray morphology of outbursts of all transient systems, show a wide range of lightcurve patterns. A typical lightcurve pattern is described as the fast-rise-exponential-decay (FRED) [42]. A FRED lightcurve can be reproduced with the disc instability model (DIM; see Ref. [43] for a review) only if the irradiation of the outer parts of the disk by the X-rays from the central source is taken into account [44]. Apart from events that show FRED like behavior and its varieties there is also a low-intensity-state (LIS) [45] in which the optical and near IR emission flux is above quiescence but the lightcurve does not follow the FRED trend and can last longer. What leads to such distinct outburst lightcurves is not very well understood.

A clue to the diversity of the outburst lightcurve morphology could be the variety of spectral states the transient systems exhibit. A soft X-ray transient (SXT) in the rising phase of the outburst would usually enter the high/soft state (HS; higher flux, softer spectrum) from the low/hard state (LH; lower flux, harder spectrum) and return to the LH state during the decay of the outburst (see Ref. [46] for a review of spectral states in black hole systems). Spectral states of SXTs in which the accreting objects are neutron stars are similar to those in black hole systems. This similarity is not well understood given that the neutron stars have hard surfaces where the energy of the accreting matter would be thermalized whereas the black holes have event horizons through which the energy could be advected with the accretion flow.

The HS state is associated with a standard geometrically thin optically thick Keplerian disk [47] while the LH state is associated with a geometrically thick optically thin advection dominated disk [48, 49] and a corona at which the soft seed photons from the disk blackbody are up-scattered by relativistic electrons. In order to address the

low luminosity in the hard state it is also necessary to introduce the truncation of the inner region of the geometrically thin accretion disk.

The different modes of interaction between the magnetosphere of the neutron star and the surrounding disk, that take place at different accretion rates, which changes by three orders of magnitude during an outburst, may also have a role in the diversity of the lightcurve morphology. During the decay phase in which the mass flux is decreasing, the inner radius of the disk moves outwards. Once the inner radius is pushed beyond the corotation radius, it is expected that accretion onto the star is inhibited by the centrifugal barrier and the system is said to be in the “propeller” stage [50–53]. Aql X–1 is one of the most active SXTs (see Ref. [54] for a review) making it possibly the most suitable system for classifying outbursts, investigating the interplay between irradiation, transition to propeller stage and spectral transitions

### 3.2 Classification of Outbursts of Aql X–1

Aql X–1 is a LMXB in which a neutron star accretes matter from an accretion disk which is supplied by the Roche lobe filling low mass companion. Aql X–1 is also classified as a SXT; most of the time it is in a quiescent state with a luminosity of  $L_X \approx 10^{33} \text{ erg s}^{-1}$  [55] while occasionally it exhibits outbursts which at the peak can reach to  $L_X \approx 10^{37} \text{ erg s}^{-1}$  resulting from the enhanced accretion rate,  $\dot{M}$ , in the disk. Figure 3.1 shows the long term X-ray light curve of Aql X–1 using ASM and MAXI data. According to the DIM, the viscous-thermal instability in the disk [56] is the cause of the enhanced accretion. Conforming to the tracks it follows on the X-ray color-color and hardness-intensity diagrams, and spectral variations that Aql X–1 shows, it is identified as an atoll source [57,58]. In this case HS and LH states roughly correspond to banana and island states [58], respectively. Aql X–1 showed a rapid decay of luminosity accompanied by an abrupt spectral transition during the decline of its 1997 outburst which was interpreted as the onset of the “propeller” stage [59,60].

Following the ideas in Ref. [59] and Ref. [60], a broad classification of outbursts of Aql X–1 based on the duration and the maximum flux is executed. A different classification for the outbursts of this object was presented by authors of Ref. [61] based on the spectral transitions (see also Ref. [62,63]). The classification presented in this thesis may not be an alternative to the classification of Ref. [61]. Figure 3.2 (upper

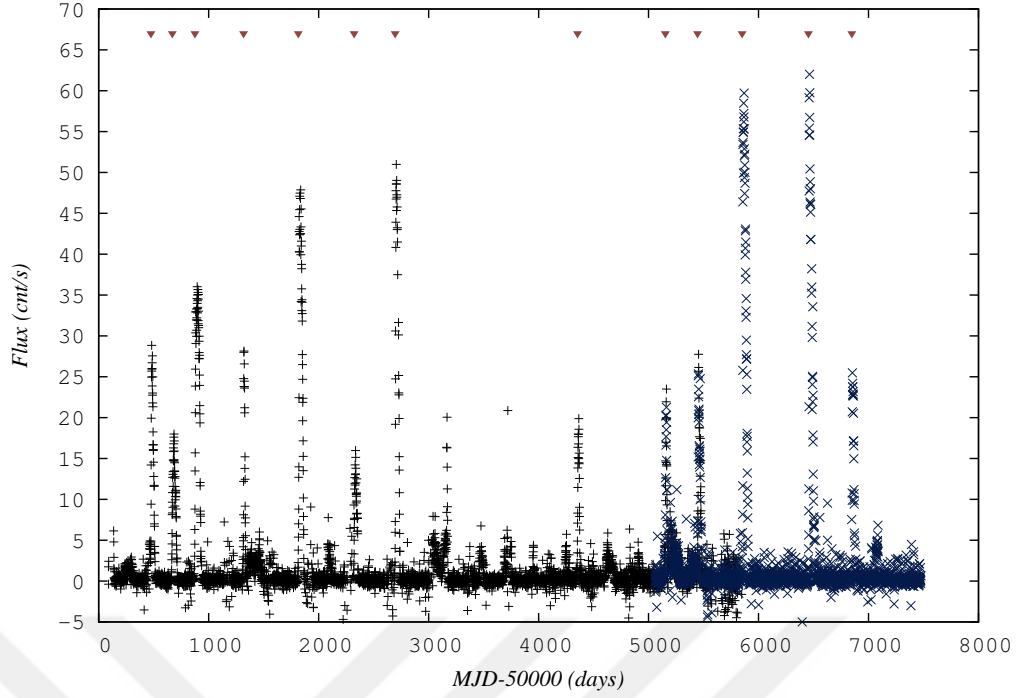


**Figure 3.1** : Long term light curve of Aql X-1 using ASM (black pluses) and MAXI (dark blue crosses) data. Brown triangles show the outbursts that are used in classification.

panel) shows all outbursts as observed by ASM [64] aboard the RXTE [65]; after 2011 outbursts observed by MAXI [66]. For each instrument the daily average values were used in the 2–10 keV and 2–20 keV range, respectively. By comparing the peak count rate of the 2009 and 2010 outbursts, which were observed by both detectors, the data sets from the two instruments were calibrated. Using the near-simultaneous detections, we determined a conversion factor of  $\approx 22$ . The beginning of the outbursts were determined as the point at which the count-rate reaches 5 cnt/s. To see the trends in the lightcurves more clearly the data sets were smoothed using the Bézier spline method.

The upper panel of Figure 3.2 shows the evolution of count-rate in all data sets. It is seen that 2013 outburst is the brightest outburst of Aql X-1 in the data set, as was suggested by authors of Ref. [67]. Note that this classification does not include outbursts corresponding to LIS that last even longer than the long-high outbursts at a LH state, but never reaches to count-rate of 5 cnt/s level, which is our criterion to calibrate initial times of all outbursts. It is clearly seen that there are three types of outbursts;

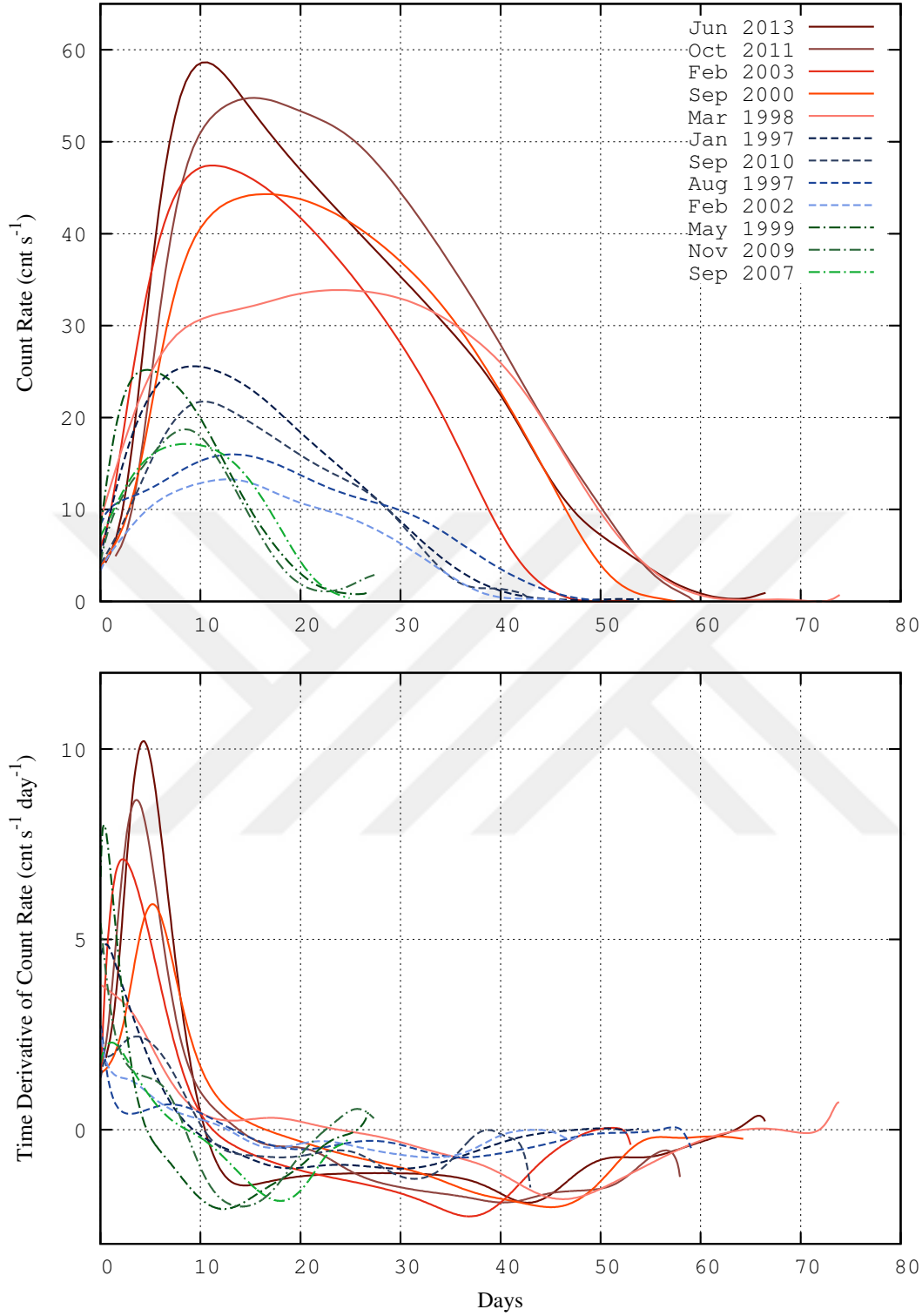


**Figure 3.2 :** ASM and MAXI lightcurves of outbursts (upper panel) and their time derivative. The data is smoothed with Bézier process for visualization. Three types of outbursts can be discriminated: (i) The long-high outbursts shown with solid lines (red). These events last about 50-60 days and reach a count rate of 37-61 cnt/s. (ii) The medium-low outbursts, shown with dashed lines (blue), last about 40-50 days and reach a count rate of 13-25 cnt/s. (iii) The short-low outbursts, shown with dashed-dot lines (green), last about 20 days and reach a count rate of 17-25 cnt/s.

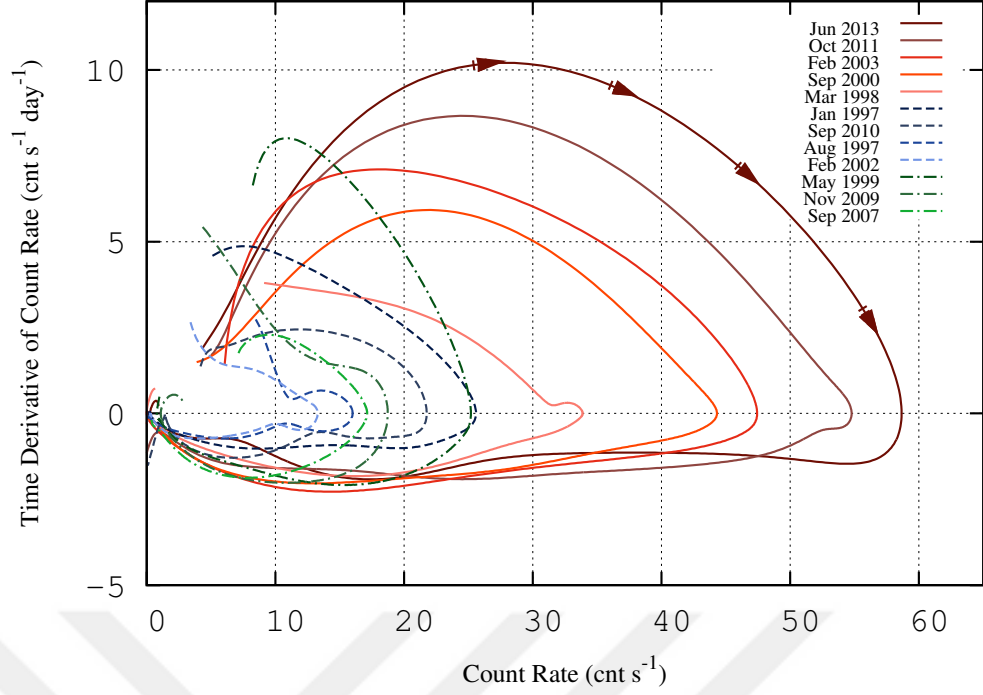


**Figure 3.3** : The outbursts in the counts/s versus counts/s/day “phase space”. The arrows on the curve of June 2013 event show the direction of time. Outbursts start from the upper-left domain, move clockwise, pass from the  $y = 0$  at the peak of the outbursts, and reach to the lower-left domain (quiescence).

- The *long-high* outbursts have long duration with 50-60 days and are luminous, reaching a maximum flux of 35-60 cnt/s.
- The *medium-low* outbursts last for 40-50 days, reaching a maximum flux of 13-25 cnt/s.
- The *short-low* outbursts last for approximately 20 days reaching a maximum flux of 17-25 cnt/s.

Conversion of the data sets to continuous curves by Bézier spline method allows us to evaluate the time derivative of the flux curves, which we show in the lower panel of Figure 3.2. We see that the rising stages of the bright outbursts consist of two sub-stages in which the flux change rate increases and then decreases. The medium-low outbursts show a more complex trend. It is also seen that the decay stage also roughly consists of two sub-stages in which the flux decay rate first speeds-up and then slows down. The behavior at the lowest flux levels are much more complicated, showing variability at a time-scale of days.

Figure 3.3 shows the evolution of the outbursts in the “phase space” of flux-rate versus flux. An outburst starts from the upper-left domain of the plot, moves clockwise as shown with arrows on the outermost curve for the June 2013 and ends near the origin. This figure presents the gradient of the count rate evolution in time in units of count rates and allows to infer the flux level at which the time evolution becomes the steepest. The steepest point in the decay phase corresponds to the transition from the slow decay phase to the fast decay phase.

### 3.3 Observation and Data Analysis

In order to better characterize the distinction between different types of outbursts, the monitoring observations performed by RXTE/PCA were used. We analysed the 2000, 2010, and 2011 outbursts of Aql X-1. Based on the above mentioned classification, the 2000 and 2011 outbursts are members of the long-high class and the 2010 outburst is a member of the medium-low class. The times of RXTE observations during 2010 and 2011 outbursts are shown on the MAXI lightcurve in Figure 3.4. It is clearly visible that the 2011 outburst is much more luminous than 2010 outburst and the RXTE pointings in 2011 covers the outburst completely, including both the rise and decay phases. We also focused on the 2000 outburst as a comparison, since it is one of the most luminous outbursts with detailed RXTE observations.

As Aql X-1 is a bright source, using one of the four PCUs is sufficient to produce high S/N spectrum. In this work only PCU2, which has been calibrated the best and has been continuously working, was used. The data were analysed using HEASoft v6.11 and response matrices were created separately for each data set using the PCARSP version 11.7. The background spectra were produced using the latest module file for bright sources, *pca\_bkgd\_cmbrightvle\_eMv20051128.mdl*.

For the spectral analysis an X-ray spectral fitting package (XSPEC) v12.7.0 was used. After subtracting the background from the original data, the energy range of 3–30 keV was fitted, retaining the band at which the PCA detector is the most sensitive. The systematic error of 1% was also added to take into account internal gain. During the 2010 and the 2011 outbursts, 2 and 4 Type-I thermonuclear X-ray bursts were determined, respectively. These time ranges in the data covering 100 seconds before the start and 100 seconds after the end of these bursts, were ignored.



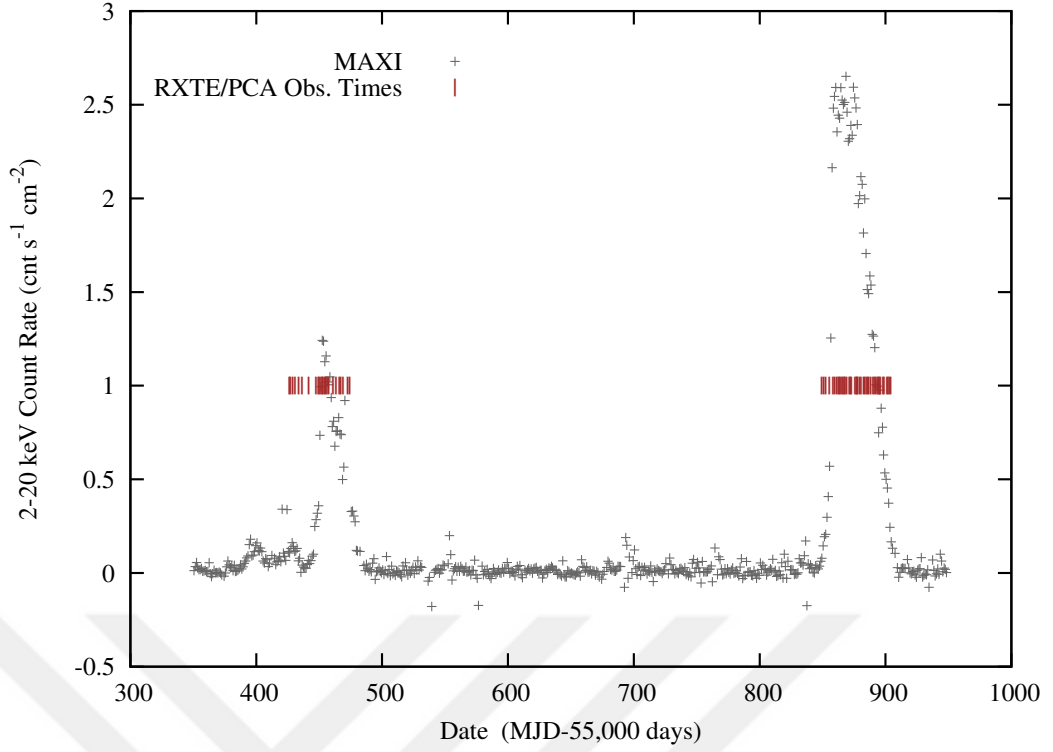


**Figure 3.4** : The long-term evolution of Aql X-1 as observed by MAXI between June 2010 to January 2012. Dates of RXTE/PCA observations are marked with vertical bars.

Following the method by authors of Ref. [68], the spectra were fitted with the EQPAIR model [69], which is a hybrid comptonization model bridging the purely Maxwellian and purely power-law particle energy distributions, responsible for the emission, in a self-consistent way. EQPAIR uses the ratio of relative heating and cooling of electrons on account of radiative processes and Coulomb interactions for solving the electron distribution. Many other models have been employed in the literature for fitting the X-ray spectra of LMXBs [70, 71]. Statistically, all these models fit the X-ray spectra as successfully as EQPAIR. EQPAIR has been used for fitting X-ray spectra of disk flows with corona in LMXBs with black hole components [72]. As such EQPAIR can not address how much the neutron star contributes to the thermal and non-thermal emission from these sources. Our choice of EQPAIR for modeling the spectra is motivated by the purpose of investigating the role of the parameters of the corona in the irradiation of the outer disk. Using EQPAIR also allows to compare our results with earlier studies [68]. Since EQPAIR is a hybrid model for both plasma, the disk and the corona, it is able to fit all the energy range between 3.0 keV and 30.0 keV, with the addition of a statistically necessary Gaussian component.

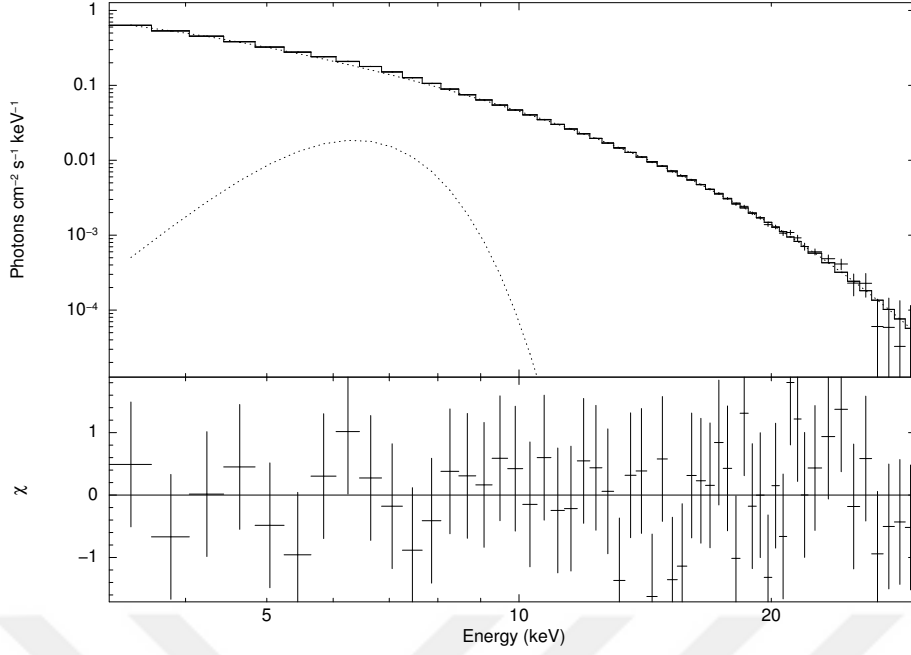


**Figure 3.5 :** Upper panel shows the X-ray spectrum (Obs ID 96440-01-03-04) in the energy range of 3.0 – 30.0 keV together with the best fit of EQPAIR model and a Gaussian line. Lower panel shows the residuals in terms of sigma.

The neutral hydrogen column density was fixed at  $N_H = 3.4 \times 10^{21} \text{ cm}^{-2}$  [68]. The soft photon compactness ( $l_{bb}$ ) and the fraction of power supplied to energetic particles which goes into accelerating non-thermal particles ( $l_{nt}/l_h$ ) were frozen at 1.0 and 0.0, respectively. This allows to determine  $l_h$  in terms of  $l_{bb}$ . Authors of Ref. [73] show that the orbital inclination should be greater than 36 degree. The inclination angle was chosen as 60 degrees for simplicity. All the other parameters of EQPAIR model, were set to default values and kept frozen during the fit following the method in Ref. [68]. After reaching the best fit parameters of EQPAIR model with minimum  $\chi^2$ , a Gaussian component was added to represent the systematic residuals due to the iron line between 5.8 keV and 7.0 keV for each observation. In Figure 3.5, an example X-ray spectrum of Aql X–1 obtained during the peak of the 2011 outburst (Obs ID 96440-01-03-04) and the best fit EQPAIR model with a Gaussian line are shown .

For all the X-ray spectra of Aql X–1 obtained by RXTE/PCA observations, the procedure described above was followed. Overall, for the 2000 outburst 55 pointings were obtained, when the source was in the outburst phase. The 2010 outburst was covered with 24 pointings. Seven of these observations were obtained when the source was still in quiescent phase, which allows to better characterize how parameters evolve

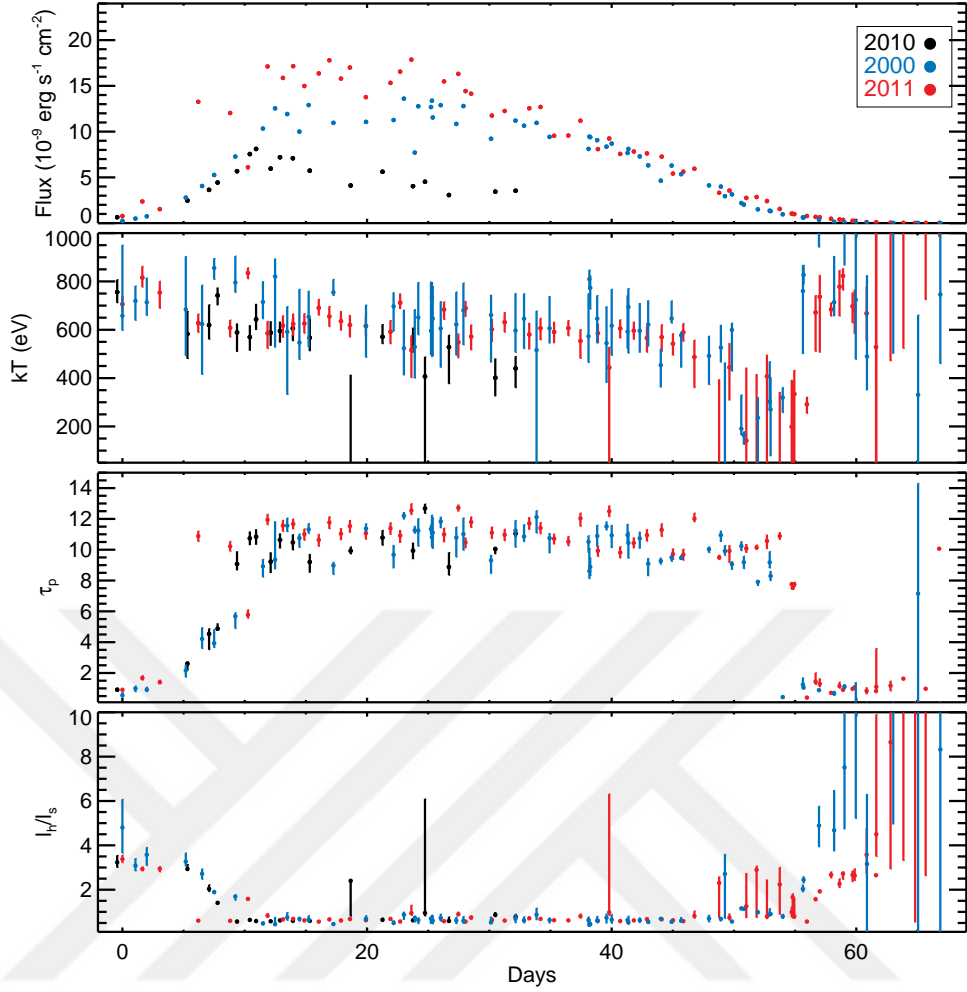


**Figure 3.6** : Spectral evolution of Aql X-1 during 2000 (Blue), 2010 (black) and 2011 (red) outbursts. From upper to lower, panels show the evolution of unabsorbed total flux, temperature of the seed photons, optical depth, and the ratio of hard to soft compactness, respectively. All fluxes are given in units of  $10^{-9} \text{ erg s}^{-1} \text{ cm}^{-2}$ . Times of the data are calibrated based on the beginnings of outbursts.

as the source advances from quiescence to outburst. 43 data sets completely comprise both the rise and decay phases of the 2011 outburst.

The free parameters of EQPAIR model are the optical depth of the corona ( $\tau$ ), the seed photon temperature ( $k_B T_{bb}$ ) and the hard state compactness ( $l_h$ ). Figure 3.6 shows the time evolution of these parameters during 2000, 2010 and 2011 outbursts. The spectral parameters evolve in a very similar way in each outburst: (i) The optical depth of the corona increases during the rise and becomes stable until the end of the decay. (ii) The hard state compactness decreases to  $\approx 0.5$  immediately after the onset of outbursts. (iii) It is seen that the seed photon temperature slightly decreases as the outbursts proceed. This however is the least constrained parameter in our model because the inferred

values are too low for the RXTE/PCA sensitivity range, during the outburst. The best fit parameters of EQPAIR model and Gaussian component including the errors are shown in Table A.1, Table A.2 and Table A.3.

### 3.4 Discussion

The diversity of outburst morphology presented in Section 3.2 can be associated with three different causes: *(i)* A longer waiting time before an outburst might lead to larger amount of matter accumulation in the disk resulting in long-high type outbursts; *(ii)* it might be that only during the long-high outbursts the inner radius of the disk penetrates the corotation radius leading to substantial accretion while the medium-low and the short-low outbursts both proceed by partial accretion during the spin-down regime; *(iii)* a different portion of the disk is involved in different types of outbursts probably because of different irradiation geometries involved. In the following we discuss these three options in detail and discuss the implications of the results of our spectral analysis.

#### 3.4.1 Is the quiescent stage duration related to the different outburst classes?

One naturally expects that a longer waiting time between two outbursts might lead to a larger amount of matter accumulation in the disk resulting with a more luminous outburst. This possibility was considered by authors of Ref. [63] (see their fig. 6) who checked whether the peak flux of outbursts are correlated with the preceding waiting times before the outbursts. They found only a very weak correlation indicating that the duration of the quiescent stage is not the main cause of the difference between the long-high, medium-low and short-low classes.

#### 3.4.2 Transition to the propeller stage as the cause of the rapid decay stage

The rapid decay of luminosity during the decline of the 1997 outburst of Aql X–1 was interpreted as the onset of the “propeller” stage [59, 60]. A similar rapid decline stage is shown also by the first discovered AMXP [19] SAX J1808.4–3658 in several of its outbursts. This was associated with transition to propeller stage by authors of Ref. [74]. The 1997 outburst of Aql X–1 which led to the propeller interpretation is of the medium-low class. It can be seen from Figure 3.2 that, compared to the 1997

event, the 1998 outburst shows a much more prominent transition from slow decay to rapid decay at a count-rate level of  $\approx 27$ . Assuming that this flux level corresponds to the critical mass flow rate that places the inner radius on the corotation radius, one is forced to conclude that the system remains in the spin-down stage throughout the medium-low and short-low outbursts, accreting only a fraction of the inflowing mass because the maximum count-rate for these outbursts remain below  $\approx 27$  cnt/s. For this point, the critical mass accretion rate is  $\approx 10^{17}$  g s $^{-1}$ . Within this scenario the inner radius can penetrate the corotation radius only for the brightest outbursts which possibly could address why many outbursts are stunted and why pulsations are elusive.

In the case of SAX J1808.4–3658 (but not Aql X–1) the X-ray pulsations continue to be detected even in the rapid decay stage [75]. In order to address this issue authors of Ref. [76] argued that it is not energetically possible for the magnetosphere to eject matter from the system as the magnetosphere expands to the corotation radius with the decaying mass flux. They presented disk solutions in which the inner radius of the disk remains on the corotation radius for a large range of mass flux such that accretion and X-ray pulsations continue. Authors of Ref. [77] concluded from the variations of the pulse profiles that the size of the hot spot on the neutron star changes throughout the outburst which then indicates that the inner radius of the disk does recede during the decay of the outburst. Authors of Ref. [78] associated the rapid decay stage of SAX J1808.4–3658 with a partial accretion regime [79–81] in which matter at the disk mid-plane is centrifugally inhibited while matter vertically away from the mid-plane can accrete. This requires the inner region of the disk to be geometrically thick as required by radiatively inefficient disk models that address the LH state.

The onset of a propeller during an outburst may affect the number of thermonuclear X-ray bursts occurring during an outburst. To test the propeller scenario, therefore, Type-I X-ray bursts were investigated during different outbursts. Using the X-ray burst catalogue of Ref. [82], the number of X-ray bursts detected was identified during a given outburst. Although such an analysis is subject to selection effects due to the varying coverage of the RXTE/PCA of individual outbursts, it was found that a similar number of X-ray bursts and photospheric radius expansion events have been observed from different types of outbursts. For example, during the short-low outburst observed in 1999, two photospheric radius expansion events were observed together with one

Type-I burst. On the other hand during the 2000 outburst, which is a long-high event according to our classification, 4 Type-I X-ray bursts were observed of which one is a photospheric radius expansion event. A similar trend is also observed during the two outbursts observed in 1997 and 2002, which are both medium-low type outbursts. During these outbursts 1, 4, and 5 type-I X-ray bursts have been observed with one photospheric radius expansion event during each of the 1997 outbursts and 2 during the 2002 outburst. It must be noted, however, that there are exceptions, for example the short-low outburst that occurred in 1998 was observed with RXTE/PCA with 24 pointings. Despite the dense coverage not a single X-ray burst was observed during the outburst from the source. This seems to support the argument discussed above that there had been a transition to the propeller stage during the 1998 outburst.

It is suggested by authors of Ref. [61] that the transition to the propeller stage as an explanation for the rapid decay in the light curves of 4U 1608–52, Aql X–1 and XTE J1701–462 identifying transition to propeller stage from the spectral transitions by using luminosity dwell-time distributions (see also [83]). This does not mean that irradiation is not present in the system, but only that it may not be the cause of the rapid decay stage. Presence of jets [84] in this system associated with transition from HS to LH state may also indicate the role of the “propeller” for ejecting matter from the system [80, 85–87].

A well known argument against the propeller interpretation is that not only NS SXTs but some black hole SXTs also show a “brink” in the decay stages of their outbursts implying a common origin for the rapid decay [88]. As black holes do not have a magnetosphere, propeller mechanism can not be at work in these systems and thus can not be the common cause for the rapid decay stage. The presence of similar spectral transitions also suggests a common mechanism disfavouring transition to propeller as the cause of the spectral transitions.

Yet another argument against the propeller interpretation is the hysteresis effect: Authors of Ref. [89] showed that the LH to HS spectral transition at the initial rise of the burst occurs at a luminosity 5 times greater than that of the transition from HS to LH at the declining stage suggesting that propeller mechanism alone can not be the driver of the spectral transitions as one would expect transitions between accretion and propeller stages to be at a single luminosity for a certain system [90]. During the

declining stage of the very faint 2001 outburst of Aql X-1, a spectral transition from LH to HS state indicated that mass flow rate,  $\dot{M}$ , is not the sole parameter determining the luminosity of the transition and mentioned the role of change in the mass flux [91].

These problems with the propeller interpretation can partly be surpassed by suggesting that the transition to the propeller stage is not the cause of the spectral transition but a consequence of it. If the inner disk makes a transition to a geometrically thick radiatively inefficient flow causing the transition to the LH state, the mass flux and the material stresses suddenly drop as the flow becomes sub-Keplerian; the magnetosphere pushes the disk outwards which may then cause the system to transit to the propeller stage if the disk is pushed beyond the corotation radius.

### **3.4.3 Irradiation as the parameter inducing different outburst durations and peak fluxes**

The difficulties in interpreting the rapid decline as transition to the propeller stage led to the favoured view that the cause of transition to the rapid decay stage is related to the outer disk disconnecting from the inner disk by entering the cool low-viscosity state as this region is no longer irradiated [92], the third possibility we would like to discuss.

Authors of the Ref. [63] presented that an in-depth analysis of the outbursts observed from Aql X-1 using the irradiated disk model of Ref. [92] and fitted the observed lightcurves. This brings in two different estimates of the outer radius of the disk: either determined via the viscous timescale at the outer radius or via the furthest point that is irradiated in the disk. One naturally expects that the peak flux would be proportional to the size of the disk kept hot by irradiation. The larger disk is the more material may be transferred from the disk to the pole of the NS which causes the higher energy releases. The estimated outer disk radius can be seen In Figure 3.7 versus the peak count-rate identified in Section 3.2. The outer radius values are from authors of Ref. [63] who estimated them based on the irradiation model [92]. Peak fluxes correspond to each outburst were obtained from the smoothed outbursts in Section 3.2. It was found that the peak flux is roughly correlated with the disk size. As the maximum size of the disk is determined by the Roche lobe radius, only during the long-high type outbursts the disk can have radii reaching that range while the disk during the medium-low and the short-low outbursts either does not fill the Roche lobe radius, or that the outer parts of

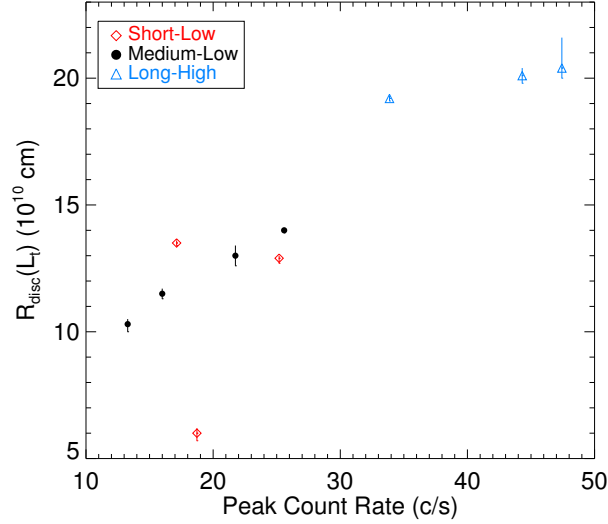


**Figure 3.7 :** Outer disk radius versus the peak count-rate of outbursts of Aql X-1. The outer radii of the outbursts are estimated by [63] via the furthest point irradiated in the disk. We see a linear correlation as would be expected that a larger outburst would require a larger portion of the disk to be involved in the outburst. Different classes of outbursts are shown with different symbols. The long-high and the medium-low outbursts have a tighter correlation with a different slope while short-low class shows no correlation.

such a disk is not sufficiently hot to be active and is not involved in the outburst. If the latter is the case then the correlation of the peak flux with the disk size is consistent with the view that a larger portion of the disk is involved in the long-high type of outbursts probably due to the different irradiation efficiency of the outer parts.

Although the number of data for each individual type of outburst is small, it is possible to infer from Figure 3.7 that the long-high and the medium-low outbursts have different slopes while the short-low outbursts show a large scatter and does not reveal its trend. The smaller slope of the long-high outbursts implies that for such large sized discs a slight increase in the disk size leads to much higher peak flux. This is because the amount of matter and angular momentum within a ring of definite width increase rapidly with radial distance from the center. Thus a small change in the irradiation geometry may lead to a small change in the heated outer radius which then would lead to drastic changes in the outburst morphology.

#### 3.4.4 Implications of spectral analysis

We consider the possibility that the differences between three different outburst types of the classification described in Section 3.2, could originate from different spectral



properties the disk displays. In order to check this possibility, the spectral evolution during the 2000, 2010 and 2011 outbursts which are of the long-high type (2000 and 2011) and medium-low type (2010) has been analysed. With this analysis the aim was to better characterize these events and to better understand their differences. Using the EQPAIR model [69], the evolutions of the optical depth in the non-thermal Comptonizing corona, the seed photon temperature and the hard state compactness parameters were tracked. The results show that independent of the duration and the maximum flux of an outburst, the spectral parameters follow a well defined and reproducible track during the long-high and medium-low type outbursts that are presented here. A typical example of a short-low type outburst is the May 1999 outburst. This outburst was also monitored with the RXTE/PCA and the X-ray spectra was modelled with the EQPAIR model by authors of Ref. [68]. Comparing the spectral evolution during this outburst with the results presented here, it is clearly seen that the optical depth and the compactness parameters evolve in a very similar way. The only difference in the deduced spectral parameters is a slight increase in the seed photon temperature measured at the beginning of the 1999 outburst (see Figure 1. of Ref. [68]), which longer outbursts in our sample do not show.

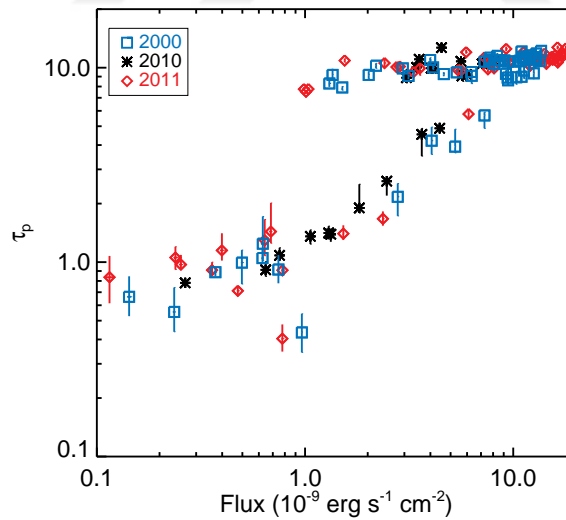


**Figure 3.8 :** Evolution of the scattering optical depth of the corona as a function of unabsorbed source flux. During the outbursts the parameters start from the lower left corner, proceed to the upper right corner during the enhancement stage, remain on the upper horizontal branch during the decay of the outburst and finally drop to the pre-outburst values.

The evolution of the optical depth with flux is shown in Figure 3.8. Once an outburst commences, together and almost simultaneously with the flux, the scattering optical

depth of the corona increases. During the increase the Spearman's rank correlation coefficient between the two parameters is 0.92. This correlation persists till the optical depth reaches a saturation point, which is between 9 to 12 and independent of the peak flux of the outburst. The optical depth remains at the saturation values even during the decline of the outburst and drops to the pre-outburst values with a substantial time delay.

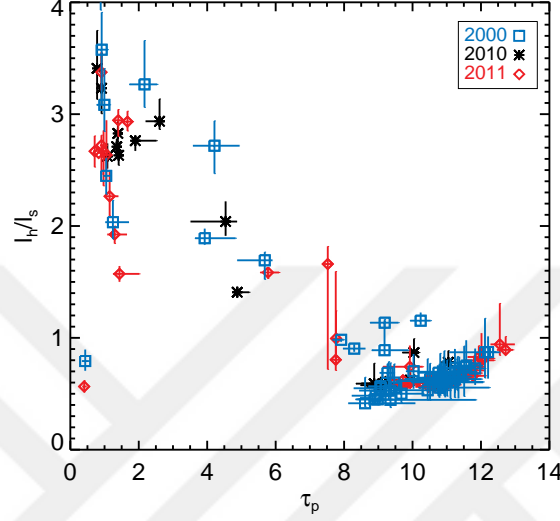


**Figure 3.9** : The relation between the compactness parameter  $l_h/l_s$  and the optical depth of the corona. The data with very large errorbars ( $\Delta(l_h/l_s) > 1$ ) is eliminated.

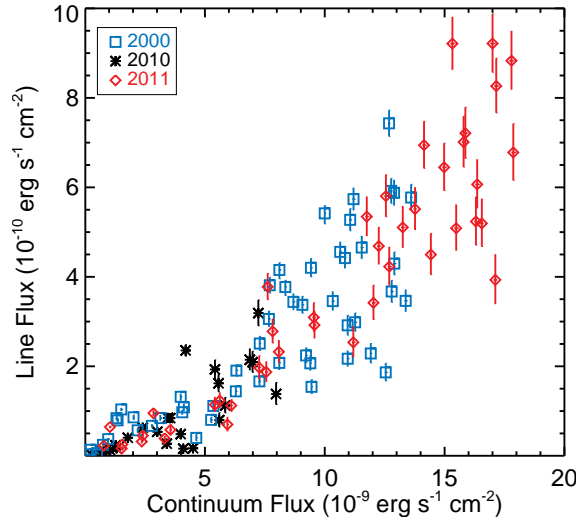


**Figure 3.10** : Variation of unabsorbed flux of the Gaussian iron line component as a with the EQPAIR model flux.

The relation between the compactness parameter  $l_h/l_s$  and the optical depth of the corona has also been investigated as shown in Figure 3.9. The bottom right corner of the figure corresponds to the HS state and upper left corner stands for the LH state. For  $1 < \tau < 10$  the relation is inverse and linear. This less populated region corresponds

to the transitions between these two spectral states. As seen in Figure 3.6,  $l_h/l_s$  shows similar time delay as  $\tau$  does, which is reflected in the linear relation seen in Figure 3.9

The time evolution of the flux of the Gaussian line at  $\approx 6.5$  keV follows a well defined and reproducible trend similar to the flux obtained from the EQPAIR model. Figure 3.10 displays the line flux as a function of the continuum flux. The relation between the flux of the iron line and the continuum flux does not seem to be exactly linear at low fluxes ( $< 6 \times 10^{-9} \text{ erg cm}^{-2} \text{ s}^{-1}$ ). As the flux increases, however, the correlation becomes more linear.

Apart from some exceptions, the X-ray spectral analysis and observations of Type-I X-ray bursts presented here indicate that the peak flux and duration of a given outburst are relatively independent of the region in the X-ray binary that determines the shape of the X-ray spectra. The only difference between the various classes of outbursts seems to be the emitting radius of the seed photons which determines the total observed X-ray flux.



## 4. PARTIAL ACCRETION IN THE PROPELLER STAGE OF AMXPS

### 4.1 Introduction

The transferred matter from companion star has angular momentum and forms an accretion disk rather than falling onto the compact object directly [93] as explained in Sec.1.4. Matter in the bulk of the disk rotates in Keplerian orbits and slowly diffuses inwards while the angular momentum is transported outwards by turbulent viscous processes [47].

If the accreting object is a NS the inner parts of the disk may be disrupted at a location beyond the stellar surface thus forming a magnetosphere. The location of the inner radius of the disk,  $R_{\text{in}}$ , is determined by the balance between the material and magnetic stresses in the disk [94,95] which in turn depend on the mass inflow rate  $\dot{M}$  in the disk, the magnetic dipole moment  $\mu$  and the spin angular velocity  $\Omega$  of the star [96]. Such magnetized star-disk systems (see Ref. [97] for a review) may show three different stages depending on the relation between the inner radius of the disk and two other characteristic radii [98]:

- The *accretion* stage in which  $R_{\text{in}}$  is smaller than the corotation radius  $R_c = (GM/\Omega^2)^{1/3}$  resulting with most (if not all) of the mass flux in the disk to reach to the polar cap of the NS.
- The *propeller* stage [50] in which  $R_{\text{in}} > R_c$  resulting with none (if not a small fraction) of the inflowing mass to reach the surface of the NS due to centrifugal barrier formed by the rapidly rotating magnetosphere within the thin disk assumption.
- The *radio pulsar* stage in which  $R_{\text{in}}$  is even further away from the star, possibly larger than the radius of the light cylinder  $R_L = c/\Omega$ .

The gravitational potential energy of infalling material is transformed to X-ray luminosity:

$$L_X = GMM_*/r_* \quad (4.1)$$

[90] where  $\dot{M}_*$  is the mass accretion rate onto the NS (which may be different than  $\dot{M}$ , the mass flow rate in the disk in unsteady regime) and  $r_*$  is the radius of the star.

A typical X-ray light curve of an outburst of AMXP has a fast rise and an exponential decay. Accordingly,  $\dot{M}$  rises steeply and declines slowly during the outburst within several weeks while magnetic dipole moment and angular velocity of the NS are relatively constant. As  $\dot{M}$  changes these systems may manifest the above mentioned stages of disk-magnetosphere interaction. AMXPs may thus serve as a lab for exploring the transitions between these different stages.

The decay stage of the light curves of AMXPs show a knee marking the transition from a slow decline to as a rapid decline stage (e.g. Ref. [77]). It is suggested by the authors of Ref. [59, 60, 74] that this knee may be due to transition of the system from the accretion stage to the propeller stage. The detection of the pulsations even at very low luminosities that the system would be expected to be well in the propeller stage may indicate that the “propeller effect” is not ideal but a fraction

$$f \equiv \dot{M}_*/\dot{M} \quad (4.2)$$

of the inflowing mass reaches the surface of the star [61, 99, 100]. This fraction would be a function of the fastness parameter of the system

$$\omega_* \equiv \Omega/\Omega_K(R_{\text{in}}) = (R_{\text{in}}/R_c)^{3/2} \quad (4.3)$$

[101] where  $\Omega_K = \sqrt{GM/R^3}$  is the Keplerian angular velocity. In the simplest picture of an ideal propeller surrounded by a infinitely thin disk  $f$  is a step function

$$f = \begin{cases} 1, & \text{for } \omega_* \leq 1 \\ 0, & \text{for } \omega_* > 1 \end{cases} \quad \text{ideal propeller.} \quad (4.4)$$

In real disks with finite scale-height,  $H$ , a regime of partial accretion may be realized in which  $f$  is expected to change smoothly with  $\omega_*$ . This is because accretion can proceed from higher latitudes of the disk even while the disk midplane is propelled. Indeed, the disk may become thicker to allow for such accretion as the fastness parameter goes above unity, or transition to the propeller stage may be induced as a result of the

evaporation and thickening of the inner disk. The smoothness of the transition will be a measure of  $H(R_{\text{in}})/R_{\text{in}}$ . Being a dimensionless function of a dimensionless parameter  $f = f(\omega_*)$  should be unique for different outbursts of a system. In general  $f$  may also depend on the inclination angle between the rotation and magnetic axis and so may vary for different systems. Theoretical estimates for  $f(\omega_*)$  were presented by authors of Ref. [102] for spherical accretion and by authors of Ref. [79] for the disk accretion case who showed that  $f = (3/8)\omega_*^{-4}$  for the  $\omega_* \gg 1$  limit. The general case was investigated by authors of Ref. [78] with an application to SAX J1808.4–3658. In this thesis, We attempt to extract  $f = f(\omega_*)$  from observations. The RXTE observations of a  $\nu = 550.27$  Hz AMXP, Aql X–1 [29] are investigated, to identify transition from the propeller stage into the accretion regime. Using the detected value of the spin frequency of Aql X–1, the radius of the light cylinder ( $R_L$ ) and the corotation radii are  $R_L = 8.7 \times 10^6$  cm and  $R_c = 2.5 \times 10^6$  cm, respectively.

## 4.2 Observation and Data Analysis

The detected X-ray luminosity originates from the NS pole and the inner parts of the disk. In order to separate these two components we performed a spectral analysis. The most luminous outbursts of Aql X–1 are the 2000, the 2003, the 2011 and the 2013 outbursts. For the 2000 and the 2011 outbursts, RXTE/PCA observations were performed covering the outburst with 52 and 51 targeted observations, respectively, after the data with thermonuclear bursts and the saturated data with very low S/N ratio are eliminated. As for 2013, we analysed 31 SWIFT/XRT data in windowed-timing mode to obtain the physical parameters and the light curves for each component. The observations well cover the entire duration of the outbursts i.e. the fast rising, the slow decay and the fast decay phases.

We analysed the RXTE/PCA data using HEASOFT<sup>1</sup> version 6.17. Since Aql X–1 is a very bright source in the X-ray band, we used only PCU2 (proportional counter unit) which is always active. We created the response files for each observation using PCARSP version 11.7.1 and we used the latest module file<sup>2</sup> for creating background models. The data reduction of SWIFT/XRT for the 2013 outburst were done using

<sup>1</sup><https://heasarc.gsfc.nasa.gov/docs/software/lheasoft/> version 6.17

<sup>2</sup>pca\_bkgd\_cmbrightvle\_eMv20051128.mdl

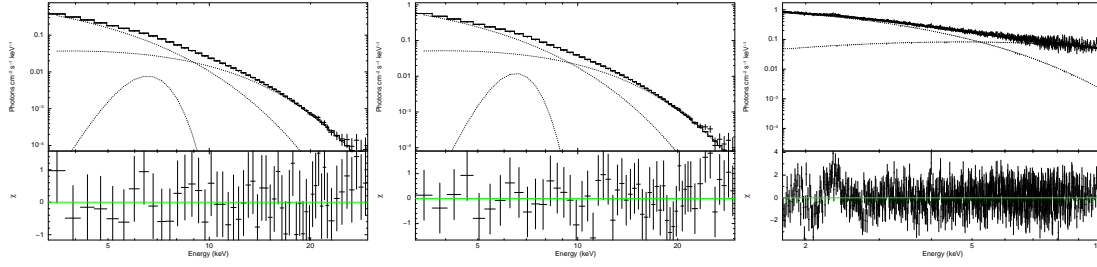


**Figure 4.1 :** The X-ray spectrum of Aql X–1 during outburst. The left and middle panels show the spectra obtained by RXTE/PCA in the 3.0 – 30.0 keV energy range during the 2000 (ObsID 50049-02-08-03) and 2011 (Obs ID 96440-01-05-01) outbursts, respectively. The right panel shows SWIFT/XRT the spectra during 2013 (00035323008) outburst in the 0.5 – 10.0 keV energy range. The best fits are obtained by using the *bb+diskbb+(ga)* model. Lower panels show the residuals in terms of sigma.

xrtpipeline<sup>3</sup>. As Aql X–1 is a luminous source it was sufficient to run xrtpipeline with the default values. Accordingly, timing bin size of 1.0 s and a circular region with radii of 20 pixels were used to extract the data.

All spectra were modelled using XSPEC package<sup>4</sup>. We modelled the spectra in a range of 3.0 – 30.0 keV for RXTE/PCA data and 0.5 – 10.0 keV for SWIFT/XRT data. These energy ranges are the most sensitive parts for each detector. We added a 1.0% systematic error to take into account internal gain.

#### 4.2.1 Model I: Black body assumption

We first modelled all spectra using a combination of black body, disk black body and a Gaussian component. The black body component (*bbody* in XSPEC) represents the X-ray emission originating from the hot spot at the pole of the NS fed by accretion. The disk black body component (*diskbb* in XSPEC) represents the X-ray contribution of the inner layers of the accretion disk. After determining the best fit parameters for *black body + disk black body* model for the RXTE/PCA data, a Gaussian line is added to represent the iron line. Addition of this line was not statistically necessary for the SWIFT/XRT data. We used a constant neutral hydrogen column density of  $N_{\text{H}} = 3.4 \times 10^{21} \text{ atoms cm}^{-2}$  [68] using the model by [103, *phabs* in XSPEC]. In Figure 4.1, we show an example of the fits we performed for each data set. The left,

<sup>3</sup>UK Swift Science Data Centre; <http://www.swift.ac.uk/analysis/xrt/xrtpipeline.php>

<sup>4</sup>An X-Ray Spectral Fitting Package v12.8.2, <https://heasarc.gsfc.nasa.gov/xanadu/xspec/>



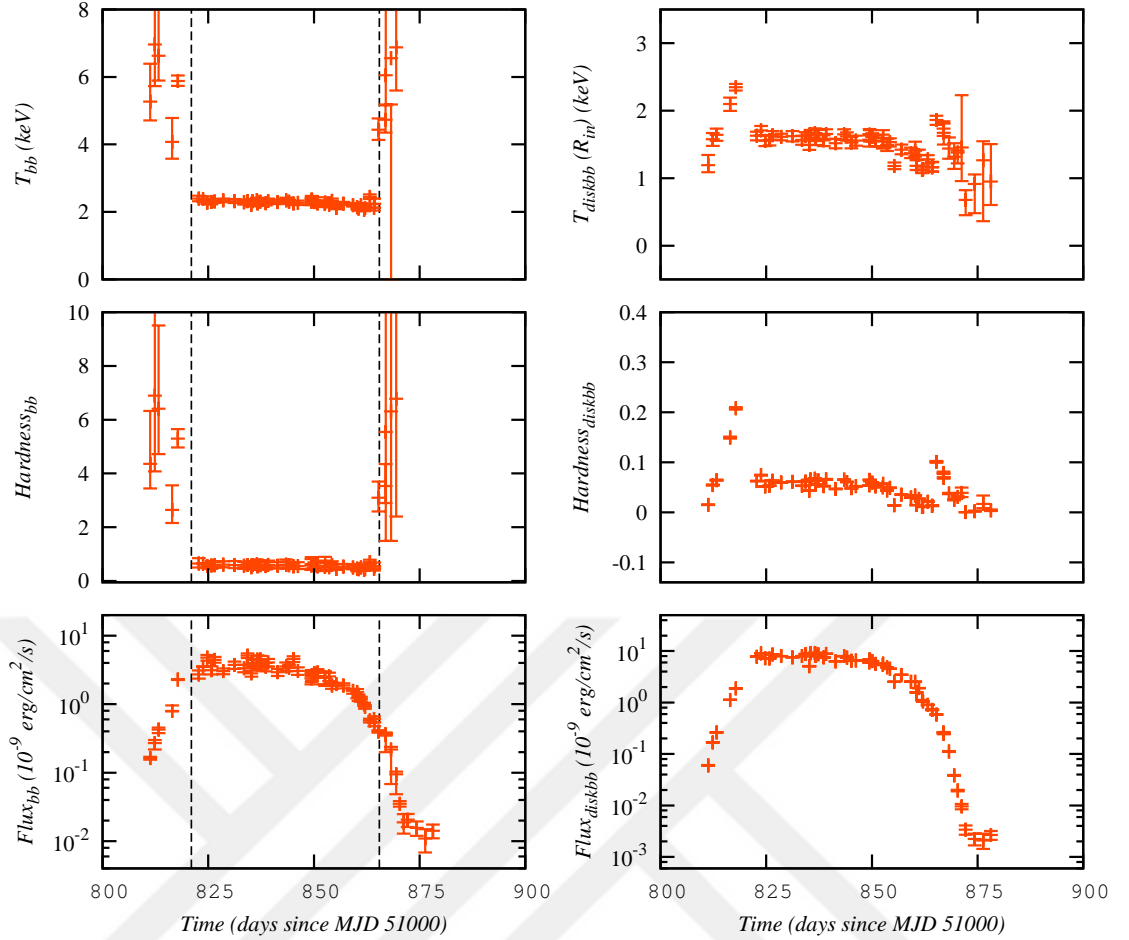


**Figure 4.2** : Evolution of spectral parameters during 2000 outburst of Aql X-1. The top panels show the time evolution of the black body temperature (left) and the inner disk temperature of disk black body component (right). The middle panels show time evolution of the hardness parameter only for black body component (left) and only for disk black body component (right). The bottom panels show the evolution of the flux of the black body component (left), and the disk black body component (right).

middle and right panels of Figure 4.1 show the 2000 (ObsID: 50049-02-08-03), 2011 (ObsID: 96440-01-05-01) and 2013 (ObsId: 00035323008) outbursts, respectively. The residuals in terms of standard deviation ( $\sigma$ ) are presented for each spectrum at the bottom of panel. The two peaks seen in residuals of SWIFT/XRT data (the right panel of Figure 4.1) around 2.0 keV could be fixed by adding two edge components [104]. We, however, tried to avoid using edge components to better characterize the black body component.

We calculated the unabsorbed fluxes for the best fit of the X-ray spectra using *black body + disk black body + Gaussian* model for the black body and the disk black body components, separately in the range of 3.0 – 30.0 keV ( $F_{3-30}$ ) for RXTE/PCA data.

Bottom left and bottom right panels of Figure 4.2 and Figure 4.3 show the light curves for each component of the 2000, the 2011 outburst, respectively. Since both of the outbursts belong to the same class mentioned in Section 3.2, the *long-high* outbursts, with similar maximum flux level and outburst duration, the intensities of accretion are similar for each outburst. This means that the amount of the matter accumulated in the disk, thereupon the inner radii of the disks, a mount of the matter being transferred to the NS poles and the contributions of the illuminated halo of the accretion disks for each class are comparable. Therefore, the ratios of the NS flux and the disk flux ( $L_*/L_{\text{disk}}$ ) for the 2000 and 2011 outburst are similar (Figure 4.2 and Figure 4.3).

Moreover, by taking a *pivot* energy ( $E_{\text{pivot}} = 10$  keV)—the critical energy separating the soft and the hard components—we computed the fluxes for 3.0 – 10.0 keV ( $F_{3-10}$ ) and 10.0 – 30.0 keV energy ranges ( $F_{10-30}$ ), following Ref. [60]. We then obtained the hardness evolution using the ratio of  $F_{10-30}/F_{3-10}$  (Figure 4.2 and Figure 4.3 middle left, middle right). The free parameters of the black body and the disk black body are the temperature of the black body component ( $T_{\text{bb}}$ ), the inner disk temperature of the disk black body component ( $T_{\text{diskbb}}(R_{\text{in}})$ ) and the normalisations of the models. We show the evolution of  $T_{\text{bb}}$  (top left) and  $R_{\text{diskbb}}(R_{\text{in}})$  in keV in upper panels of Figure 4.2 and Figure 4.3. We provide the final model parameters in Table B.1 and Table B.2 for the 2000 and 2011, respectively.

Since the most sensitive energy range of SWIFT/XRT is different, we calculated the fluxes in the range of 0.5 – 10.0 keV ( $F_{0.5-10}$ ) (Figure 4.4 bottom panel). We calculated the hardness evolution by taking the  $E_{\text{pivot}}$  of each 0.1 keV energy step from 1.0 keV to 6 keV to search the most effective  $E_{\text{pivot}}$  ( $F_{E_{\text{pivot}}-10}/F_{0.5-E_{\text{pivot}}}$ ,  $1.0 \leq E_{\text{pivot}} \leq 6.0$ ,  $dE = 0.1$ ). Although, we obtained the best hardness evolution using the *pivot* energy of 1.8 keV with the least errors, the state transitions in the 2013 outburst were not obvious as in the RXTE/PCA data of the 2000 and the 2011 outbursts. We hereby, computed the hardness evolution using the count rates of SWIFT/XRT via the same *pivot* energy (Figure 4.4 middle panel) and checked the ratio of MAXI count rates between 10.0 – 20.0 keV to 2.0 – 4.0 keV (Figure 4.4 top panel).

In both components, we see that the spectral parameters evolve in a similar way but the black body component is more accurate at higher luminosities. As the outburst starts,  $T_{\text{bb}}$  drops down to reach  $\sim 2$  keV and the hardness ratio of black body decreases to  $\sim 1$

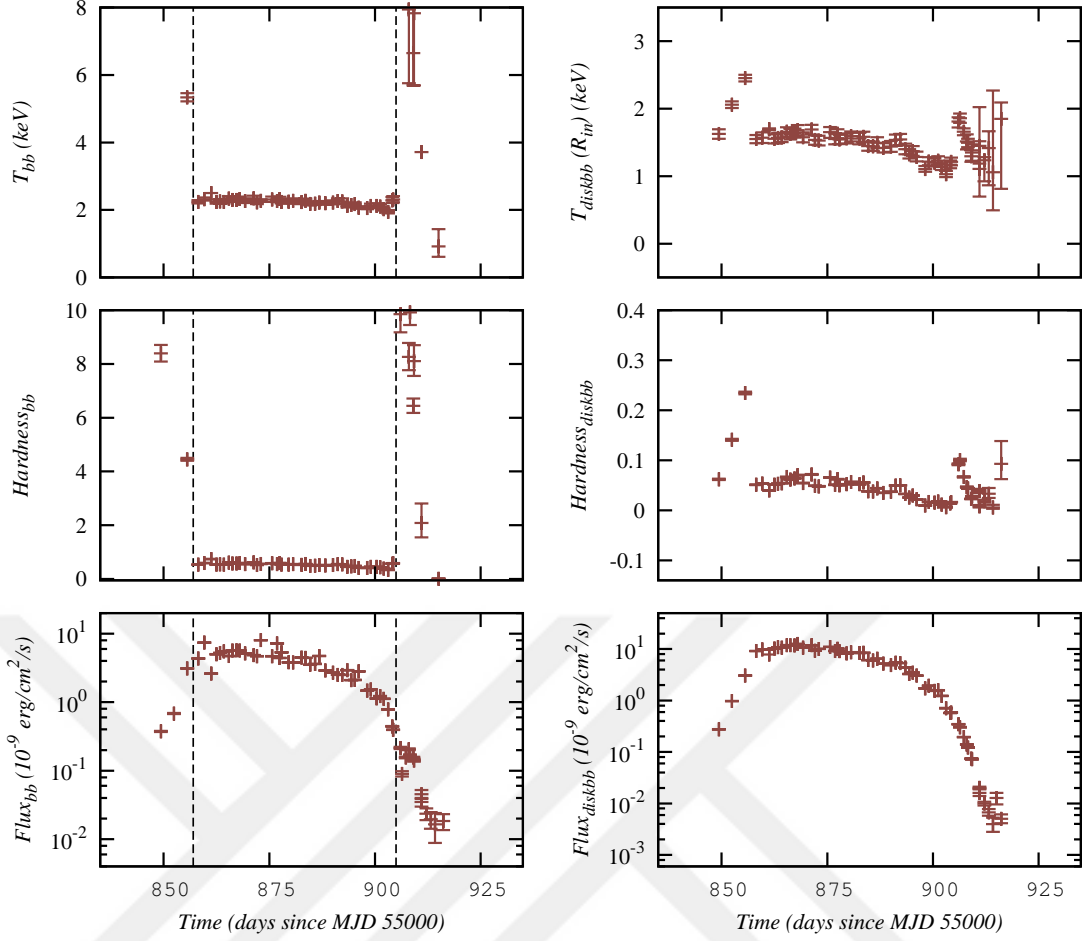


**Figure 4.3** : Same as Figure 4.2 but for the RXTE/PCA data during 2011 outburst of Aql X-1.

at the maximum of outburst, and both parameters stay stable until the propeller stage. This is the transition from the LH state to the HS state [46]. Before the outburst ends and the system passes to the quiescent stage, the hardness decreases to pre-outbursts level. On the other hand, this transition occurs simultaneously with the “knee” of the light curve well before quiescent stage. These critical instants (vertical dashed lines in Figure 4.2 and Figure 4.3) are used as the beginning and the terminal of the accretion stage which are also used as the fit range in our method described in section 4.3. Authors of Ref. [105] argued that the transition in the hardness evolution is caused by the *propeller effect* [50]. Because of the narrower energy range of SWIFT/XRT, hardness parameters are not sensitive as they are in RXTE/PCA. Therefore, specifying the accretion stage from the hardness evolution is not possible. So, we determine the maximum of the outburst and the knee by the dramatic change in the light curve of 2013 outburst.

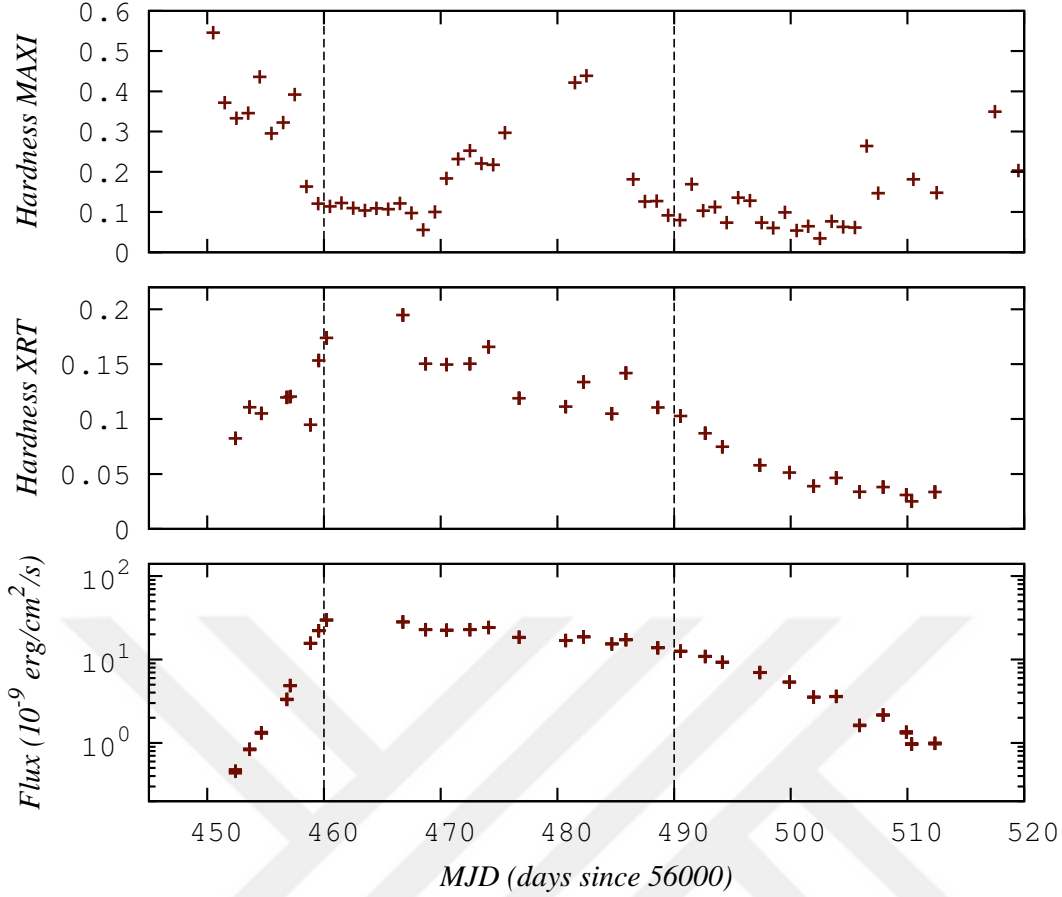


**Figure 4.4** : SWIFT/XRT light curve of the 2013 outburst of Aql X-1 in the energy range of 0.5 – 10.0 keV (bottom panel). The time evolution of hardness parameter using the ratio of SWIFT/XRT count rates of 1.8 – 10.0 keV to 0.5 – 1.8 keV energy ranges (middle panel) and the one using the ratio of MAXI count rates of 10.0 – 20.0 keV to 2.0 – 4.0 keV energy ranges.

#### 4.2.2 Model II: Comptonised black body assumption

Even if the black body assumption works in many cases, the upscattering of the photons by the coronal electrons must also be taken into account. We checked the role of Comptonisation by modelling all spectra in the LH state and few examples in the HS state corresponding to accretion using a similar combination as model I adding a Comptonisation model (*comptTT* in XSPEC, [106]) in which the Wien temperature of the Comptonisation model is linked to the temperature of the black body model under the assumption that protons from the NS pole act as the seed for inverse Compton process. For the X-ray contribution of the heated inner disk layers, we added the disk black body component just as we did in model I. We added the Gaussian emission line component to account for Fe line emission in cases it was statistically necessary. The input parameters of the disk black body component to the fit are taken from the

resulting fit of model I to better constrain the Comptonization effect on the black body component.

We provide resulting parameters of model II analysis in Table C.1 and Table C.2 for the 2000 and the 2011 outbursts, respectively. We tracked the time evolution of the optical depth ( $\tau$ ) during outburst. The variance of the parameters  $\tau$  and hardness of the black body component implies that Comptonisation becomes ineffective in the high-soft state. It is possible to interpret this simply by suggesting that the disk penetrates and dominates the total X-ray flux leading to the lack of Comptonisation contribution during the accretion phase. The result implies that the black body component is sufficient for representing the accretion phase. We will then assume that the light curve of the black body component represents the time evolution of the luminosity of accretion onto the NS poles. This assumption is necessary for the application of the technique that we present in the next section.

### 4.3 The Partial Accretion Regime of Outbursts

Here, we propose a simple method for extracting  $f(\omega_*)$  from the light curve,  $L_X(t)$ . The method is based on three assumptions:

- The rapid decay stage is a consequence of transition of the system to the propeller stage  $\omega_* > 1$  and is not due to irradiation or any other process.
- The decay of the mass inflow rate  $\dot{M}$  continues its evolution with no modification upon the transition of the system from accretion to the propeller stage though a smaller fraction of it can now accrete onto the star leading to the appearance of rapid decline.
- The angular velocity  $\Omega$  and magnetic moment  $\mu$  of the neutron star does not change significantly during an outburst.

We also assume  $f = 1$  (meaning that  $\dot{M}_* = \dot{M}$ ) in the accretion stage before the knee. Soon after the maximum is reached the disk establishes a quasi-equilibrium stage which evolves self-similarly [107–109] where the mass flux and hence the luminosity will evolve as a power-law:

$$L(t) = L_0 \left[ 1 + \left( \frac{t - t_0}{t_v} \right) \right]^{-\alpha}, \quad t_0 < t < t_{\text{knee}}. \quad (4.5)$$

Here  $L_0$  is the luminosity at the moment of  $t_0$ ;  $t_{\text{knee}}$  is the corresponding time since the start of the fast decay phase;  $t_v$  is the time-scale of the outburst decay (viscous timescale) and  $\alpha \simeq 1.25$  depending on the opacity prevailing in the disk [78, 110]. We first fit the region between the maximum of the light curve and the knee using Equation 4.5 to determine  $L_0$ ,  $t_0$  and  $t_v$ . We have fixed  $\alpha = 1.25$  appropriate for a gas pressure dominated disk with bound-free opacity.

The inner radius,  $R_{\text{in}}$ , is determined by the equilibrium of magnetic and material stresses. This is proportional to the Alfvén radius which is defined as the location at which magnetic pressure and ram pressure are balanced;

$$R_A = \left( \frac{\mu^4}{2GM\dot{M}^2} \right)^{1/7} \propto \dot{M}^{-2/7}. \quad (4.6)$$

Thus by Eq.4.3 we obtain  $\omega_* \propto \dot{M}^{-3/7}$  or rather

$$\omega_* = (\dot{M}/\dot{M}_c)^{-3/7} \quad (4.7)$$

where  $\dot{M}_c$  is the mass inflow rate that would place the inner radius on the corotation radius. Similarly

$$\omega_* = (L/L_c)^{-3/7} \quad (4.8)$$

where  $L_c$  is the luminosity at which rapid decay starts. In the propeller stage we assume that the mass inflow rate determining the inner radius continues with the same trend. Thus if all this inflowing matter could accrete we would have a luminosity continuing with the same trend of the accretion stage with no knee. The presence of the knee is assumed to be a consequence of partial accretion in the propeller stage: thus a fraction  $f$  of  $\dot{M}$  can accrete. We thus determine  $f(t)$  by dividing the observed light curve with luminosity obtained via Eq.4.5. Accordingly the fastness parameter will evolve as

$$\omega_*(t) = \left( \frac{L_0}{L_c} \right)^{-3/7} \left( 1 + \frac{t-t_0}{t_v} \right)^{3\alpha/7}. \quad (4.9)$$

By eliminating time,  $t$ , between  $\omega_*(t)$  and  $f(t)$  one can obtain a parametric plot of  $f(\omega_*)$ . Once the data is converted to  $f(\omega_*)$  we fit the resulting data with a smoothed step function that varies between from unity to  $f_{\text{min}} < 1$ :

$$f(\omega_*) = \frac{1}{2} \left[ 1 + f_{\text{min}} + (1 - f_{\text{min}}) \tanh \left( \frac{\omega_c - \omega_*}{\delta} \right) \right] \quad (4.10)$$

where  $w_c \simeq 1$  and  $\delta$  are free fit parameters. The method presumes that the X-ray luminosity arises from the polar cap, yet the inner disk may also contribute to the X-ray emission. In order to find the X-ray luminosity arising from the polar cap only we employed a spectral analysis (in Sec.4.2) to obtain the X-ray light curve of the polar cap and the disk, separately, during an outburst.

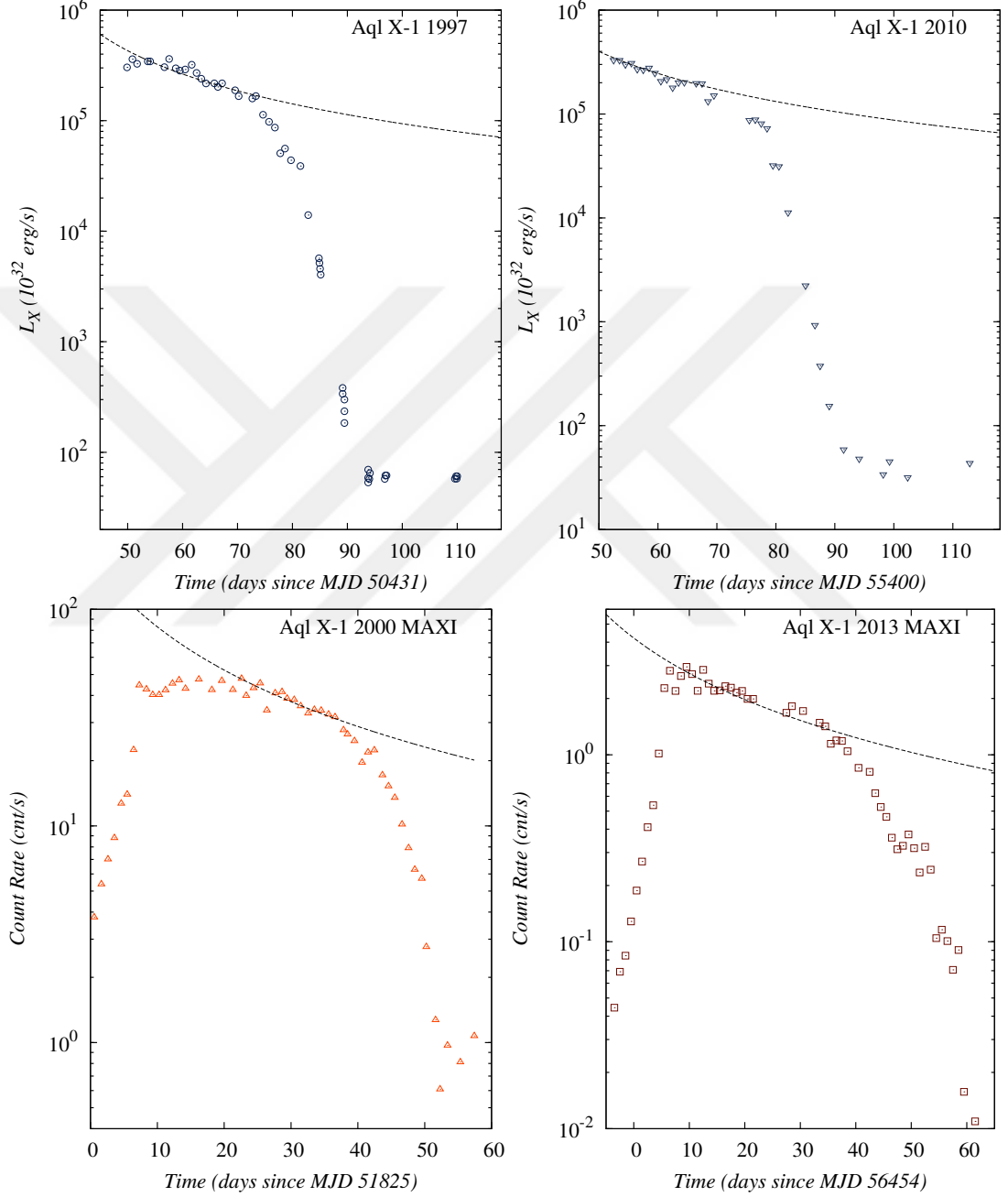


**Figure 4.5 :** X-ray light curves of the 1997 (the upper-left panel), the 2010 (the upper right panel), the 2000 (the bottom left panel) and the 2013 (the bottom right panel) outbursts together with the best fit of Eq.4.5 between maximum of outbursts and the knee.

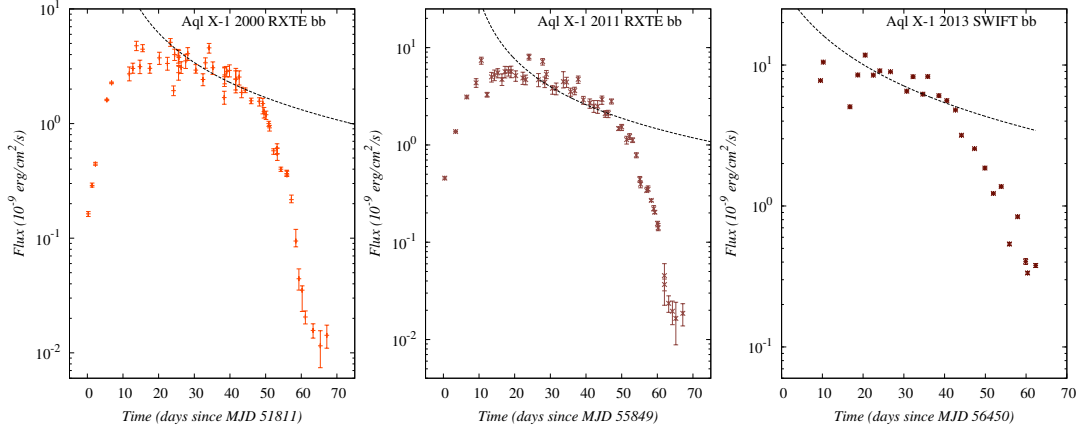


**Figure 4.6 :** X-ray light curves of black body component of the 2000 (the left panel), the 2011 (the middle panel) and the 2013 (the right panel) outbursts together with the best fit of Eq.4.5 between the maximum and the knee.

#### 4.4 Applications

The decay stages of the 1997 and the 2010 outbursts of Aql X–1 have been studied by authors of Ref. [59] and Ref. [111] who concluded that the rapid decay stage is probably caused by transition to the propeller stage. Although, both outbursts belong to the *medium-low* class and are not the most luminous ones, their durations are similar to *long-high* class [112]. In addition to the MAXI light curve of the 2000 and 2013 outbursts of Aql X–1, we applied the procedure described in Sec.4.3 to the 1997, the 2010, the 2000 and 2013 outbursts to calculate the fraction of mass flux reaching the NS in the propeller stage. In Figure 4.5, we show the light curves of the 1997 outburst (the left panel) and the 2010 outburst (the second panel) taken from Ref. [111] together with the MAXI light curve of the 2000 (the third panel) and the 2013 (the right panel) outbursts. The best fit values of  $t_v$  are determined as 50.0, 51.0, 25.0 and 23.5 days for the 1997, the 2010, the 2000 and the 2013 outbursts, respectively.

After performing the spectral analysis and obtaining the light curves only for black body components explained in Sec.4.2.1, we followed the same procedure and determined the  $\dot{M}_*/\dot{M}$  in the propeller stage. In Figure 4.6, we show the best fit curves of Eq.4.5 for the 2000 (left panel), the 2011 (middle panel) and the 2013 (right panel) outbursts. We have subtracted 51811, 55849 and 56450 days from the MJD dates for the 2000, the 2011 and the 2013 outbursts, respectively. The best fit values of  $t_v$  for each outburst are determined as 16.0, 23.5 and 19.5 days, respectively.



## 4.5 Results and Discussion

By using the method described in Sec.4.3, we obtained  $f \equiv \dot{M}_*/\dot{M}$  vs  $\omega_*$  for the black body light curves of 2000, 2011 and 2013 outbursts. We also added the light curves of the 1997 and the 2010 outbursts from Ref. [111] and the MAXI light curve of the 2000 and the 2013 outbursts. In Figure 4.7, we show the results fitted with the phenomenological model Eq.4.10. As seen in Figure 4.7, for outbursts belonging to the *medium-low* class  $f$  has a steeper fastness parameter dependence compared to  $f$  of the outbursts that belong to the *long-high* class. The physics behind this picture can be summarised as follows;

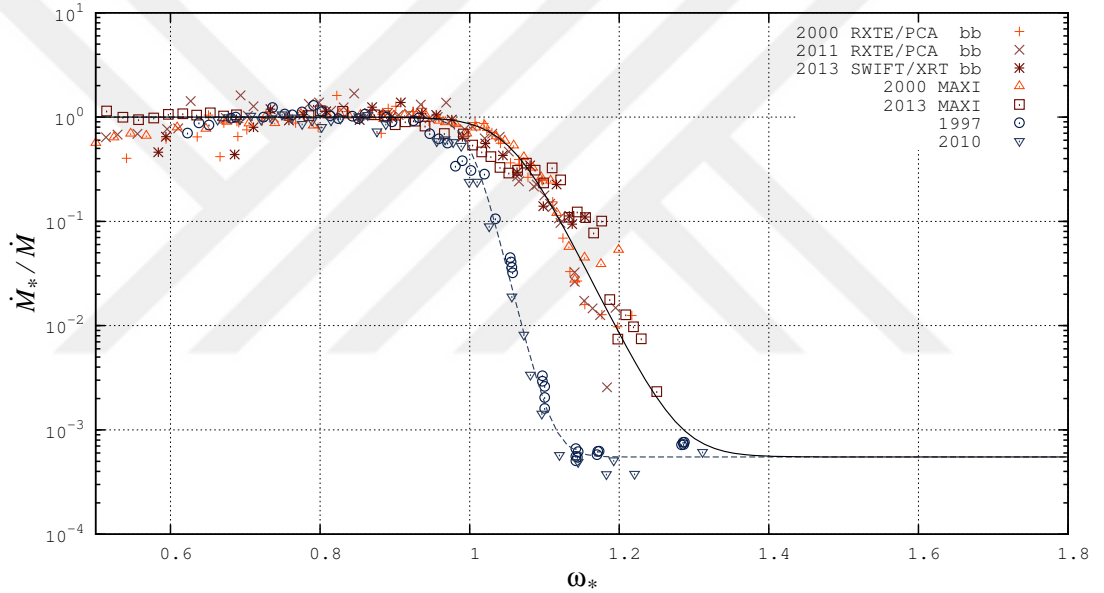


**Figure 4.7 :**  $\dot{M}_*/\dot{M}$  vs the fastness parameter relation of the outbursts of Aql X-1. Smoothed step functions show the best fit of Equation 4.10 using MAXI data (blue curve) and black body component of RXTE/PCA and SWIFT/XRT data (black curve).

- The range  $\omega_* \lesssim 0.6$  corresponds to the rising phase of the outburst. It should not be taken in consideration that  $f < 1$  in this case. The material in the disk is transferred from the outer layers of the disk to the inner layers, therefore  $R_{\text{in}}$  approaches to NS and penetrates into  $R_c$ .
- The range  $0.6 \lesssim \omega_* \lesssim 1.0$  is the accretion stage. All of the material transferred from outer disk accretes onto the NS. As  $\dot{M}$  ( $= \dot{M}_*$  in accretion stage) decreases in time, the luminosity declines (slow decay stage) while  $R_{\text{in}}$  expands back to  $R_c$ .

- The range  $1.0 \lesssim \omega_* \lesssim 1.4$  is the partial accretion regime. The values of  $\delta$  we determined by fitting the data are 0.03 and 0.06 for the *medium-low* and *long-high* classes, respectively. This can be attributed to the inner disk being thicker in the *long-high* class outbursts as a result of higher density of inner disk in the propeller regime.
- The range  $\omega_* \gtrsim 1.4$  is the radio pulsar stage. After all of the material inner then  $R_c$  is totally accreted onto the poles of NS,  $R_{in}$  expands and becomes greater than  $R_L$ . The system shows no evidence of accretion in the X-ray light curve and acts like an isolated NS.

Some outbursts of X-ray binary systems show fluctuations in their X-ray light curves after the main outburst terminates. A clear example of such fluctuations can be seen in the 2002 outburst of SAX J1808.4–3658 (see Figure 1 in Ref. [77]). One of the open questions about partial accretion in the propeller stage is what happens to the incoming material which is not transferred to NS poles (non-accreted materials) since only a fraction of it may accrete. The technique presented in this thesis may also clarify this question by allowing to calculate mass fraction rate and the time evolution of the mass transfer rate from outer layers to inner layer. As a first impression, the peaks of the fluctuations are following the trend of the slow decay stage, described by Eq.4.5 in our work, as it shows the time evolution of the mass transfer rate along disk layers. For the future of the non-accreted materials after the main outbursts, in other words the first penetration of the disk to the corotation radius, two possible scenarios come to mind: (i) The non-accreted materials may be thrown to the outer layers of the disk rather than to fall onto NS poles and transferred to inner layers again. In this situation, the time scale of the fluctuations is related to the radius at which the material is thrown and the mass transfer speed along disk. (ii) If the penetration of the inner radius of the disk to corotation radius occurs as a result of wavelike motion, fluctuations may be outcome of wave reflections from the edges of the disk. In this scenario, the time scale of fluctuations indicates the wave travel duration between the inner radius and the outer radius of the disk. A combination of two scenarios could happen as the thrown material creates new shock on the outer layers of the disk and matter is transferred via wave to inner layer which causes the penetration and constitute the fluctuations in the light curve.

## 5. CONCLUSION

For the first time in literature, we presented a broad classification of the outbursts of Aql X-1. Based on the duration and maximum flux, we identified three types of outbursts, *long-high*, *medium-low* and *short-low*. In terms of total energy released, the *long-high* outbursts overwhelms the others.

We analysed the spectral evolution throughout three outbursts of Aql X-1 observed by RXTE, the 2000, 2010 and 2011, using the EQPAIR model. The 2010 outburst is a member of the medium-low type while 2000 and 2011 outbursts are members of the long-high type. These outbursts, together with the 1999 outburst analysed by authors of Ref. [68] which is of the short-low type, give us an opportunity to discuss the three types of outbursts analysed with the same method. Our spectral analysis shows that all of the inferred parameters evolve in a very similar way regardless of the different classes of the outbursts, with only difference being the maximum flux. This implies that the ingredient in the X-ray binary that shapes the observed X-ray spectra is not the cause of the different outburst types.

Irradiation of the disk modulates the disk size involved in the outbursts thereby leading to different luminosities in different classes. We showed a correlation between the maximum flux and the outer radius of the disk inferred by [63] which demonstrates the role of irradiation as the main cause for the different peak luminosities. We argued that the transition to the propeller or partial accretion regime induced by transition to a geometrically thick disk might contribute to the diversity in the observed light curve morphology.

We analysed the RXTE/PCA data during the 2000, the 2011 outbursts and SWIFT/XRT data during the 2013 outburst of Aql X-1. We modelled each spectra using a combination of black body and disk black body to take into consideration the contribution of the disk to X-ray luminosity. We calculated fluxes for each component separately. Furthermore, we investigated the time evolution of the spectral parameters for each model. At this point, it could be argued whether

the black body component represents the hot spot on the NS poles well, since the Comptonisation effect would be important. Different models could be employed to separate contributions from different components in the total X-ray flux that we observe (e.g. *nthcomp(black body)+diskbb*, [104]). We checked the black body assumption by using a Comptonisation model in which Wien temperature parameter is linked to the black body temperature. It is shown that Comptonisation is not significantly effective during the accretion phase which supports the idea of that accretion is represented by the black body radiation.

By using only the black body light curves for these three outbursts, we transformed the flux to the ratio of  $\dot{M}_*/\dot{M}$  and time scale to fastness parameter. We then compared all of the outbursts in this picture. We fit the result using a phenomenological function given in Eq.4.10. We showed that different outbursts in the long-high class with different time scales and maximum fluxes follow the same trend. Accordingly, the step function representing the outbursts in  $f - \omega_*$  scene must be a universal function for a unique system and it must be related to the ratio of the thickness of the inner layers of the disk to the inner radius of the disk and/or the inclination between the magnetic field and the spin axis of the NS.

This work can be extended to different types of X-ray binaries. More systems and more outbursts will allow to compare the results and link our work to morphology of the disk.

## REFERENCES

- [1] **Lattimer, J.M. and Prakash, M.** (2007). Neutron star observations: Prognosis for equation of state constraints, *Physics Reports*, 442, 109–165, astro-ph/0612440.
- [2] **Chadwick, J.** (1932). Possible existence of a neutron, *Nature*, 129, 312.
- [3] **Baade, W. and Zwicky, F.** (1934). Remarks on Super-Novae and Cosmic Rays, *Phys. Rev.*, 46, 76–77.
- [4] **Hewish, A., Bell, S., Pilkington, J., Scott, P. and Collins, R.** (1968). Observation of a rapidly pulsating radio source, *Nature*, 217, 709–713.
- [5] **Page, D.P.**, <http://www.astrosu.unam.mx/neutrones/NS-Picture/NStar/NStar.html>, date: 10.08.2016.
- [6] **Oppenheimer, J.R. and Volkoff, G.M.** (1939). On Massive Neutron Cores, *Phys. Rev.*, 55, 374–381.
- [7] **C., T.R.** (1939). On Massive Neutron Cores, *Phys. Rev.*, 55, 364–374.
- [8] **Demorest, P.B., Pennucci, T., Ransom, S.M., Roberts, M.S.E. and Hessels, J.W.T.** (2010). A two-solar-mass neutron star measured using Shapiro delay, *Nature*, 467, 1081–1083, 1010.5788.
- [9] **Harding, A.K.** (2013). The neutron star zoo, *Frontiers of Physics*, 8, 679–692, 1302.0869.
- [10] **Verbunt, F.** (1993). Origin and evolution of X-ray binaries and binary radio pulsars, *ARA&A*, 31, 93–127.
- [11] **Bradt, H.V.D. and McClintock, J.E.** (1983). The optical counterparts of compact galactic X-ray sources, *ARA&A*, 21, 13–66.
- [12] <http://hemel.waarnemen.com/Informatie/Sterren/hoofdstuk6.html#mtr>, date: 10.08.2016.
- [13] **Bildsten, L., Chakrabarty, D., Chiu, J., Finger, M.H., Koh, D.T., Nelson, R.W., Prince, T.A., Rubin, B.C., Scott, D.M., Stollberg, M., Vaughan, B.A., Wilson, C.A. and Wilson, R.B.** (1997). Observations of Accreting Pulsars, *ApJS*, 113, 367–408, astro-ph/9707125.
- [14] **Hayakawa, S.** (1985). X-rays from accreting neutron stars, *Physics Reports*, 121, 317–406.

- [15] **Cumming, A., Zweibel, E. and Bildsten, L.** (2001). Magnetic Screening in Accreting Neutron Stars, *ApJ*, 557, 958–966, astro-ph/0102178.
- [16] **Backer, D.C., Kulkarni, S.R., Heiles, C., Davis, M.M. and Goss, W.M.** (1982). A millisecond pulsar, *Nature*, 300, 615–618.
- [17] **Alpar, M.A., Cheng, A.F., Ruderman, M.A. and Shaham, J.** (1982). A new class of radio pulsars, *Nature*, 300, 728–730.
- [18] **Radhakrishnan, V. and Srinivasan, G.** (1982). On the origin of the recently discovered ultra-rapid pulsar, *Current Science*, 51, 1096–1099.
- [19] **Wijnands, R. and van der Klis, M.** (1998). A millisecond pulsar in an X-ray binary system, *Nature*, 394, 344–346.
- [20] **in 't Zand, J.J.M., Heise, J., Muller, J.M., Bazzano, A., Cocchi, M., Natalucci, L. and Ubertini, P.** (1998). Discovery of the X-ray transient SAX J1808.4-3658, a likely low-mass X-ray binary, *A&A*, 331, L25–L28, astro-ph/9802098.
- [21] **Markwardt, C.B., Swank, J.H., Strohmayer, T.E., in 't Zand, J.J.M. and Marshall, F.E.** (2002). Discovery of a Second Millisecond Accreting Pulsar: XTE J1751-305, *ApJ*, 575, L21–L24, astro-ph/0206491.
- [22] **Remillard, R.A., Swank, J. and Strohmayer, T.** (2002). XTE J0929-314, *IAU Circ.*, 7893.
- [23] **Markwardt, C.B., Smith, E. and Swank, J.H.** (2003). XTE J1807-294, *IAU Circ.*, 8080.
- [24] **Falanga, M., Bonnet-Bidaud, J.M., Poutanen, J., Farinelli, R., Martocchia, A., Goldoni, P., Qu, J.L., Kuiper, L. and Goldwurm, A.** (2005). INTEGRAL spectroscopy of the accreting millisecond pulsar XTE J1807-294 in outburst, *A&A*, 436, 647–652, astro-ph/0503292.
- [25] **Markwardt, C.B. and Swank, J.H.** (2003). XTE J1814-338, *IAU Circ.*, 8144.
- [26] **Eckert, D., Walter, R., Kretschmar, P., Mas-Hesse, M., Palumbo, G.G.C., Roques, J.P., Ubertini, P. and Winkler, C.** (2004). IGR J00291+5934, a new X-ray transient discovered with INTEGRAL, *The Astronomer's Telegram*, 352.
- [27] **Morgan, E., Kaaret, P. and Vanderspek, R.** (2005). HETE J1900.1-2455 is a millisecond pulsar, *The Astronomer's Telegram*, 523.
- [28] **Markwardt, C.B., Krimm, H.A. and Swank, J.H.** (2007). SWIFT J1756.9-2508 is a 182 Hz Millisecond X-ray Pulsar, *The Astronomer's Telegram*, 1108.
- [29] **Casella, P., Altamirano, D., Patruno, A., Wijnands, R. and van der Klis, M.** (2008). Discovery of Coherent Millisecond X-Ray Pulsations in Aquila X-1, *ApJ*, 674, L41–L44, 0708.1110.
- [30] **Thorstensen, J., Charles, P. and Bowyer, S.** (1978). The optical counterpart of Aquila X-1 /3U 1908+00/, *ApJ*, 220, L131–L134.

- [31] **Gavriil, F.P., Strohmayer, T.E., Swank, J.H. and Markwardt, C.B.** (2006). Discovery of 442 Hz Pulsations From an X-ray Source In the Globular Cluster NGC 6440, *AAS/High Energy Astrophysics Division #9*, volume 38 of *Bulletin of the American Astronomical Society*, p.336.
- [32] **Altamirano, D., Patruno, A., Heinke, C.O., Markwardt, C., Strohmayer, T.E., Linares, M., Wijnands, R., van der Klis, M. and Swank, J.H.** (2010). Discovery of a 205.89 Hz Accreting Millisecond X-ray Pulsar in the Globular Cluster NGC 6440, *ApJ*, 712, L58–L62, 0911.0435.
- [33] **Markwardt, C.B., Altamirano, D., Swank, J.H., Strohmayer, T.E., Linares, M. and Pereira, D.** (2009). RXTE Detects 245 Hz X-ray Pulsations from IGR J17511-305, *The Astronomer's Telegram*, 2197.
- [34] **Altamirano, D., Wijnands, R., van der Klis, M., Patruno, A., Watts, A., Armas Padilla, M., Cavecchi, Y., Degenaar, N., Kalamkar, M., Kaur, R., Yang, Y.J., Casella, P., Linares, M., Soleri, P. and Rea, N.** (2010). Detection of coherent millisecond pulsations at  $\sim 518$  Hz in the LMXB Swift J1749.4-2807 (GRB060602B), *The Astronomer's Telegram*, 2565.
- [35] **Bozzo, E., Belloni, T., Israel, G. and Stella, L.** (2010). SwiftJ1749-2807 now pulsing at its first overtone, *The Astronomer's Telegram*, 2567.
- [36] **Papitto, A., Bozzo, E., Ferrigno, C., Belloni, T., Burderi, L., di Salvo, T., Riggio, A., D'Ai, A. and Iaria, R.** (2011). The discovery of the 401 Hz accreting millisecond pulsar IGR J17498-2921 in a 3.8 h orbit, *A&A*, 535, L4, 1111.1976.
- [37] **Linares, M., Altamirano, D., Watts, A., Strohmayer, T., Chakrabarty, D., Patruno, A., van der Klis, M., Wijnands, R., Casella, P., Armas-Padilla, M., Cavecchi, Y., Degenaar, N., Kalamkar, M., Kaur, R., Yang, Y. and Rea, N.** (2011). RXTE detection of a thermonuclear burst from IGR J17498-2921: distance estimate and burst oscillations, *The Astronomer's Telegram*, 3568.
- [38] **Eckert, D., Del Santo, M., Bazzano, A., Watanabe, K., Paizis, A., Bozzo, E., Ferrigno, C., Caballero, I., Sidoli, L. and Kuiper, L.** (2013). IGR J18245-2452: a new hard X-ray transient discovered by INTEGRAL, *The Astronomer's Telegram*, 4925.
- [39] **Patruno, A. and Watts, A.L.** (2012). Accreting Millisecond X-Ray Pulsars, *ArXiv e-prints*, 1206.2727.
- [40] **HEASARC**, <http://heasarc.gsfc.nasa.gov>, date: 10.08.2016.
- [41] **mission operation center, S.**, <https://www.swift.psu.edu/>, date: 10.08.2016.
- [42] **Chen, W., Shrader, C.R. and Livio, M.** (1997). The Properties of X-Ray and Optical Light Curves of X-Ray Novae, *ApJ*, 491, 312, arXiv: astro-ph/9707138.

- [43] **Lasota, J.P.** (2001). The disc instability model of dwarf novae and low-mass X-ray binary transients, *New Astronomy Reviews*, 45, 449–508, arXiv:astro-ph/0102072.
- [44] **King, A.R. and Ritter, H.** (1998). The light curves of soft X-ray transients, *MNRAS*, 293, L42–L48.
- [45] **Wachter, S., Hoard, D.W., Bailyn, C.D., Corbel, S. and Kaaret, P.** (2002). A Closer Look at the Soft X-Ray Transient X1608-52: Long-Term Optical and X-Ray Observations, *ApJ*, 568, 901–911, arXiv:astro-ph/0112465.
- [46] **Remillard, R.A. and McClintock, J.E.** (2006). X-Ray Properties of Black-Hole Binaries, *ARA&A*, 44, 49–92, arXiv:astro-ph/0606352.
- [47] **Shakura, N.I. and Sunyaev, R.A.** (1973). Black holes in binary systems. Observational appearance., *A&A*, 24, 337–355.
- [48] **Ichimaru, S.** (1977). Bimodal behavior of accretion disks - Theory and application to Cygnus X-1 transitions, *ApJ*, 214, 840–855.
- [49] **Narayan, R. and Yi, I.** (1994). Advection-dominated accretion: A self-similar solution, *ApJ*, 428, L13–L16, arXiv:astro-ph/9403052.
- [50] **Illarionov, A.F. and Sunyaev, R.A.** (1975). Why the Number of Galactic X-ray Stars Is so Small?, *A&A*, 39, 185.
- [51] **Davies, R.E., Fabian, A.C. and Pringle, J.E.** (1979). Spindown of neutron stars in close binary systems, *MNRAS*, 186, 779–782.
- [52] **Davies, R.E. and Pringle, J.E.** (1981). Spindown of neutron stars in close binary systems. II, *MNRAS*, 196, 209–224.
- [53] **Wang, Y.M. and Robertson, J.A.** (1985). 'Propeller' action by rotating neutron stars, *A&A*, 151, 361–371.
- [54] **Campana, S., Colpi, M., Mereghetti, S., Stella, L. and Tavani, M.** (1998). The neutron stars of Soft X-ray Transients, *A&ARv*, 8, 279–316, arXiv:astro-ph/9805079.
- [55] **Verbunt, F., Belloni, T., Johnston, H.M., van der Klis, M. and Lewin, W.H.G.** (1994). ROSAT observations of soft X-ray transients in quiescence, *A&A*, 285, 903–911.
- [56] **van Paradijs, J.** (1996). On the Accretion Instability in Soft X-Ray Transients, *ApJ*, 464, L139.
- [57] **van der Klis, M.** (1994). Similarities in neutron star and black hole accretion, *ApJS*, 92, 511–519.
- [58] **Hasinger, G. and van der Klis, M.** (1989). Two patterns of correlated X-ray timing and spectral behaviour in low-mass X-ray binaries, *A&A*, 225, 79–96.



- [59] Campana, S., Stella, L., Mereghetti, S., Colpi, M., Tavani, M., Ricci, D., Fiume, D.D. and Belloni, T. (1998). Aquila X-1 from Outburst to Quiescence: The Onset of the Propeller Effect and Signs of a Turned-on Rotation-powered Pulsar, *ApJ*, 499, L65, arXiv:astro-ph/9803303.
- [60] Zhang, S.N., Yu, W. and Zhang, W. (1998). Spectral Transitions in Aquila X-1: Evidence for “Propeller” Effects, *ApJ*, 494, L71, arXiv:astro-ph/9711282.
- [61] Asai, K., Matsuoka, M., Mihara, T., Sugizaki, M., Serino, M., Nakahira, S., Negoro, H., Ueda, Y. and Yamaoka, K. (2013). A Propeller-effect Interpretation of MAXI/GSC Light Curves of 4U 1608-52 and Aql X-1 and Application to XTE J1701-462, *ApJ*, 773, 117, 1306.3545.
- [62] Maitra, D. and Bailyn, C.D. (2008). Outburst Morphology in the Soft X-Ray Transient Aquila X-1, *ApJ*, 688, 537–549, 0807.3542.
- [63] Campana, S., Coti Zelati, F. and D’Avanzo, P. (2013). Mining the Aql X-1 long-term X-ray light curve, *MNRAS*, 432, 1695–1700, 1304.4033.
- [64] Levine, A.M., Bradt, H., Cui, W., Jernigan, J.G., Morgan, E.H., Remillard, R., Shirey, R.E. and Smith, D.A. (1996). First Results from the All-Sky Monitor on the Rossi X-Ray Timing Explorer, *ApJ*, 469, L33, arXiv:astro-ph/9608109.
- [65] Jahoda, K., Swank, J.H., Giles, A.B., Stark, M.J., Strohmayer, T., Zhang, W. and Morgan, E.H. (1996). In-orbit performance and calibration of the Rossi X-ray Timing Explorer (RXTE) Proportional Counter Array (PCA), *O.H. Siegmund and M.A. Gummin, editors, Society of Photo-Optical Instrumentation Engineers (SPIE) Conference Series*, volume 2808 of *Society of Photo-Optical Instrumentation Engineers (SPIE) Conference Series*, pp.59–70.
- [66] Matsuoka, M., Kawasaki, K., Ueno, S., Tomida, H., Kohama, M., Suzuki, M., Adachi, Y., Ishikawa, M., Mihara, T., Sugizaki, M., Isobe, N. and Nakagawa, Y. (2009). The MAXI Mission on the ISS: Science and Instruments for Monitoring All-Sky X-Ray Images, *PASJ*, 61, 999–, 0906.0631.
- [67] Guver, T., Ak, T., Gungor, C. and Eksi, Y. (2013). Optical observations of Aql X-1, *The Astronomer’s Telegram*, 5129, 1.
- [68] Maccarone, T.J. and Coppi, P.S. (2003). Spectral fits to the 1999 Aql X-1 outburst data, *A&A*, 399, 1151–1157, arXiv:astro-ph/0301091.
- [69] Coppi, P.S. (2000). EQPAIR: A Hybrid Thermal/Non-Thermal Model for the Spectra of X-Ray Binaries, *AAS/High Energy Astrophysics Division #5*, volume 32 of *Bulletin of the American Astronomical Society*, p.1217.
- [70] Raichur, H., Misra, R. and Dewangan, G. (2011). Broad-band spectral analysis of Aql X-1, *MNRAS*, 416, 637–643, 1105.5523.

- [71] **Maitra, D. and Bailyn, C.D.** (2004). Evolution of Spectral States of Aquila X-1 during the 2000 Outburst, *ApJ*, 608, 444–453, [astro-ph/0401212](#).
- [72] **Caballero-Garcia, M.D., Miller, J.M. and Fabian, A.C.** (2008). The high-energy emission from GX 339-4 as seen with INTEGRAL and XMM-Newton, *Proceedings of the 7th INTEGRAL Workshop*, 0812.1346.
- [73] **Welsh, W.F., Robinson, E.L. and Young, P.** (2000). The Orbital Light Curve of Aquila X-1, *AJ*, 120, 943–949, [arXiv:astro-ph/0004344](#).
- [74] **Gilfanov, M., Revnivtsev, M., Sunyaev, R. and Churazov, E.** (1998). The millisecond X-ray pulsar/burster SAX J1808.4-3658: the outburst light curve and the power law spectrum, *A&A*, 338, L83–L86, [arXiv:astro-ph/9805152](#).
- [75] **Psaltis, D. and Chakrabarty, D.** (1999). The Disk-Magnetosphere Interaction in the Accretion-powered Millisecond Pulsar SAX J1808.4-3658, *ApJ*, 521, 332–340, [arXiv:astro-ph/9809335](#).
- [76] **Rappaport, S.A., Fregeau, J.M. and Spruit, H.** (2004). Accretion onto Fast X-Ray Pulsars, *ApJ*, 606, 436–443, [arXiv:astro-ph/0310224](#).
- [77] **Ibragimov, A. and Poutanen, J.** (2009). Accreting millisecond pulsar SAX J1808.4-3658 during its 2002 outburst: evidence for a receding disc, *MNRAS*, 400, 492–508, [0901.0073](#).
- [78] **Ekşi, K.Y. and Kutlu, E.** (2011). Accretion in the spin-down regime, *E. Göğüş, T. Belloni and Ü. Ertan, editors, American Institute of Physics Conference Series*, volume 1379 of *American Institute of Physics Conference Series*, pp.156–159.
- [79] **Menou, K., Esin, A.A., Narayan, R., Garcia, M.R., Lasota, J.P. and McClintock, J.E.** (1999). Black Hole and Neutron Star Transients in Quiescence, *ApJ*, 520, 276–291, [arXiv:astro-ph/9810323](#).
- [80] **Ustyugova, G.V., Koldoba, A.V., Romanova, M.M. and Lovelace, R.V.E.** (2006). “Propeller” Regime of Disk Accretion to Rapidly Rotating Stars, *ApJ*, 646, 304–318, [arXiv:astro-ph/0603249](#).
- [81] **Romanova, M.M., Ustyugova, G.V., Koldoba, A.V. and Lovelace, R.V.E.** (2004). The Propeller Regime of Disk Accretion to a Rapidly Rotating Magnetized Star, *ApJ*, 616, L151–L154, [arXiv:astro-ph/0502266](#).
- [82] **Galloway, D.K., Muno, M.P., Hartman, J.M., Psaltis, D. and Chakrabarty, D.** (2008). Thermonuclear (Type I) X-Ray Bursts Observed by the Rossi X-Ray Timing Explorer, *ApJS*, 179, 360–422, [arXiv:astro-ph/0608259](#).
- [83] **Matsuoka, M. and Asai, K.** (2013). Simplified Picture of Low-Mass X-Ray Binaries Based on Data from Aquila X-1 and 4U 1608-52, *PASJ*, 65, 26, [1210.2586](#).

- [84] **Tudose, V., Fender, R.P., Linares, M., Maitra, D. and van der Klis, M.** (2009). The disc-jet coupling in the neutron star X-ray binary Aquila X-1, *MNRAS*, *400*, 2111–2121, 0908.3604.
- [85] **Romanova, M.M., Ustyugova, G.V., Koldoba, A.V. and Lovelace, R.V.E.** (2009). Launching of conical winds and axial jets from the disc-magnetosphere boundary: axisymmetric and 3D simulations, *MNRAS*, *399*, 1802–1828.
- [86] **Lii, P., Romanova, M. and Lovelace, R.** (2012). Magnetic launching and collimation of jets from the disc-magnetosphere boundary: 2.5D MHD simulations, *MNRAS*, *420*, 2020–2033, 1104.4374.
- [87] **Lovelace, R.V.E., Romanova, M.M. and Bisnovatyi-Kogan, G.S.** (1999). Magnetic Propeller Outflows, *ApJ*, *514*, 368–372, arXiv:astro-ph/9811369.
- [88] **Jonker, P.G., Gallo, E., Dhawan, V., Rupen, M., Fender, R.P. and Dubus, G.** (2004). Radio and X-ray observations during the outburst decay of the black hole candidate XTE J1908+094, *MNRAS*, *351*, 1359–1364, arXiv:astro-ph/0403578.
- [89] **Maccarone, T.J. and Coppi, P.S.** (2003). Hysteresis in the light curves of soft X-ray transients, *MNRAS*, *338*, 189–196, arXiv:astro-ph/0209116.
- [90] **Davidson, K. and Ostriker, J.P.** (1973). Neutron-Star Accretion in a Stellar Wind: Model for a Pulsed X-Ray Source, *ApJ*, *179*, 585–598.
- [91] **Yu, W. and Dolence, J.** (2007). A Hard-to-Soft State Transition during a Luminosity Decline of Aquila X-1, *ApJ*, *667*, 1043–1047, arXiv:astro-ph/0608601.
- [92] **Powell, C.R., Haswell, C.A. and Falanga, M.** (2007). Mass transfer during low-mass X-ray transient decays, *MNRAS*, *374*, 466–476, arXiv:astro-ph/0610108.
- [93] **Pringle, J.E. and Rees, M.J.** (1972). Accretion Disc Models for Compact X-Ray Sources, *A&A*, *21*, 1.
- [94] **Ghosh, P. and Lamb, F.K.** (1979). Accretion by rotating magnetic neutron stars. II - Radial and vertical structure of the transition zone in disk accretion, *ApJ*, *232*, 259–276.
- [95] **Ghosh, P. and Lamb, F.K.** (1979). Accretion by rotating magnetic neutron stars. III - Accretion torques and period changes in pulsating X-ray sources, *ApJ*, *234*, 296–316.
- [96] **Lamb, F.K., Pethick, C.J. and Pines, D.** (1973). A Model for Compact X-Ray Sources: Accretion by Rotating Magnetic Stars, *ApJ*, *184*, 271–290.
- [97] **Romanova, M.M. and Owocki, S.P.** (2015). Accretion, Outflows, and Winds of Magnetized Stars, *Space Science Reviews*, *191*, 339–389, 1605.04979.

- [98] **Lipunov, V.M., Börner, G. and Wadhwa, R.S.** (1992). *Astrophysics of Neutron Stars*.
- [99] **Campana, S., Gastaldello, F., Stella, L., Israel, G.L., Colpi, M., Pizzolato, F., Orlandini, M. and Dal Fiume, D.** (2001). The Transient X-Ray Pulsar 4U 0115+63 from Quiescence to Outburst through the Centrifugal Transition, *ApJ*, 561, 924–929, astro-ph/0107236.
- [100] **Cui, W.** (1997). Evidence for “Propeller” Effects in X-Ray Pulsars GX 1+4 and GRO J1744-28, *ApJ*, 482, L163–L166, astro-ph/9704084.
- [101] **Elsner, R.F. and Lamb, F.K.** (1977). Accretion by magnetic neutron stars. I - Magnetospheric structure and stability, *ApJ*, 215, 897–913.
- [102] **Lipunov, V.M. and Shakura, N.I.** (1976). On the nature of binary-system X-ray pulsars, *Soviet Astronomy Letters*, 2, 133–135.
- [103] **Balucinska-Church, M. and McCammon, D.** (1992). Photoelectric absorption cross sections with variable abundances, *ApJ*, 400, 699.
- [104] **Sakurai, S., Yamada, S., Torii, S., Noda, H., Nakazawa, K., Makishima, K. and Takahashi, H.** (2012). Accretion Geometry of the Low-Mass X-Ray Binary Aquila X-1 in the Soft and Hard States, *PASJ*, 64, 72, 1201.5891.
- [105] **Zhang, S.N., Yu, W. and Zhang, W.** (1998). Spectral State Transitions in Aquila X-1: Evidence for “Propeller” Effects, *ApJ*, 494, L71–L74, astro-ph/9711282.
- [106] **Titarchuk, L. and Lyubarskij, Y.** (1995). Power-Law Spectra as a Result of Comptonization of the Soft Radiation in a Plasma Cloud, *ApJ*, 450, 876.
- [107] **Lyubarskij, Y.E. and Shakura, N.I.** (1987). Nonlinear self-similar problems of nonstationary disk accretion, *Soviet Astronomy Letters*, 13, 386.
- [108] **Lipunova, G.V. and Shakura, N.I.** (2002). Non-Steady-State Accretion Disks in X-Ray Novae: Outburst Models for Nova Monocerotis 1975 and Nova Muscae 1991, *Astronomy Reports*, 46, 366–379, 0905.2515.
- [109] **Suleimanov, V.F., Lipunova, G.V. and Shakura, N.I.** (2008). Modeling of non-stationary accretion disks in X-ray novae A 0620-00 and GRS 1124-68 during outburst, *A&A*, 491, 267–277, 0805.1001.
- [110] **Cannizzo, J.K., Lee, H.M. and Goodman, J.** (1990). The disk accretion of a tidally disrupted star onto a massive black hole, *ApJ*, 351, 38–46.
- [111] **Campana, S., Brivio, F., Degenaar, N., Mereghetti, S., Wijnands, R., D’Avanzo, P., Israel, G.L. and Stella, L.** (2014). The return to quiescence of Aql X-1 following the 2010 outburst, *MNRAS*, 441, 1984–1991, 1404.2065.
- [112] **Güngör, C., Güver, T. and Eksi, K.Y.** (2014). Classification and spectral evolution of outbursts of Aql X-1, *MNRAS*, 439, 2717–2727, 1401.4054.

## APPENDICES

**APPENDIX A:** Best fit parameters of *EQPAIR* + *Gauss* model of RXTE/PCA data during 2000, 2010 and 2011 outbursts of Aql X-1

**APPENDIX B:** Best fit parameters of *black body* + *disk black body* + *Gauss* model of RXTE/PCA data during 2000 and 2011 outbursts of Aql X-1

**APPENDIX C:** Best fit parameters of *black body radiation* + *comptonisation* + *disk black body* + *Gauss* model of RXTE/PCA data during 2000 and 2011 outbursts of Aql X-1



**APPENDIX A:** Best fit parameters of *EQPAIR* + *Gauss* model of RXTE/PCA data during 2000, 2010 and 2011 outbursts of Aql X-1

**Table A.1 :** Best fit parameters of *EQPAIR* model and the Gaussian line for the 2000 outburst.

JD-51000 (days)	$h_1/s$	$kT_{bb}$ (eV)	$\tau_p$	$\chi^2/d.o.f.$	Line Energy (keV)	Line Width (keV)	Flux $^a_{eqpair}$	Flux $^b_{gauss}$
811.2856	4.80 $^{+1.27}_{-1.15}$	658 $^{+292}_{-61}$	0.55 $^{+0.18}_{-0.12}$	0.65	5.80 $^{+0.33}_{-0.80}$	1.71 $^c$	0.235 $^{+0.004}_{-0.004}$	0.136 $^{+0.008}_{-0.008}$
812.3495	3.08 $^{+0.32}_{-0.24}$	719 $^{+62}_{-80}$	0.99 $^{+0.16}_{-0.22}$	0.68	6.34 $^{+0.19}_{-0.21}$	0.57 $^{+0.33}_{-0.29}$	0.497 $^{+0.004}_{-0.004}$	0.061 $^{+0.008}_{-0.008}$
813.2773	3.58 $^{+0.33}_{-0.49}$	714 $^{+101}_{-55}$	0.92 $^{+0.17}_{-0.14}$	0.82	5.80 $^{+0.24}_{-0.80}$	1.40 $^{+0.18}_{-0.27}$	0.745 $^{+0.004}_{-0.004}$	0.245 $^{+0.013}_{-0.015}$
816.4667	3.27 $^{+0.39}_{-0.21}$	684 $^{+220}_{-192}$	2.17 $^{+0.37}_{-0.44}$	0.68	6.07 $^{+0.17}_{-0.19}$	1.20 $^{+0.20}_{-0.18}$	2.787 $^{+0.008}_{-0.007}$	0.670 $^{+0.038}_{-0.037}$
817.7979	2.72 $^{+0.22}_{-0.25}$	624 $^{+161}_{-209}$	4.21 $^{+0.74}_{-0.63}$	0.67	6.04 $^{+0.17}_{-0.19}$	1.20 $^{+0.19}_{-0.17}$	4.055 $^{+0.011}_{-0.011}$	0.973 $^{+0.055}_{-0.054}$
818.7868	1.89 $^{+0.09}_{-0.06}$	856 $^{+39}_{-47}$	3.93 $^{+0.90}_{-0.28}$	0.54	6.52 $^{+0.15}_{-0.16}$	0.85 $^{+0.20}_{-0.18}$	5.260 $^{+0.011}_{-0.012}$	0.804 $^{+0.061}_{-0.059}$
820.5169	1.69 $^{+0.07}_{-0.17}$	795 $^{+110}_{-41}$	5.68 $^{+0.23}_{-0.26}$	0.54	6.38 $^{+0.14}_{-0.15}$	1.13 $^{+0.17}_{-0.24}$	7.273 $^{+0.009}_{-0.026}$	1.663 $^{+0.091}_{-0.089}$
822.7745	0.48 $^{+0.07}_{-0.08}$	715 $^{+84}_{-70}$	8.92 $^{+0.46}_{-0.70}$	0.56	6.29 $^{+0.14}_{-0.30}$	1.34 $^{+0.24}_{-0.21}$	10.334 $^{+0.026}_{-0.026}$	3.457 $^{+0.218}_{-0.211}$
823.7689	0.45 $^{+0.03}_{-0.07}$	820 $^{+75}_{-295}$	9.36 $^{+2.49}_{-0.63}$	0.69	6.72 $^{+0.20}_{-0.25}$	0.82 $^{+0.30}_{-0.33}$	12.544 $^{+0.032}_{-0.033}$	1.865 $^{+0.203}_{-0.193}$
824.7611	0.75 $^{+0.23}_{-0.13}$	592 $^{+104}_{-260}$	11.57 $^{+0.49}_{-0.40}$	0.32	6.26 $^{+0.22}_{-0.26}$	0.91 $^{+0.26}_{-0.23}$	11.919 $^{+0.038}_{-0.035}$	2.287 $^{+0.223}_{-0.213}$
825.7550	0.69 $^{+0.11}_{-0.11}$	547 $^{+221}_{-70}$	10.76 $^{+0.26}_{-0.62}$	0.64	5.81 $^{+0.21}_{-0.81}$	1.42 $^{+0.08}_{-0.17}$	10.000 $^{+0.029}_{-0.015}$	5.418 $^{+0.175}_{-0.235}$
826.5129	0.65 $^{+0.18}_{-0.13}$	653 $^{+107}_{-125}$	11.32 $^{+0.39}_{-0.26}$	0.39	6.25 $^{+0.18}_{-0.21}$	1.15 $^{+0.18}_{-0.17}$	12.902 $^{+0.034}_{-0.034}$	4.296 $^{+0.260}_{-0.184}$
828.5344	0.45 $^{+0.05}_{-0.05}$	755 $^{+13}_{-88}$	8.98 $^{+0.22}_{-0.59}$	0.68	6.61 $^{+0.18}_{-0.22}$	0.93 $^{+0.22}_{-0.20}$	10.958 $^{+0.030}_{-0.029}$	2.171 $^{+0.175}_{-0.175}$
831.2024	0.69 $^{+0.14}_{-0.14}$	615 $^{+88}_{-58}$	11.37 $^{+0.32}_{-0.64}$	0.53	5.96 $^{+0.20}_{-0.17}$	1.38 $^{+0.17}_{-0.19}$	11.061 $^{+0.028}_{-0.033}$	5.274 $^{+0.250}_{-0.207}$
833.4586	0.50 $^{+0.13}_{-0.08}$	697 $^{+58}_{-105}$	9.67 $^{+0.17}_{-0.89}$	0.74	6.52 $^{+0.20}_{-0.20}$	0.97 $^{+0.19}_{-0.17}$	11.268 $^{+0.033}_{-0.031}$	2.984 $^{+0.207}_{-0.198}$
834.3003	0.87 $^{+0.14}_{-0.24}$	523 $^{+160}_{-112}$	12.21 $^{+0.24}_{-0.25}$	0.35	5.92 $^{+0.19}_{-0.92}$	1.33 $^{+0.15}_{-0.36}$	13.604 $^{+0.036}_{-0.289}$	5.772 $^{+0.295}_{-0.289}$
835.1903	0.73 $^{+0.08}_{-0.19}$	529 $^{+154}_{-129}$	11.26 $^{+0.27}_{-0.19}$	0.43	5.88 $^{+0.18}_{-0.88}$	1.29 $^{+0.12}_{-0.15}$	7.705 $^{+0.022}_{-0.023}$	3.812 $^{+0.176}_{-0.172}$
835.4761	0.63 $^{+0.10}_{-0.17}$	651 $^{+145}_{-73}$	11.24 $^{+0.78}_{-1.01}$	0.34	6.06 $^{+0.19}_{-0.22}$	1.37 $^{+0.15}_{-0.15}$	12.771 $^{+0.034}_{-0.035}$	5.920 $^{+0.280}_{-0.274}$
836.5150	0.70 $^{+0.03}_{-0.21}$	596 $^{+203}_{-100}$	11.34 $^{+0.28}_{-0.37}$	0.52	5.88 $^{+0.19}_{-0.88}$	1.48 $^{+0.12}_{-0.15}$	12.683 $^{+0.035}_{-0.036}$	7.430 $^{+0.295}_{-0.290}$
836.5906	0.56 $^{+0.07}_{-0.21}$	734 $^{+245}_{-133}$	10.81 $^{+0.44}_{-0.64}$	0.64	6.47 $^{+0.22}_{-0.22}$	1.03 $^{+0.22}_{-0.19}$	13.376 $^{+0.036}_{-0.036}$	3.463 $^{+0.234}_{-0.244}$
836.6590	0.61 $^{+0.15}_{-0.15}$	647 $^{+133}_{-153}$	11.11 $^{+0.96}_{-1.03}$	0.42	6.05 $^{+0.21}_{-0.22}$	1.25 $^{+0.20}_{-0.18}$	11.543 $^{+0.034}_{-0.033}$	4.655 $^{+0.261}_{-0.255}$
837.3107	0.73 $^{+0.18}_{-0.15}$	605 $^{+111}_{-161}$	11.83 $^{+0.29}_{-0.42}$	0.62	5.95 $^{+0.23}_{-0.95}$	1.46 $^{+0.17}_{-0.18}$	12.892 $^{+0.035}_{-0.034}$	5.877 $^{+0.291}_{-0.285}$
838.5825	0.61 $^{+0.13}_{-0.15}$	622 $^{+135}_{-143}$	10.79 $^{+0.69}_{-0.77}$	0.78	6.11 $^{+0.18}_{-0.21}$	1.19 $^{+0.18}_{-0.21}$	10.843 $^{+0.031}_{-0.031}$	4.419 $^{+0.238}_{-0.231}$
839.1655	0.60 $^{+0.20}_{-0.12}$	680 $^{+113}_{-143}$	11.01 $^{+1.05}_{-1.05}$	0.44	6.34 $^{+0.18}_{-0.21}$	1.05 $^{+0.20}_{-0.18}$	12.792 $^{+0.034}_{-0.033}$	3.672 $^{+0.251}_{-0.242}$
841.4233	0.53 $^{+0.08}_{-0.08}$	661 $^{+197}_{-197}$	9.31 $^{+0.87}_{-0.87}$	0.65	6.48 $^{+0.22}_{-0.22}$	0.97 $^{+0.22}_{-0.19}$	9.220 $^{+0.027}_{-0.026}$	2.244 $^{+0.169}_{-0.162}$
843.4235	0.70 $^{+0.20}_{-0.19}$	597 $^{+154}_{-90}$	11.24 $^{+0.66}_{-0.08}$	0.50	5.93 $^{+0.21}_{-0.93}$	1.45 $^{+0.15}_{-0.17}$	11.201 $^{+0.030}_{-0.034}$	5.737 $^{+0.258}_{-0.259}$
844.1205	0.62 $^{+0.10}_{-0.12}$	646 $^{+145}_{-124}$	10.85 $^{+0.17}_{-0.34}$	0.44	6.13 $^{+0.19}_{-0.22}$	1.32 $^{+0.15}_{-0.16}$	10.645 $^{+0.031}_{-0.027}$	4.558 $^{+0.239}_{-0.223}$
845.1457	0.87 $^{+0.30}_{-0.12}$	516 $^{+162}_{-161}$	12.12 $^{+0.42}_{-0.51}$	0.25	6.06 $^{+0.24}_{-0.19}$	1.12 $^{+0.23}_{-0.22}$	10.955 $^{+0.033}_{-0.029}$	2.916 $^{+0.227}_{-0.219}$
846.2087	0.63 $^{+0.15}_{-0.15}$	606 $^{+134}_{-63}$	10.75 $^{+0.33}_{-0.99}$	0.45	6.08 $^{+0.19}_{-0.22}$	1.28 $^{+0.17}_{-0.16}$	9.423 $^{+0.027}_{-0.030}$	4.203 $^{+0.208}_{-0.203}$
849.3941	0.63 $^{+0.14}_{-0.19}$	573 $^{+177}_{-109}$	10.51 $^{+0.40}_{-0.70}$	0.48	5.82 $^{+0.25}_{-0.82}$	1.45 $^{+0.11}_{-0.025}$	8.108 $^{+0.013}_{-0.197}$	4.153 $^{+0.163}_{-0.197}$
849.4632	0.42 $^{+0.23}_{-0.03}$	810 $^{+38}_{-44}$	8.61 $^{+1.47}_{-0.49}$	0.77	6.71 $^{+0.21}_{-0.26}$	0.90 $^{+0.29}_{-0.24}$	9.447 $^{+0.029}_{-0.021}$	1.542 $^{+0.160}_{-0.151}$
849.5347	0.45 $^{+0.07}_{-0.04}$	774 $^{+95}_{-88}$	8.89 $^{+0.56}_{-0.55}$	0.83	6.60 $^{+0.26}_{-0.26}$	1.03 $^{+0.25}_{-0.21}$	9.398 $^{+0.023}_{-0.025}$	2.068 $^{+0.172}_{-0.164}$
850.1023	0.61 $^{+0.19}_{-0.11}$	646 $^{+95}_{-101}$	10.89 $^{+0.70}_{-0.70}$	0.41	6.20 $^{+0.19}_{-0.22}$	1.21 $^{+0.18}_{-0.16}$	9.067 $^{+0.025}_{-0.025}$	3.374 $^{+0.190}_{-0.185}$
850.8640	0.74 $^{+0.19}_{-0.16}$	544 $^{+165}_{-151}$	11.51 $^{+0.33}_{-0.26}$	0.72	5.81 $^{+0.24}_{-0.81}$	1.44 $^{+0.18}_{-0.18}$	8.355 $^{+0.023}_{-0.023}$	3.772 $^{+0.190}_{-0.190}$
851.2877	0.64 $^{+0.24}_{-0.17}$	617 $^{+151}_{-151}$	10.93 $^{+0.66}_{-0.66}$	0.60	6.09 $^{+0.21}_{-0.21}$	1.32 $^{+0.19}_{-0.21}$	8.692 $^{+0.025}_{-0.025}$	3.440 $^{+0.188}_{-0.183}$
852.5877	0.63 $^{+0.09}_{-0.16}$	592 $^{+150}_{-70}$	10.96 $^{+0.70}_{-0.47}$	1.10	6.01 $^{+0.23}_{-0.61}$	1.30 $^{+0.21}_{-0.26}$	7.669 $^{+0.023}_{-0.023}$	3.059 $^{+0.176}_{-0.172}$
852.6531	0.53 $^{+0.09}_{-0.13}$	694 $^{+77}_{-191}$	10.44 $^{+0.70}_{-1.00}$	0.72	6.47 $^{+0.22}_{-0.27}$	1.02 $^{+0.26}_{-0.24}$	8.104 $^{+0.024}_{-0.024}$	2.077 $^{+0.167}_{-0.159}$
853.5833	0.63 $^{+0.13}_{-0.13}$	596 $^{+115}_{-91}$	10.74 $^{+0.44}_{-0.68}$	0.54	6.11 $^{+0.22}_{-0.26}$	1.18 $^{+0.22}_{-0.20}$	7.288 $^{+0.022}_{-0.022}$	2.510 $^{+0.161}_{-0.156}$
854.2723	0.55 $^{+0.09}_{-0.10}$	621 $^{+101}_{-91}$	9.09 $^{+0.58}_{-0.81}$	0.43	6.22 $^{+0.24}_{-0.31}$	1.28 $^{+0.19}_{-0.21}$	6.314 $^{+0.019}_{-0.017}$	1.904 $^{+0.132}_{-0.126}$
855.3036	0.69 $^{+0.08}_{-0.07}$	454 $^{+95}_{-95}$	9.27 $^{+0.22}_{-0.22}$	0.51	6.61 $^{+0.29}_{-0.42}$	0.68 $^{+0.42}_{-0.42}$	4.639 $^{+0.012}_{-0.011}$	0.400 $^{+0.073}_{-0.066}$
856.1874	0.56 $^{+0.07}_{-0.07}$	647 $^{+93}_{-73}$	9.50 $^{+0.07}_{-0.26}$	0.49	6.48 $^{+0.25}_{-0.28}$	1.08 $^{+0.26}_{-0.22}$	6.289 $^{+0.018}_{-0.017}$	1.441 $^{+0.118}_{-0.112}$
856.9696	0.60 $^{+0.17}_{-0.14}$	577 $^{+15}_{-134}$	9.47 $^{+0.18}_{-0.14}$	0.52	6.40 $^{+0.23}_{-0.23}$	1.05 $^{+0.26}_{-0.16}$	5.350 $^{+0.016}_{-0.016}$	1.114 $^{+0.100}_{-0.095}$
859.2409	0.70 $^{+0.15}_{-0.16}$	492 $^{+82}_{-119}$	10.03 $^{+0.17}_{-0.22}$	0.62	6.26 $^{+0.23}_{-0.29}$	1.14 $^{+0.24}_{-0.21}$	4.122 $^{+0.013}_{-0.012}$	1.084 $^{+0.083}_{-0.079}$
860.2152	0.68 $^{+0.08}_{-0.11}$	527 $^{+94}_{-62}$	10.95 $^{+0.30}_{-0.44}$	0.51	5.80 $^{+0.32}_{-0.80}$	1.41 $^{+0.15}_{-0.27}$	3.989 $^{+0.012}_{-0.012}$	1.319 $^{+0.071}_{-0.087}$
860.5474	2.71 $^c$	1 $^{+464}_{-1}$	9.92 $^{+0.37}_{-0.28}$	0.73	6.46 $^{+0.31}_{-0.41}$	1.10 $^{+0.37}_{-0.29}$	2.948 $^{+0.015}_{-0.019}$	0.494 $^{+0.108}_{-0.096}$
861.1194	0.57 $^{+0.03}_{-0.06}$	600 $^{+28}_{-171}$	9.06 $^{+0.18}_{-0.35}$	0.67	6.39 $^{+0.36}_{-0.45}$	1.39 $^{+0.13}_{-0.29}$	3.139 $^{+0.065}_{-0.008}$	0.844 $^{+0.065}_{-0.062}$
861.8861	1.15 $^{+0.07}_{-0.04}$	190 $^{+140}_{-26}$	10.24 $^{+0.29}_{-0.25}$	0.72	6.20 $^c$	1.49 $^{+0.17}_{-0.17}$	2.192 $^{+0.007}_{-0.008}$	0.570 $^{+0.048}_{-0.045}$
862.0931	1.14 $^{+0.03}_{-0.05}$	164 $^{+14}_{-39}$	9.19 $^{+0.40}_{-0.42}$	0.82	5.95 $^{+0.45}_{-0.73}$	1.73 $^{+0.47}_{-0.34}$	2.022 $^{+0.010}_{-0.005}$	0.860 $^{+0.050}_{-0.048}$
863.2400	0.98 $^{+0.01}_{-0.02}$	236 $^{+83}_{-14}$	7.91 $^{+0.08}_{-0.25}$	0.67	5.88 $^{+0.24}_{-0.88}$	1.69 $^{+0.17}_{-0.17}$	1.509 $^{+0.004}_{-0.005}$	1.036 $^{+0.036}_{-0.035}$
864.2082	0.89 $^{+0.26}_{-0.04}$	303 $^{+165}_{-34}$	9.18 $^{+0.70}_{-0.37}$	0.55	5.84 $^{+0.44}_{-0.84}$	1.74 $^{+0.35}_{-0.35}$	1.356 $^{+0.006}_{-0.006}$	0.793 $^{+0.037}_{-0.040}$
864.2775	0.90 $^{+0.04}_{-0.03}$	270 $^{+134}_{-194}$	8.30 $^{+0.33}_{-0.33}$	0.64	5.99 $^{+0.37}_{-0.99}$	1.64 $^{+0.31}_{-0.31}$	1.308 $^{+0.006}_{-0.007}$	0.841 $^{+0.041}_{-0.040}$
865.2722	0.79 $^{+0.10}_{-0.09}$	320 $^{+42}_{-63}$	0.43 $^{+0.11}_{-0.09}$	0.95	5.88 $^{+0.21}_{-0.88}$	1.13 $^{+0.23}_{-0.24}$	0.965 $^{+0.005}_{-0.006}$	0.373 $^{+0.025}_{-0.024}$
866.9225	2.03 $^{+0.20}_{-0.15}$	760 $^{+107}_{-261}$	1.24 $^{+0.47}_{-0.22}$	1.02	6.08 $^{+0.28}_{-0.29}$	0.25 $^{+0.46}_{-0.00}$	0.627 $^{+0.013}_{-0.012}$	0.049 $^{+0.022}_{-0.019}$
866.9779	2.45 $^{+0.16}_{-0.16}$	827 $^{+42}_{-40}$	1.05 $^{+0.11}_{-0.07}$	2.21	5.60 $^c$	0.93 $^c$	0.625 $^{+0.006}_{-0.007}$	0.065 $^c$
868.2361	4.89 $^{+0.88}_{-0.96}$	1049 $^{+16}_{-107}$	0.89 $^{+0.04}_{-0.04}$	0.72	5.87 $^c$	0.25 $^c$	0.371 $^{+0.002}_{-0.007}$	0.000 $^{+0.011}_{-0.007}$
869.4744	4.68 $^{+1.81}_{-0.95}$	714 $^{+191}_{-58}$	0.66 $^{+0.18}_{-0.14}$	0.62	6.50 $^{+0.27}_{-0.33}$	0.82 $^{+0.48}_{-0.34}$	0.143 $^{+0.003}_{-0.003}$	0.034 $^{+0.005}_{-0.005}$
870.3233	7.51 $^{+3.92}_{-2.80}$	1071 $^{+119}_{-205}$	1.11 $^{+0.16}_{-0.16}$	1.50	5.60 $^c$	1.75 $^c$	0.078 $^{+0.004}_{-0.004}$	0.100 $^c$
871.2461	12.86 $^{+13.06}_{-7.65}$	724 $^{+600}_{-246}$	0.00 $^{+1$					

**Table A.2** : Same as Table A.1 but for the 2010 outburst.

JD-55000 (days)	$l_h/l_s$	$kT_{bb}$ (eV)	$\tau_p$	$\chi^2/\text{d.o.f.}$	Line Energy (keV)	Line Width (keV)	Flux $^a_{eqpair}$	Flux $^b_{gauss}$
426.2689	2.71 $^{+0.07}_{-0.06}$	784 $^{+53}_{-50}$	1.36 $^{+0.12}_{-0.11}$	2.12	5.60 $^{+0.11}_{-0.10}$	1.01 $^{+0.22}_{-0.21}$	1.048 $^{+0.006}_{-0.007}$	0.127 $^{+0.025}_{-0.024}$
426.9906	2.63 $^{+0.12}_{-0.09}$	740 $^{+57}_{-58}$	1.41 $^{+0.10}_{-0.10}$	1.14	5.60 $^{+0.10}_{-0.09}$	1.24 $^{+0.20}_{-0.14}$	1.275 $^{+0.009}_{-0.006}$	0.235 $^{+0.031}_{-0.031}$
428.8847	2.76 $^{+0.04}_{-0.09}$	672 $^{+47}_{-77}$	1.90 $^{+0.11}_{-0.62}$	1.92	5.60 $^{+0.09}_{-0.60}$	1.23 $^{+0.14}_{-0.14}$	1.782 $^{+0.006}_{-0.006}$	0.403 $^{+0.022}_{-0.031}$
430.8469	2.83 $^{+0.11}_{-0.07}$	795 $^{+66}_{-14}$	1.39 $^{+0.12}_{-0.10}$	2.06	5.60 $^{+0.07}_{-0.60}$	0.97 $^{+0.20}_{-0.19}$	1.313 $^{+0.004}_{-0.019}$	0.169 $^{+0.029}_{-0.029}$
433.8503	2.62 $^{+0.12}_{-0.11}$	718 $^{+50}_{-51}$	1.08 $^{+0.05}_{-0.10}$	1.59	5.60 $^{+0.13}_{-0.60}$	0.94 $^{+0.25}_{-0.25}$	0.746 $^{+0.006}_{-0.007}$	0.089 $^{+0.019}_{-0.020}$
436.3373	3.41 $^{+0.34}_{-0.28}$	755 $^{+30}_{-34}$	0.78 $^{+0.40}_{-0.04}$	0.82	6.68 $^{+0.25}_{-0.24}$	0.25 $^{+0.42}_{-0.25}$	0.264 $^{+0.004}_{-0.004}$	0.022 $^{+0.005}_{-0.005}$
441.8428	3.23 $^{+0.31}_{-0.23}$	756 $^{+51}_{-44}$	0.91 $^{+0.07}_{-0.09}$	0.68	6.02 $^{+0.27}_{-0.35}$	0.76 $^{+0.51}_{-0.45}$	0.636 $^{+0.010}_{-0.010}$	0.110 $^{+0.026}_{-0.025}$
447.5829	2.94 $^{+0.07}_{-0.07}$	582 $^{+93}_{-102}$	2.61 $^{+0.41}_{-0.11}$	0.80	5.60 $^{+0.16}_{-0.60}$	1.35 $^{+0.23}_{-0.17}$	2.405 $^{+0.006}_{-0.007}$	0.629 $^{+0.031}_{-0.032}$
449.3527	2.04 $^{+0.18}_{-0.13}$	619 $^{+84}_{-58}$	4.54 $^{+1.03}_{-0.34}$	0.83	6.21 $^{+0.17}_{-0.19}$	1.08 $^{+0.23}_{-0.20}$	3.552 $^{+0.019}_{-0.021}$	0.841 $^{+0.091}_{-0.088}$
450.0526	1.41 $^{+0.05}_{-0.05}$	742 $^{+33}_{-41}$	4.88 $^{+0.14}_{-0.35}$	1.10	5.88 $^{+0.17}_{-0.19}$	1.62 $^{+0.12}_{-0.17}$	4.197 $^{+0.021}_{-0.020}$	2.355 $^{+0.128}_{-0.126}$
451.6399	0.56 $^{+0.09}_{-0.04}$	589 $^{+37}_{-80}$	9.07 $^{+0.41}_{-0.83}$	0.50	6.54 $^{+0.23}_{-0.29}$	0.78 $^{+0.30}_{-0.28}$	5.596 $^{+0.031}_{-0.032}$	0.796 $^{+0.167}_{-0.151}$
452.6867	0.64 $^{+0.07}_{-0.06}$	570 $^{+49}_{-57}$	10.74 $^{+0.45}_{-0.45}$	0.72	5.87 $^{+0.30}_{-0.87}$	1.49 $^{+0.25}_{-0.24}$	7.229 $^{+0.036}_{-0.035}$	3.189 $^{+0.294}_{-0.283}$
453.1981	0.59 $^{+0.05}_{-0.05}$	643 $^{+44}_{-44}$	10.85 $^{+0.53}_{-0.49}$	0.58	6.38 $^{+0.28}_{-0.28}$	0.82 $^{+0.29}_{-0.25}$	7.970 $^{+0.038}_{-0.038}$	1.381 $^{+0.256}_{-0.233}$
454.3926	0.58 $^{+0.06}_{-0.05}$	588 $^{+48}_{-54}$	9.23 $^{+0.74}_{-0.61}$	0.79	6.50 $^{+0.20}_{-0.26}$	0.87 $^{+0.28}_{-0.24}$	5.844 $^{+0.026}_{-0.032}$	1.125 $^{+0.181}_{-0.166}$
455.1530	0.62 $^{+0.06}_{-0.08}$	595 $^{+39}_{-48}$	10.64 $^{+0.56}_{-0.42}$	0.73	6.27 $^{+0.20}_{-0.25}$	1.08 $^{+0.23}_{-0.20}$	6.988 $^{+0.033}_{-0.033}$	2.094 $^{+0.243}_{-0.228}$
456.2053	0.60 $^{+0.06}_{-0.05}$	606 $^{+39}_{-50}$	10.47 $^{+0.49}_{-0.51}$	0.53	6.30 $^{+0.24}_{-0.22}$	1.19 $^{+0.26}_{-0.29}$	6.873 $^{+0.033}_{-0.033}$	2.147 $^{+0.252}_{-0.237}$
457.5870	0.59 $^{+0.06}_{-0.08}$	567 $^{+80}_{-56}$	9.20 $^{+0.70}_{-0.53}$	0.66	6.22 $^{+0.28}_{-0.37}$	1.25 $^{+0.29}_{-0.25}$	5.568 $^{+0.028}_{-0.028}$	1.621 $^{+0.204}_{-0.191}$
460.9298	2.40 $^{+0.04}_{-0.04}$	4 $^{+411}_{-159}$	9.93 $^{+0.20}_{-0.26}$	0.46	6.38 $^{+0.55}_{-0.38}$	0.32 $^{+0.14}_{-0.11}$	4.096 $^{+0.018}_{-0.027}$	0.160 $^{+0.075}_{-0.056}$
463.5337	0.64 $^{+0.07}_{-0.06}$	571 $^{+51}_{-29}$	10.78 $^{+0.49}_{-0.48}$	0.76	5.76 $^{+0.41}_{-0.76}$	1.50 $^{+0.22}_{-0.22}$	5.418 $^{+0.027}_{-0.027}$	1.930 $^{+0.212}_{-0.220}$
466.0262	0.62 $^{+0.07}_{-0.06}$	560 $^{+49}_{-55}$	9.94 $^{+0.55}_{-0.53}$	0.76	6.56 $^{+0.41}_{-0.32}$	0.69 $^{+0.16}_{-0.33}$	3.987 $^{+0.016}_{-0.022}$	0.485 $^{+0.123}_{-0.108}$
467.0082	0.95 $^{+0.14}_{-0.14}$	407 $^{+81}_{-407}$	12.68 $^{+0.32}_{-0.59}$	0.59	6.38 $^{+0.36}_{-0.67}$	0.25 $^{+0.80}_{-0.25}$	4.505 $^{+0.014}_{-0.014}$	0.169 $^{+0.065}_{-0.050}$
468.9646	0.59 $^{+0.05}_{-0.05}$	528 $^{+152}_{-152}$	8.88 $^{+0.93}_{-0.93}$	0.93	7.00 $^{+0.00}_{-0.36}$	1.75 $^{+0.25}_{-0.20}$	3.015 $^{+0.018}_{-0.018}$	0.537 $^{+0.083}_{-0.078}$
472.7545	0.87 $^{+0.12}_{-0.11}$	401 $^{+80}_{-77}$	10.04 $^{+0.34}_{-0.45}$	0.95	6.79 $^{+0.69}_{-0.79}$	0.45 $^{+0.37}_{-0.11}$	3.408 $^{+0.010}_{-0.011}$	0.270 $^{+0.047}_{-0.044}$
474.4141	0.78 $^{+0.10}_{-0.07}$	440 $^{+50}_{-80}$	11.05 $^{+0.21}_{-0.19}$	0.98	6.06 $^{+0.36}_{-0.06}$	1.33 $^{+0.36}_{-0.31}$	3.452 $^{+0.005}_{-0.010}$	0.847 $^{+0.076}_{-0.073}$

<sup>a</sup> Unabsorbed flux of the EQPAIR model in units of  $10^{-9} \text{ erg s}^{-1} \text{ cm}^{-2}$ .

<sup>b</sup> Unabsorbed flux of the Gaussian component in units of  $10^{-12} \text{ erg s}^{-1} \text{ cm}^{-2}$ .

<sup>c</sup> Errors bars could not be constrained either due to low flux levels or degeneracies between model parameters.

**Table A.3** : Same as Table A.1 but for the 2011 outburst.

JD-55000 (days)	$l_h/l_s$	$kT_{bb}$ (eV)	$\tau_p$	$\chi^2/\text{d.o.f.}$	Line Energy (keV)	Line Width (keV)	Flux $^a_{eqpair}$	Flux $^b_{gauss}$
849.3771	3.38 $^{+0.18}_{-0.16}$	706 $^{+32}_{-34}$	0.91 $^{+0.06}_{-0.06}$	0.79	5.81 $^{+0.30}_{-0.81}$	1.46 $^{+0.30}_{-0.30}$	0.779 $^{+0.007}_{-0.007}$	0.225 $^{+0.026}_{-0.025}$
851.0042	2.93 $^{+0.09}_{-0.08}$	816 $^{+39}_{-39}$	1.67 $^{+0.15}_{-0.17}$	0.62	6.38 $^{+0.17}_{-0.20}$	0.82 $^{+0.25}_{-0.23}$	2.366 $^{+0.013}_{-0.011}$	0.320 $^{+0.049}_{-0.046}$
852.4341	2.95 $^{+0.10}_{-0.14}$	754 $^{+47}_{-65}$	1.40 $^{+0.15}_{-0.10}$	0.56	6.40 $^{+0.17}_{-0.22}$	0.62 $^{+0.29}_{-0.26}$	1.527 $^{+0.011}_{-0.011}$	0.164 $^{+0.036}_{-0.034}$
855.5781	0.61 $^{+0.05}_{-0.04}$	628 $^{+38}_{-39}$	10.89 $^{+0.33}_{-0.35}$	0.66	6.04 $^{+0.19}_{-0.22}$	1.21 $^{+0.18}_{-0.19}$	13.256 $^{+0.059}_{-0.058}$	5.105 $^{+0.477}_{-0.457}$
858.1831	0.60 $^{+0.04}_{-0.04}$	608 $^{+38}_{-38}$	10.22 $^{+0.33}_{-0.31}$	0.43	6.24 $^{+0.18}_{-0.21}$	1.00 $^{+0.19}_{-0.17}$	12.033 $^{+0.054}_{-0.054}$	3.419 $^{+0.394}_{-0.371}$
859.6397	1.58 $^{+0.04}_{-0.05}$	835 $^{+22}_{-22}$	5.78 $^{+0.32}_{-0.32}$	0.67	6.22 $^{+0.18}_{-0.20}$	1.08 $^{+0.22}_{-0.19}$	6.099 $^{+0.023}_{-0.024}$	1.123 $^{+0.131}_{-0.126}$
861.2436	0.83 $^{+0.10}_{-0.07}$	586 $^{+49}_{-64}$	11.94 $^{+0.37}_{-0.32}$	0.67	6.12 $^{+0.26}_{-0.30}$	1.09 $^{+0.26}_{-0.23}$	17.118 $^{+0.071}_{-0.071}$	3.932 $^{+0.574}_{-0.542}$
862.5005	0.66 $^{+0.06}_{-0.05}$	617 $^{+41}_{-41}$	11.56 $^{+0.37}_{-0.37}$	0.64	5.97 $^{+0.18}_{-0.20}$	1.26 $^{+0.15}_{-0.15}$	15.866 $^{+0.070}_{-0.070}$	7.209 $^{+0.582}_{-0.562}$
863.3370	0.68 $^{+0.06}_{-0.05}$	624 $^{+43}_{-49}$	11.67 $^{+0.35}_{-0.35}$	0.44	6.02 $^{+0.17}_{-0.19}$	1.30 $^{+0.15}_{-0.14}$	17.155 $^{+0.074}_{-0.074}$	8.264 $^{+0.620}_{-0.600}$
864.2519	0.62 $^{+0.05}_{-0.05}$	626 $^{+40}_{-40}$	11.00 $^{+0.35}_{-0.39}$	0.56	6.09 $^{+0.17}_{-0.20}$	1.19 $^{+0.16}_{-0.15}$	14.981 $^{+0.068}_{-0.067}$	6.448 $^{+0.539}_{-0.519}$
865.4324	0.56 $^{+0.04}_{-0.04}$	691 $^{+36}_{-36}$	10.64 $^{+0.37}_{-0.42}$	0.49	6.21 $^{+0.18}_{-0.21}$	1.19 $^{+0.18}_{-0.16}$	16.361 $^{+0.071}_{-0.072}$	6.067 $^{+0.562}_{-0.536}$
866.2953	0.66 $^{+0.06}_{-0.05}$	655 $^{+41}_{-43}$	11.77 $^{+0.38}_{-0.41}$	0.41	5.88 $^{+0.20}_{-0.23}$	1.40 $^{+0.17}_{-0.16}$	17.792 $^{+0.077}_{-0.077}$	8.830 $^{+0.668}_{-0.649}$
867.2469	0.61 $^{+0.05}_{-0.05}$	635 $^{+42}_{-42}$	11.04 $^{+0.36}_{-0.42}$	0.75	6.07 $^{+0.18}_{-0.21}$	1.24 $^{+0.17}_{-0.17}$	15.794 $^{+0.071}_{-0.071}$	7.012 $^{+0.580}_{-0.558}$
867.9782	0.68 $^{+0.07}_{-0.06}$	620 $^{+42}_{-52}$	11.53 $^{+0.39}_{-0.44}$	0.52	5.81 $^{+0.20}_{-0.21}$	1.42 $^{+0.17}_{-0.16}$	17.001 $^{+0.077}_{-0.077}$	9.215 $^{+0.660}_{-0.643}$
869.2827	0.63 $^{+0.05}_{-0.05}$	616 $^{+42}_{-42}$	11.07 $^{+0.34}_{-0.39}$	0.41	6.08 $^{+0.18}_{-0.21}$	1.19 $^{+0.17}_{-0.15}$	13.766 $^{+0.065}_{-0.060}$	5.515 $^{+0.490}_{-0.470}$
871.2931	0.68 $^{+0.07}_{-0.06}$	592 $^{+47}_{-50}$	11.39 $^{+0.37}_{-0.40}$	0.53	5.77 $^{+0.18}_{-0.22}$	1.41 $^{+0.15}_{-0.14}$	15.326 $^{+0.070}_{-0.070}$	9.212 $^{+0.602}_{-0.586}$
872.0839	0.57 $^{+0.03}_{-0.04}$	712 $^{+39}_{-26}$	10.92 $^{+0.36}_{-0.48}$	0.62	6.35 $^{+0.18}_{-0.21}$	1.09 $^{+0.19}_{-0.17}$	16.554 $^{+0.070}_{-0.072}$	5.194 $^{+0.545}_{-0.515}$
873.0034	0.94 $^{+0.37}_{-0.10}$	516 $^{+61}_{-115}$	12.55 $^{+0.44}_{-0.40}$	0.74	5.79 $^{+0.22}_{-0.20}$	1.28 $^{+0.18}_{-0.21}$	17.867 $^{+0.079}_{-0.066}$	6.780 $^{+0.642}_{-0.623}$
875.6732	0.58 $^{+0.10}_{-0.04}$	684 $^{+32}_{-41}$	11.00 $^{+0.40}_{-0.49}$	0.62	6.31 $^{+0.20}_{-0.24}$	1.17 $^{+0.21}_{-0.19}$	15.484 $^{+0.066}_{-0.067}$	5.087 $^{+0.532}_{-0.504}$
876.8402	0.89 $^{+0.12}_{-0.03}$	548 $^{+36}_{-66}$	12.72 $^{+0.21}_{-0.25}$	0.57	6.13 $^{+0.21}_{-0.24}$	1.20 $^{+0.20}_{-0.18}$	16.308 $^{+0.067}_{-0.066}$	5.238 $^{+0.551}_{-0.528}$
877.4295	0.56 $^{+0.04}_{-0.03}$	689 $^{+30}_{-36}$	10.47 $^{+0.33}_{-0.38}$	0.56	6.33 $^{+0.18}_{-0.21}$	1.07 $^{+0.19}_{-0.17}$	14.428 $^{+0.063}_{-0.062}$	4.497 $^{+0.474}_{-0.448}$
877.8880	0.74 $^{+0.08}_{-0.06}$	572 $^{+49}_{-55}$	11.80 $^{+0.34}_{-0.35}$	0.62	5.82 $^{+0.19}_{-0.82}$	1.36 $^{+0.17}_{-0.15}$	14.142 $^{+0.063}_{-0.062}$	6.943 $^{+0.532}_{-0.517}$
879.5833	0.64 $^{+0.06}_{-0.05}$	601 $^{+41}_{-50}$	11.10 $^{+0.37}_{-0.38}$	0.56	5.86 $^{+0.22}_{-0.86}$	1.37 $^{+0.20}_{-0.18}$	11.754 $^{+0.054}_{-0.054}$	5.345 $^{+0.451}_{-0.436}$
880.6295	0.61 $^{+0.05}_{-0.05}$	631 $^{+40}_{-41}$	10.97 $^{+0.37}_{-0.40}$	0.73	6.19 $^{+0.18}_{-0.21}$	1.18 $^{+0.18}_{-0.16}$	12.253 $^{+0.055}_{-0.055}$	4.687 $^{+0.430}_{-0.410}$
882.6413	0.71 $^{+0.09}_{-0.06}$	580 $^{+49}_{-41}$	11.71 $^{+0.41}_{-0.37}$	0.59	5.89 $^{+0.20}_{-0.20}$	1.28 $^{+0.18}_{-0.21}$	12.552 $^{+0.057}_{-0.054}$	5.804 $^{+0.478}_{-0.443}$
883.5596	0.68 $^{+0.06}_{-0.06}$	607 $^{+49}_{-49}$	11.41 $^{+0.42}_{-0.38}$	0.61	6.14 $^{+0.22}_{-0.24}$	1.16 $^{+0.19}_{-0.19}$	12.691 $^{+0.057}_{-0.057}$	4.229 $^{+0.462}_{-0.422}$
884.6704	0.63 $^{+0.05}_{-0.05}$	591 $^{+43}_{-43}$	10.71 $^{+0.33}_{-0.37}$	0.87	6.20 $^{+0.19}_{-0.22}$	1.08 $^{+0.19}_{-0.18}$	9.544 $^{+0.043}_{-0.044}$	3.094 $^{+0.328}_{-0.311}$
885.8371	0.62 $^{+0.04}_{-0.04}$	607 $^{+32}_{-32}$	10.52 $^{+0.34}_{-0.27}$	0.60	6.28 $^{+0.18}_{-0.22}$	1.08 $^{+0.20}_{-0.18}$	9.571 $^{+0.041}_{-0.041}$	2.921 $^{+0.317}_{-0.299}$
886.8228	0.80 $^{+0.11}_{-0.07}$	554 $^{+72}_{-72}$	12.03 $^{+0.35}_{-0.51}$	0.72	6.23 $^{+0.22}_{-0.26}$	0.99 $^{+0.22}_{-0.22}$	11.192 $^{+0.046}_{-0.048}$	2.536 $^{+0.360}_{-0.338}$
888.2533	0.60 $^{+0.04}_{-0.04}$	586 $^{+37}_{-37}$	9.93 $^{+0.30}_{-0.38}$	0.52	6.30 $^{+0.19}_{-0.19}$	1.04 $^{+0.19}_{-0.17}$	8.085 $^{+0.037}_{-0.038}$	2.324 $^{+0.264}_{-0.248}$
890.0729	0.59 $^{+0.04}_{-0.04}$	605 $^{+39}_{-39}$	9.82 $^{+0.36}_{-0.36}$	0.61	6.43 $^{+0.23}_{-0.23}$	0.96 $^{+0.22}_{-0.20}$	7.560 $^{+0.035}_{-0.035}$	1.874 $^{+0.222}_{-0.222}$
891.1884	0.62 $^{+0.04}_{-0.04}$	596 $^{+37}_{-48}$	10.43 $^{+0.37}_{-0.35}$	0.75	6.16 $^{+0.20}_{-0.24}$	1.21 $^{+0.20}_{-0.18}$	7.825 $^{+0.032}_{-0.035}$	2.782 $^{+0.222}_{-0.262}$
892.2633	0.67 $^{+0.07}_{-0.07}$	565 $^{+48}_{-48}$	10.94 $^{+0.37}_{-0.39}$	0.39	5.80 $^{+0.24}_{-0.80}$	1.45 $^{+0.19}_{-0.06}$	7.619 $^{+0.035}_{-0.036}$	3.777 $^{+0.300}_{-0.290}$
893.4686	0.67 $^{+0.08}_{-0.06}$	570 $^{+51}_{-58}$	11.29 $^{+0.40}_{-0.43}$	0.69	6.06 $^{+0.27}_{-0.32}$	1.16 $^{+0.26}_{-0.23}$	7.265 $^{+0.034}_{-0.034}$	1.971 $^{+0.264}_{-0.269}$
894.3870	0.62 $^{+0.05}_{-0.05}$	542 $^{+48}_{-48}$	9.72 $^{+0.34}_{-0.33}$	0.59	6.34 $^{+0.20}_{-0.30}$	0.99 $^{+0.26}_{-0.23}$	5.417 $^{+0.026}_{-0.026}$	1.141 $^{+0.175}_{-0.141}$

**Table A.3 (continued)** : Same as Table A.1 but for the 2011 outburst.

JD-55000 (days)	$l_h/l_s$	$kT_{bb}$ (eV)	$\tau_p$	$\chi^2/\text{d.o.f.}$	Line Energy (keV)	Line Width (keV)	Flux <sup>a</sup> <sub>eqpair</sub>	Flux <sup>b</sup> <sub>gauss</sub>
895.2340	0.58 <sup>+0.04</sup> <sub>-0.04</sub>	590 <sup>+37</sup> <sub>-37</sub>	9.68 <sup>+0.36</sup> <sub>-0.36</sub>	0.60	6.38 <sup>+0.25</sup> <sub>-0.32</sub>	1.06 <sup>+0.27</sup> <sub>-0.24</sub>	5.619 <sup>+0.026</sup> <sub>-0.026</sub>	1.233 <sup>+0.184</sup> <sub>-0.170</sub>
896.1426	0.82 <sup>+0.23</sup> <sub>-0.10</sub>	487 <sup>+70</sup> <sub>-127</sub>	12.02 <sup>+0.37</sup> <sub>-0.21</sub>	0.69	6.43 <sup>+0.25</sup> <sub>-0.34</sub>	0.73 <sup>+0.36</sup> <sub>-0.30</sub>	5.939 <sup>+0.027</sup> <sub>-0.027</sub>	0.699 <sup>+0.174</sup> <sub>-0.153</sub>
898.1645	2.30 <sup>+0.28</sup> <sub>-1.57</sub>	1 <sup>+394</sup> <sub>-1</sub>	9.50 <sup>+0.15</sup> <sub>-0.14</sub>	0.92	6.73 <sup>+0.21</sup> <sub>-0.25</sub>	0.70 <sup>+0.30</sup> <sub>-0.26</sub>	3.318 <sup>+0.010</sup> <sub>-0.010</sub>	0.389 <sup>+0.050</sup> <sub>-0.046</sub>
899.0077	0.74 <sup>+0.19</sup> <sub>-0.13</sub>	444 <sup>+100</sup> <sub>-137</sub>	9.92 <sup>+0.38</sup> <sub>-0.26</sub>	1.09	6.51 <sup>+0.23</sup> <sub>-0.31</sub>	0.84 <sup>+0.34</sup> <sub>-0.26</sub>	3.561 <sup>+0.019</sup> <sub>-0.019</sub>	0.580 <sup>+0.111</sup> <sub>-0.099</sub>
901.2278	2.90 <sup>+0.17</sup> <sub>-2.15</sub>	1 <sup>+416</sup> <sub>-1</sub>	10.14 <sup>+0.17</sup> <sub>-0.11</sub>	0.66	6.10 <sup>+0.30</sup> <sub>-0.41</sub>	1.34 <sup>+0.32</sup> <sub>-0.26</sub>	2.852 <sup>+0.007</sup> <sub>-0.006</sub>	0.953 <sup>+0.066</sup> <sub>-0.064</sub>
902.0756	0.79 <sup>+1.67</sup> <sub>-0.12</sub>	407 <sup>+90</sup> <sub>-407</sub>	10.57 <sup>+0.42</sup> <sub>-0.52</sub>	0.65	6.54 <sup>+0.23</sup> <sub>-0.31</sub>	0.89 <sup>+0.32</sup> <sub>-0.26</sub>	2.408 <sup>+0.013</sup> <sub>-0.013</sub>	0.453 <sup>+0.080</sup> <sub>-0.073</sub>
903.1209	2.24 <sup>+0.77</sup> <sub>-1.35</sub>	23 <sup>+320</sup> <sub>-23</sub>	10.88 <sup>+0.24</sup> <sub>-0.22</sub>	0.76	6.77 <sup>+0.20</sup> <sub>-0.23</sub>	0.77 <sup>+0.31</sup> <sub>-0.26</sub>	1.550 <sup>+0.005</sup> <sub>-0.005</sub>	0.254 <sup>+0.028</sup> <sub>-0.027</sub>
904.0978	0.99 <sup>+0.25</sup> <sub>-0.23</sub>	199 <sup>+194</sup> <sub>-443</sub>	7.77 <sup>+0.11</sup> <sub>-0.10</sub>	1.08	6.03 <sup>+0.26</sup> <sub>-0.32</sub>	1.42 <sup>+0.26</sup> <sub>-0.21</sub>	1.037 <sup>+0.004</sup> <sub>-0.004</sub>	0.644 <sup>+0.029</sup> <sub>-0.029</sub>
889.1765	0.98 <sup>+5.33</sup> <sub>-0.14</sub>	443 <sup>+85</sup> <sub>-443</sub>	12.50 <sup>+0.35</sup> <sub>-0.36</sub>	0.78	5.83 <sup>+0.26</sup> <sub>-0.33</sub>	1.12 <sup>+0.23</sup> <sub>-0.20</sub>	9.245 <sup>+0.042</sup> <sub>-0.040</sub>	2.139 <sup>+0.329</sup> <sub>-0.312</sub>
900.3845	1.26 <sup>+1.50</sup> <sub>-0.54</sub>	142 <sup>+302</sup> <sub>-142</sub>	10.08 <sup>+0.29</sup> <sub>-0.29</sub>	1.00	6.15 <sup>+0.33</sup> <sub>-0.44</sub>	1.47 <sup>+0.00</sup> <sub>-0.27</sub>	2.751 <sup>+0.015</sup> <sub>-0.015</sub>	0.722 <sup>+0.108</sup> <sub>-0.100</sub>
905.3416	0.57 <sup>+0.05</sup> <sub>-0.05</sub>	291 <sup>+30</sup> <sub>-37</sub>	0.40 <sup>+0.07</sup> <sub>-0.05</sub>	0.62	5.60 <sup>+0.18</sup> <sub>-0.60</sub>	1.61 <sup>+0.09</sup> <sub>-0.14</sub>	0.778 <sup>+0.006</sup> <sub>-0.006</sub>	0.523 <sup>+0.027</sup> <sub>-0.030</sub>
906.0508	1.57 <sup>+0.07</sup> <sub>-0.07</sub>	672 <sup>+70</sup> <sub>-162</sub>	1.44 <sup>+0.58</sup> <sub>-0.18</sub>	1.00	5.60 <sup>+0.15</sup> <sub>-5.60</sub>	1.22 <sup>+0.19</sup> <sub>-0.19</sub>	0.686 <sup>+0.002</sup> <sub>-0.012</sub>	0.182 <sup>+0.024</sup> <sub>-0.024</sub>
907.3148	2.67 <sup>+0.14</sup> <sub>-0.14</sub>	684 <sup>+28</sup> <sub>-28</sub>	0.71 <sup>+0.04</sup> <sub>-0.04</sub>	0.80	5.65 <sup>+0.15</sup> <sub>-5.65</sub>	1.39 <sup>+0.14</sup> <sub>-0.14</sub>	0.476 <sup>+0.004</sup> <sub>-0.004</sub>	0.228 <sup>+0.015</sup> <sub>-0.015</sub>
908.2906	2.72 <sup>+0.09</sup> <sub>-0.19</sub>	823 <sup>+29</sup> <sub>-59</sub>	0.91 <sup>+0.09</sup> <sub>-0.04</sub>	3.48	5.60 <sup>c</sup>	0.51 <sup>c</sup>	0.358 <sup>+0.002</sup> <sub>-0.006</sub>	0.000 <sup>+0.000</sup> <sub>-0.000</sub>
909.0731	2.67 <sup>+0.19</sup> <sub>-0.31</sub>	697 <sup>+56</sup> <sub>-68</sub>	0.97 <sup>+0.12</sup> <sub>-0.04</sub>	1.66	6.79 <sup>c</sup>	0.25 <sup>+1.26</sup> <sub>-0.25</sub>	0.253 <sup>+0.003</sup> <sub>-0.005</sub>	0.006 <sup>+0.005</sup> <sub>-0.005</sub>
910.2218	3.58 <sup>+1.18</sup> <sub>-0.87</sub>	668 <sup>+111</sup> <sub>-115</sub>	0.84 <sup>+0.24</sup> <sub>-0.22</sub>	0.69	6.41 <sup>c</sup>	0.25 <sup>+1.20</sup> <sub>-0.25</sub>	0.115 <sup>+0.006</sup> <sub>-0.006</sub>	0.011 <sup>+0.006</sup> <sub>-0.006</sub>
904.1780	1.66 <sup>c</sup> <sub>-0.94</sub>	1 <sup>+387</sup> <sub>-1</sub>	7.52 <sup>+0.11</sup> <sub>-0.11</sub>	0.83	5.73 <sup>+0.17</sup> <sub>-0.11</sub>	1.74 <sup>c</sup> <sub>-0.11</sub>	1.011 <sup>+0.005</sup> <sub>-0.006</sub>	0.911 <sup>+0.039</sup> <sub>-0.045</sub>
904.3096	0.80 <sup>+0.79</sup> <sub>-0.10</sub>	334 <sup>+98</sup> <sub>-327</sub>	7.76 <sup>+0.14</sup> <sub>-0.15</sub>	0.75	5.74 <sup>+0.17</sup> <sub>-0.10</sub>	1.75 <sup>c</sup> <sub>-0.11</sub>	0.988 <sup>+0.005</sup> <sub>-0.006</sub>	0.863 <sup>+0.036</sup> <sub>-0.042</sub>
906.3936	1.92 <sup>+0.07</sup> <sub>-0.08</sub>	736 <sup>+91</sup> <sub>-231</sub>	1.30 <sup>+0.36</sup> <sub>-0.22</sub>	1.26	5.60 <sup>+0.21</sup> <sub>-5.60</sub>	1.15 <sup>+0.22</sup> <sub>-0.21</sub>	0.640 <sup>+0.002</sup> <sub>-0.013</sub>	0.154 <sup>+0.026</sup> <sub>-0.026</sub>
908.0061	2.27 <sup>+0.23</sup> <sub>-0.18</sub>	778 <sup>+68</sup> <sub>-121</sub>	1.15 <sup>+0.26</sup> <sub>-0.13</sub>	1.60	5.60 <sup>c</sup>	1.21 <sup>c</sup>	0.399 <sup>+0.007</sup> <sub>-0.007</sub>	0.000 <sup>+0.000</sup> <sub>-0.000</sub>
909.2486	2.63 <sup>+0.31</sup> <sub>-0.23</sub>	683 <sup>+82</sup> <sub>-99</sub>	1.06 <sup>+0.14</sup> <sub>-0.14</sub>	1.56	6.02 <sup>c</sup>	0.25 <sup>c</sup>	0.238 <sup>+0.005</sup> <sub>-0.004</sub>	0.000 <sup>+0.000</sup> <sub>-0.000</sub>
910.9905	2.65 <sup>c</sup>	529 <sup>+770</sup> <sub>-529</sub>	0.83 <sup>c</sup>	0.66	7.00 <sup>c</sup>	0.25 <sup>c</sup>	0.069 <sup>+0.016</sup> <sub>-0.011</sub>	0.316 <sup>+0.000</sup> <sub>-0.000</sub>
912.1792	8.65 <sup>+10.74</sup> <sub>-5.72</sub>	1009 <sup>+224</sup> <sub>-538</sub>	1.17 <sup>+0.30</sup> <sub>-0.34</sub>	0.86	6.79 <sup>c</sup>	1.70 <sup>c</sup>	0.046 <sup>+0.004</sup> <sub>-0.005</sub>	0.000 <sup>+0.000</sup> <sub>-0.000</sub>
911.0143	4.50 <sup>+5.59</sup> <sub>-1.00</sub>	1011 <sup>+288</sup> <sub>-959</sub>	1.11 <sup>+2.48</sup> <sub>-0.14</sub>	0.82	5.94 <sup>c</sup>	0.25 <sup>c</sup>	0.076 <sup>+0.006</sup> <sub>-0.003</sub>	0.002 <sup>+0.007</sup> <sub>-0.000</sub>
913.2270	21.81 <sup>+63.58</sup> <sub>-18.50</sub>	1210 <sup>+526</sup> <sub>-687</sub>	1.63 <sup>c</sup>	0.54	5.60 <sup>c</sup>	1.49 <sup>c</sup>	0.031 <sup>+0.006</sup> <sub>-0.006</sub>	0.000 <sup>+0.000</sup> <sub>-0.000</sub>
914.1906	13.72 <sup>+57.73</sup> <sub>-13.19</sub>	1070 <sup>c</sup>	0.01 <sup>c</sup>	0.82	6.64 <sup>c</sup>	0.80 <sup>c</sup>	0.017 <sup>+0.006</sup> <sub>-0.007</sub>	0.013 <sup>+0.014</sup> <sub>-0.011</sub>
915.0509	13.95 <sup>+33.88</sup> <sub>-11.33</sub>	1154 <sup>+261</sup> <sub>-430</sub>	0.98 <sup>c</sup>	0.77	7.00 <sup>c</sup>	0.25 <sup>c</sup>	0.016 <sup>+0.004</sup> <sub>-0.004</sub>	0.004 <sup>+0.010</sup> <sub>-0.000</sub>
916.1545	87.75 <sup>+306.47</sup> <sub>-69.32</sub>	1195 <sup>+467</sup> <sub>-210</sub>	10.07 <sup>c</sup>	0.74	5.60 <sup>+0.90</sup> <sub>-5.60</sub>	1.17 <sup>c</sup>	0.020 <sup>+0.004</sup> <sub>-0.005</sub>	0.009 <sup>+0.008</sup> <sub>-0.008</sub>

<sup>a</sup> Unabsorbed flux of the EQPAIR model in units of  $10^{-9} \text{ erg s}^{-1} \text{ cm}^{-2}$ .

<sup>b</sup> Unabsorbed flux of the Gaussian component in units of  $10^{-12} \text{ erg s}^{-1} \text{ cm}^{-2}$ .

<sup>c</sup> Error bars could not be constrained either due to low flux level or degeneracy between model parameters.



**APPENDIX B:** Best fit parameters of *black body + disk black body + Gauss* model of RXTE/PCA data during the 2000 and the 2011 outbursts of Aql X-1

**Table B.1 :** Best fit parameters of *black body + disk black body + Gauss* model for the 2000 outburst of RXTE/PCA data.

Obs Number	ObsID	JD-51000 (days)	$kT_{bbody}$ (keV)	$kT_{diskbb}$ (keV)	$\chi^2$	Hardness <sup>a</sup> bbbody	Hardness <sup>a</sup> diskbb	Flux <sup>b</sup> bbbody	Flux <sup>c</sup> diskbb
1	50049-01-03-00	811.28564	$5.27 \pm 1.12$	$1.19 \pm 0.15$	0.90	$4.36 \pm 1.97$	$1.50 \pm 0.06$	$1.63 \pm 0.08$	$0.60 \pm 0.01$
2	50049-01-03-01	812.34953	$6.96 \pm 1.23$	$1.58 \pm 0.10$	1.14	$6.89 \pm 2.81$	$5.45 \pm 0.13$	$2.70 \pm 0.52$	$1.68 \pm 0.02$
3	50049-01-03-02	813.27735	$6.63 \pm 1.40$	$1.64 \pm 0.09$	1.00	$6.41 \pm 1.69$	$6.43 \pm 0.13$	$4.27 \pm 0.49$	$2.63 \pm 0.03$
4	50049-01-04-00	816.46667	$4.08 \pm 0.71$	$2.10 \pm 0.10$	1.13	$2.64 \pm 0.92$	$14.93 \pm 0.20$	$7.95 \pm 1.67$	$11.29 \pm 0.08$
5	50049-01-04-01	817.79791	$5.88 \pm 0.16$	$2.35 \pm 0.05$	1.24	$5.29 \pm 0.36$	$20.77 \pm 0.25$	$22.94 \pm 0.40$	$18.80 \pm 0.11$
6	50049-01-04-04	822.77448	$2.40 \pm 0.08$	$1.63 \pm 0.07$	0.69	$0.65 \pm 0.19$	$6.23 \pm 0.07$	$27.16 \pm 4.01$	$77.91 \pm 0.44$
7	50049-01-05-00	823.76888	$2.38 \pm 0.07$	$1.71 \pm 0.07$	0.57	$0.64 \pm 0.06$	$7.40 \pm 0.14$	$35.20 \pm 0.20$	$90.30 \pm 0.50$
8	50049-01-05-01	824.76115	$2.28 \pm 0.05$	$1.56 \pm 0.08$	0.38	$0.56 \pm 0.11$	$5.15 \pm 0.07$	$47.76 \pm 4.49$	$72.13 \pm 0.48$
9	50049-01-05-02	825.75496	$2.29 \pm 0.08$	$1.57 \pm 0.08$	0.63	$0.57 \pm 0.16$	$5.31 \pm 0.06$	$31.39 \pm 4.32$	$71.95 \pm 0.44$
10	50049-02-01-00	826.51291	$2.31 \pm 0.05$	$1.64 \pm 0.07$	0.39	$0.59 \pm 0.12$	$6.31 \pm 0.07$	$44.55 \pm 4.34$	$86.14 \pm 0.52$
11	50049-02-02-00	828.53443	$2.34 \pm 0.05$	$1.61 \pm 0.05$	0.75	$0.61 \pm 0.12$	$5.96 \pm 0.06$	$30.32 \pm 3.03$	$79.80 \pm 0.45$
12	50049-02-03-00	833.45856	$2.28 \pm 0.07$	$1.57 \pm 0.07$	0.81	$0.57 \pm 0.15$	$5.30 \pm 0.06$	$33.46 \pm 4.39$	$79.95 \pm 0.47$
13	50049-02-03-01	831.20242	$2.32 \pm 0.07$	$1.62 \pm 0.08$	0.49	$0.59 \pm 0.15$	$6.12 \pm 0.07$	$37.45 \pm 4.64$	$75.74 \pm 0.46$
14	50049-02-03-02	835.19034	$2.21 \pm 0.06$	$1.49 \pm 0.07$	0.40	$0.51 \pm 0.11$	$4.33 \pm 0.06$	$28.15 \pm 2.96$	$50.67 \pm 0.33$
15	50049-02-04-00	834.30025	$2.31 \pm 0.04$	$1.63 \pm 0.06$	0.31	$0.59 \pm 0.09$	$6.16 \pm 0.08$	$51.16 \pm 4.02$	$87.91 \pm 0.55$
16	50049-02-05-00	835.47605	$2.32 \pm 0.06$	$1.65 \pm 0.07$	0.30	$0.59 \pm 0.14$	$6.58 \pm 0.07$	$40.02 \pm 4.54$	$90.68 \pm 0.52$
17	50049-02-06-00	836.51501	$2.35 \pm 0.08$	$1.66 \pm 0.08$	0.45	$0.62 \pm 0.18$	$6.73 \pm 0.08$	$38.97 \pm 5.37$	$92.11 \pm 0.52$
18	50049-02-06-01	836.59062	$2.31 \pm 0.08$	$1.65 \pm 0.09$	0.61	$0.58 \pm 0.19$	$6.47 \pm 0.08$	$44.63 \pm 6.76$	$89.74 \pm 0.55$
19	50049-02-06-02	836.65903	$2.25 \pm 0.09$	$1.58 \pm 0.09$	0.41	$0.54 \pm 0.19$	$5.53 \pm 0.07$	$37.83 \pm 6.14$	$79.84 \pm 0.50$
20	50049-02-07-00	837.31072	$2.30 \pm 0.07$	$1.64 \pm 0.09$	0.59	$0.58 \pm 0.16$	$6.34 \pm 0.08$	$45.08 \pm 5.90$	$86.81 \pm 0.54$
21	50049-02-07-01	838.58253	$2.26 \pm 0.08$	$1.56 \pm 0.08$	0.78	$0.55 \pm 0.16$	$5.21 \pm 0.07$	$35.25 \pm 4.99$	$75.20 \pm 0.47$
22	50049-02-07-02	839.16547	$2.33 \pm 0.07$	$1.66 \pm 0.07$	0.38	$0.60 \pm 0.16$	$6.59 \pm 0.08$	$40.72 \pm 5.23$	$88.67 \pm 0.51$
23	50049-02-07-03	841.42330	$2.29 \pm 0.07$	$1.52 \pm 0.08$	0.83	$0.57 \pm 0.14$	$4.67 \pm 0.06$	$29.26 \pm 3.45$	$63.35 \pm 0.40$
24	50049-02-07-04	843.42348	$2.34 \pm 0.08$	$1.65 \pm 0.08$	0.47	$0.61 \pm 0.19$	$6.52 \pm 0.08$	$35.51 \pm 5.09$	$79.77 \pm 0.46$
25	50049-02-08-00	844.12055	$2.31 \pm 0.05$	$1.62 \pm 0.06$	0.44	$0.58 \pm 0.13$	$6.06 \pm 0.07$	$33.90 \pm 3.53$	$74.70 \pm 0.44$
26	50049-02-08-01	845.14572	$2.25 \pm 0.06$	$1.53 \pm 0.09$	0.29	$0.54 \pm 0.11$	$4.80 \pm 0.07$	$45.79 \pm 4.64$	$64.78 \pm 0.45$
27	50049-02-08-03	846.20867	$2.27 \pm 0.07$	$1.56 \pm 0.08$	0.47	$0.55 \pm 0.15$	$5.20 \pm 0.06$	$30.71 \pm 3.89$	$65.45 \pm 0.42$
28	50049-02-10-00	850.10229	$2.29 \pm 0.05$	$1.61 \pm 0.06$	0.38	$0.57 \pm 0.12$	$5.92 \pm 0.07$	$28.52 \pm 2.95$	$63.79 \pm 0.36$
29	50049-02-10-01	849.53465	$2.36 \pm 0.11$	$1.63 \pm 0.09$	0.89	$0.62 \pm 0.24$	$6.26 \pm 0.07$	$26.61 \pm 4.62$	$67.68 \pm 0.40$
30	50049-02-10-02	849.46316	$2.36 \pm 0.11$	$1.65 \pm 0.09$	0.79	$0.63 \pm 0.26$	$6.47 \pm 0.07$	$25.65 \pm 4.95$	$68.85 \pm 0.40$
31	50049-02-10-03	849.39406	$2.29 \pm 0.11$	$1.57 \pm 0.10$	0.48	$0.57 \pm 0.24$	$5.37 \pm 0.06$	$23.76 \pm 4.69$	$60.09 \pm 0.37$
32	50049-02-10-05	850.86400	$2.25 \pm 0.06$	$1.56 \pm 0.08$	0.72	$0.54 \pm 0.14$	$5.18 \pm 0.06$	$29.09 \pm 3.53$	$56.65 \pm 0.36$
33	50049-02-11-01	852.58772	$2.23 \pm 0.11$	$1.54 \pm 0.10$	1.13	$0.53 \pm 0.23$	$5.01 \pm 0.06$	$24.38 \pm 4.74$	$53.92 \pm 0.34$
34	50049-02-11-02	852.65313	$2.28 \pm 0.16$	$1.60 \pm 0.13$	0.73	$0.56 \pm 0.34$	$5.70 \pm 0.07$	$24.49 \pm 5.96$	$57.21 \pm 0.37$
35	50049-02-12-00	854.27232	$2.33 \pm 0.06$	$1.54 \pm 0.07$	0.76	$0.60 \pm 0.13$	$4.90 \pm 0.06$	$18.68 \pm 2.09$	$45.47 \pm 0.28$
36	50049-02-12-01	853.58329	$2.21 \pm 0.09$	$1.49 \pm 0.09$	0.57	$0.51 \pm 0.15$	$4.35 \pm 0.06$	$25.43 \pm 3.74$	$48.45 \pm 0.33$
37	50049-02-13-00	855.30361	$2.11 \pm 0.04$	$1.18 \pm 0.05$	0.87	$0.45 \pm 0.04$	$1.40 \pm 0.02$	$19.59 \pm 0.99$	$25.38 \pm 0.21$
38	50049-02-14-00	856.96964	$2.25 \pm 0.05$	$1.42 \pm 0.07$	0.82	$0.54 \pm 0.10$	$3.54 \pm 0.05$	$18.73 \pm 1.78$	$34.56 \pm 0.24$
39	50049-02-15-00	859.24090	$2.20 \pm 0.05$	$1.37 \pm 0.07$	0.99	$0.50 \pm 0.08$	$2.97 \pm 0.04$	$15.66 \pm 1.44$	$25.45 \pm 0.19$
40	50049-02-15-01	860.21521	$2.14 \pm 0.10$	$1.41 \pm 0.13$	0.63	$0.46 \pm 0.16$	$3.35 \pm 0.05$	$14.95 \pm 2.78$	$25.42 \pm 0.19$
41	50049-02-15-02	861.11940	$2.20 \pm 0.06$	$1.34 \pm 0.08$	1.12	$0.50 \pm 0.08$	$2.71 \pm 0.04$	$11.94 \pm 0.89$	$19.12 \pm 0.15$
42	50049-02-15-03	861.88606	$2.06 \pm 0.04$	$1.12 \pm 0.05$	0.84	$0.41 \pm 0.04$	$1.05 \pm 0.02$	$9.99 \pm 0.53$	$11.14 \pm 0.10$
43	50049-02-15-04	862.09305	$2.11 \pm 0.05$	$1.13 \pm 0.05$	1.35	$0.45 \pm 0.05$	$1.10 \pm 0.02$	$9.18 \pm 0.57$	$10.45 \pm 0.10$
44	50049-02-15-05	863.23997	$2.45 \pm 0.08$	$1.28 \pm 0.06$	1.72	$0.70 \pm 0.09$	$2.13 \pm 0.03$	$5.78 \pm 0.39$	$9.03 \pm 0.08$
45	50049-02-15-06	864.20819	$2.12 \pm 0.11$	$1.16 \pm 0.08$	0.83	$0.45 \pm 0.10$	$1.27 \pm 0.03$	$6.07 \pm 0.67$	$7.24 \pm 0.07$
46	50049-02-15-07	864.27747	$2.24 \pm 0.15$	$1.17 \pm 0.08$	0.85	$0.54 \pm 0.14$	$1.31 \pm 0.03$	$5.46 \pm 0.70$	$7.19 \pm 0.08$
47	50049-02-15-08	860.54742	$2.10 \pm 0.10$	$1.18 \pm 0.08$	1.01	$0.44 \pm 0.10$	$1.43 \pm 0.03$	$12.74 \pm 1.58$	$15.82 \pm 0.15$
48	50049-03-01-00	865.27217	$4.43 \pm 0.34$	$1.86 \pm 0.07$	1.48	$3.10 \pm 0.61$	$10.09 \pm 0.17$	$3.99 \pm 0.17$	$5.83 \pm 0.05$
49	50049-03-02-00	866.97790	$6.05 \pm 0.89$	$1.67 \pm 0.17$	0.96	$5.55 \pm 4.06$	$6.88 \pm 0.15$	$3.55 \pm 1.55$	$2.45 \pm 0.03$
50	50049-03-02-01	866.92250	$4.73 \pm 0.46$	$1.74 \pm 0.11$	0.99	$3.53 \pm 0.63$	$7.87 \pm 0.25$	$3.64 \pm 0.16$	$2.63 \pm 0.04$
51	50049-03-03-00	868.23607	$6.56 \pm 1.37$	$1.44 \pm 0.16$	0.74	$6.31 \pm 4.82$	$3.75 \pm 0.14$	$2.17 \pm 1.49$	$1.12 \pm 0.02$
52	50049-03-04-00	869.47435	$6.88 \pm 1.28$	$1.32 \pm 0.20$	0.86	$6.78 \pm 4.38$	$2.49 \pm 0.11$	$0.95 \pm 0.47$	$0.38 \pm 0.01$

<sup>a</sup> Hardness parameters are obtained using the flux ratio of two different energy ranges;  $L(10 - 30 \text{ keV})/L(3 - 10 \text{ keV})$ . The parameters for diskbb component are multiplied by  $10^2$  because of low values

<sup>b</sup> Unabsorbed flux of the bbody component in units of  $10^{-10} \text{ erg s}^{-1} \text{ cm}^{-2}$ .

<sup>c</sup> Unabsorbed flux of the diskbb component in units of  $10^{-10} \text{ erg s}^{-1} \text{ cm}^{-2}$ .

**Table B.2** : Same as Table B.1 but for the 2011 outburst.

Obs Number	ObsID	JD–55000 (days)	$kT_{\text{bbody}}$ (keV)	$kT_{\text{diskbb}}$ (keV)	$\chi^2$	Hardness <sup>a</sup> bbody	Hardness <sup>a</sup> diskbb	Flux <sup>b</sup> bbody	Flux <sup>c</sup> diskbb
1	96440-01-01-00	849.3771	8.04 ± 1.71	1.63 ± 0.07	1.09	8.39 ± 0.32	6.19 ± 0.12	3.74 ± 0.07	2.76 ± 0.03
2	96440-01-01-01	852.4442	12.11 ± 4.58	2.06 ± 0.05	0.98	12.77 ± 0.42	14.08 ± 0.19	6.83 ± 0.11	9.78 ± 0.06
3	96440-01-02-00	858.1840	2.24 ± 0.05	1.55 ± 0.06	0.60	0.53 ± 0.01	5.10 ± 0.06	43.52 ± 0.25	91.63 ± 0.54
4	96440-01-02-01	861.2549	2.50 ± 0.03	1.69 ± 0.01	1.10	0.74 ± 0.01	3.97 ± 0.20	26.10 ± 0.51	78.60 ± 0.34
5	96440-01-02-02	855.5727	5.33 ± 0.13	2.45 ± 0.05	1.11	4.45 ± 0.06	23.44 ± 0.26	31.11 ± 0.19	30.63 ± 0.17
6	96440-01-02-03	859.6329	2.32 ± 0.05	1.57 ± 0.08	0.54	0.59 ± 0.01	5.36 ± 0.07	74.03 ± 0.41	98.06 ± 0.69
7	96440-01-03-00	864.2559	2.24 ± 0.06	1.57 ± 0.07	0.61	0.53 ± 0.01	5.41 ± 0.07	54.97 ± 0.32	107.14 ± 0.65
8	96440-01-03-01	867.2569	2.30 ± 0.06	1.64 ± 0.06	0.38	0.58 ± 0.01	6.37 ± 0.07	57.38 ± 0.32	118.24 ± 0.68
9	96440-01-03-02	862.4965	2.24 ± 0.06	1.55 ± 0.07	0.54	0.53 ± 0.01	5.12 ± 0.06	50.02 ± 0.32	102.58 ± 0.63
10	96440-01-03-03	865.4324	2.34 ± 0.08	1.66 ± 0.06	0.42	0.61 ± 0.01	6.66 ± 0.07	47.21 ± 0.33	119.18 ± 0.65
11	96440-01-03-04	867.9826	2.32 ± 0.07	1.68 ± 0.07	0.37	0.60 ± 0.01	7.02 ± 0.08	56.88 ± 0.37	125.92 ± 0.74
12	96440-01-03-05	863.3270	2.25 ± 0.07	1.57 ± 0.07	0.71	0.54 ± 0.01	5.32 ± 0.07	52.41 ± 0.35	108.54 ± 0.67
13	96440-01-03-06	866.2909	2.30 ± 0.08	1.63 ± 0.08	0.52	0.58 ± 0.01	6.14 ± 0.07	56.66 ± 0.40	118.43 ± 0.73
14	96440-01-04-01	872.0858	2.22 ± 0.06	1.54 ± 0.07	0.41	0.52 ± 0.01	4.90 ± 0.06	46.96 ± 0.29	93.05 ± 0.57
15	96440-01-04-03	869.2781	2.26 ± 0.07	1.58 ± 0.07	0.53	0.55 ± 0.01	5.44 ± 0.07	51.59 ± 0.35	106.77 ± 0.65
16	96440-01-04-04	871.2958	2.35 ± 0.08	1.69 ± 0.07	0.55	0.61 ± 0.01	7.16 ± 0.08	48.77 ± 0.33	118.72 ± 0.66
17	96440-01-04-05	873.0034	2.27 ± 0.04	1.53 ± 0.07	0.49	0.56 ± 0.01	4.78 ± 0.07	80.36 ± 0.41	100.79 ± 0.74
18	96440-01-04-06	875.6732	2.31 ± 0.08	1.65 ± 0.08	0.56	0.59 ± 0.01	6.55 ± 0.07	46.82 ± 0.32	110.27 ± 0.61
19	96440-01-05-00	876.8402	2.27 ± 0.04	1.55 ± 0.08	0.49	0.55 ± 0.01	5.10 ± 0.07	72.06 ± 0.34	91.93 ± 0.64
20	96440-01-05-01	877.4295	2.32 ± 0.07	1.63 ± 0.06	0.59	0.60 ± 0.01	6.21 ± 0.07	44.29 ± 0.29	101.79 ± 0.58
21	96440-01-05-02	877.8880	2.24 ± 0.05	1.54 ± 0.07	0.57	0.53 ± 0.01	5.00 ± 0.06	53.36 ± 0.30	91.42 ± 0.59
22	96440-01-05-03	879.5833	2.24 ± 0.07	1.56 ± 0.07	0.54	0.54 ± 0.01	5.21 ± 0.06	38.17 ± 0.25	82.47 ± 0.49
23	96440-01-05-04	880.6295	2.27 ± 0.08	1.59 ± 0.07	0.70	0.55 ± 0.01	5.67 ± 0.07	38.00 ± 0.26	86.76 ± 0.48
24	96440-01-05-05	882.6413	2.23 ± 0.08	1.56 ± 0.08	0.57	0.53 ± 0.01	5.20 ± 0.07	44.76 ± 0.30	83.84 ± 0.53
25	96440-01-06-00	883.5596	2.27 ± 0.07	1.58 ± 0.07	0.59	0.56 ± 0.01	5.56 ± 0.07	44.31 ± 0.28	84.61 ± 0.51
26	96440-01-06-01	884.6704	2.18 ± 0.05	1.45 ± 0.07	0.88	0.49 ± 0.01	3.79 ± 0.05	35.19 ± 0.21	61.04 ± 0.40
27	96440-01-06-02	885.8371	2.19 ± 0.05	1.44 ± 0.07	0.60	0.50 ± 0.01	3.75 ± 0.05	36.20 ± 0.20	59.89 ± 0.40
28	96440-01-06-03	886.8228	2.22 ± 0.05	1.50 ± 0.08	0.73	0.52 ± 0.01	4.38 ± 0.06	47.34 ± 0.24	65.07 ± 0.42
29	96440-01-06-04	888.2533	2.20 ± 0.06	1.42 ± 0.07	0.65	0.50 ± 0.01	3.48 ± 0.05	29.03 ± 0.17	52.16 ± 0.35
30	96440-01-07-00	890.0729	2.22 ± 0.07	1.44 ± 0.08	0.81	0.52 ± 0.01	3.72 ± 0.05	26.97 ± 0.17	48.77 ± 0.32
31	96440-01-07-01	891.1884	2.26 ± 0.08	1.54 ± 0.08	0.85	0.55 ± 0.01	4.94 ± 0.06	25.15 ± 0.17	54.51 ± 0.32
32	96440-01-07-02	892.2633	2.25 ± 0.09	1.54 ± 0.08	0.41	0.54 ± 0.01	4.99 ± 0.06	24.98 ± 0.17	53.47 ± 0.31
33	96440-01-07-03	893.4686	2.12 ± 0.06	1.40 ± 0.08	0.67	0.45 ± 0.01	3.28 ± 0.05	29.27 ± 0.18	43.78 ± 0.31
34	96440-01-07-04	894.3870	2.15 ± 0.05	1.33 ± 0.07	0.84	0.47 ± 0.01	2.54 ± 0.04	21.01 ± 0.13	32.87 ± 0.23
35	96440-01-07-05	895.2340	2.17 ± 0.06	1.37 ± 0.08	0.72	0.48 ± 0.01	2.95 ± 0.04	21.07 ± 0.13	34.92 ± 0.23
36	96440-01-07-06	896.1426	2.07 ± 0.04	1.29 ± 0.08	0.80	0.41 ± 0.01	2.18 ± 0.04	28.16 ± 0.15	30.50 ± 0.25
37	96440-01-08-00	898.1645	2.06 ± 0.04	1.10 ± 0.04	1.35	0.41 ± 0.01	0.97 ± 0.02	14.75 ± 0.09	17.27 ± 0.15
38	96440-01-08-02	899.0077	2.12 ± 0.06	1.22 ± 0.07	1.54	0.45 ± 0.01	1.65 ± 0.03	15.29 ± 0.11	19.47 ± 0.16
39	96440-01-08-03	900.3845	2.12 ± 0.08	1.20 ± 0.06	1.31	0.45 ± 0.01	1.53 ± 0.03	11.34 ± 0.08	15.41 ± 0.13
40	96440-01-08-04	901.2278	2.10 ± 0.06	1.23 ± 0.07	0.92	0.44 ± 0.01	1.75 ± 0.03	12.26 ± 0.09	15.87 ± 0.12
41	96440-01-08-05	902.0756	2.02 ± 0.05	1.14 ± 0.06	0.78	0.39 ± 0.01	1.15 ± 0.02	11.22 ± 0.08	12.26 ± 0.11
42	96440-01-08-06	903.1209	1.94 ± 0.05	1.03 ± 0.05	0.86	0.34 ± 0.01	0.63 ± 0.01	7.86 ± 0.06	7.10 ± 0.08
43	96440-01-09-00	904.0978	2.29 ± 0.10	1.17 ± 0.06	1.56	0.57 ± 0.01	1.34 ± 0.03	4.44 ± 0.05	5.74 ± 0.05
44	96440-01-09-02	906.0508	9.22 ± 3.94	1.81 ± 0.06	0.93	9.85 ± 0.72	9.19 ± 0.17	2.15 ± 0.08	3.47 ± 0.03
45	96440-01-09-03	907.3148	15.80 ± 7.33	1.66 ± 0.05	1.17	15.40 ± 0.96	6.67 ± 0.12	1.56 ± 0.05	1.95 ± 0.02
46	96440-01-09-04	908.2906	9.27 ± 2.57	1.49 ± 0.06	1.02	9.92 ± 0.49	4.37 ± 0.09	1.69 ± 0.04	1.22 ± 0.01
47	96440-01-09-05	909.0731	6.65 ± 1.80	1.30 ± 0.09	1.07	6.44 ± 0.27	2.27 ± 0.06	1.56 ± 0.03	0.75 ± 0.01
48	96440-01-09-08	904.3096	2.31 ± 0.10	1.21 ± 0.06	1.35	0.58 ± 0.01	1.63 ± 0.03	3.95 ± 0.04	5.86 ± 0.05
49	96440-01-09-10	908.0061	7.94 ± 2.18	1.51 ± 0.11	1.03	8.26 ± 0.52	4.63 ± 0.13	2.05 ± 0.06	1.40 ± 0.02
50	96440-01-09-11	909.2486	7.83 ± 2.14	1.35 ± 0.12	0.84	8.11 ± 0.59	2.78 ± 0.10	1.41 ± 0.05	0.72 ± 0.01
51	96440-01-09-12	910.9905	3.72 ± 3.72	1.11 ± 0.91	0.61	2.09 ± 0.72	0.76 ± 0.27	0.45 ± 0.07	0.16 ± 0.03

<sup>a</sup> Hardness parameters are obtained using the flux ratio of two different energy ranges;  $L(10 - 30 \text{ keV})/L(3 - 10 \text{ keV})$ . The parameters for diskbb component are multiplied by  $10^2$  because of low values

<sup>b</sup> Unabsorbed flux of the bbody component in units of  $10^{-10} \text{ erg s}^{-1} \text{ cm}^{-2}$ .

<sup>c</sup> Unabsorbed flux of the diskbb component in units of  $10^{-10} \text{ erg s}^{-1} \text{ cm}^{-2}$ .

**APPENDIX C:** Best fit parameters of *black body radiation + comptonisation + disk black body + Gauss* model of RXTE/PCA data during the 2000 and the 2011 outbursts of Aql X-1

**Table C.1 :** Best fit parameters of *black body radiation + comptonisation + disk black body + Gauss* model for the 2000 outburst of RXTE/PCA data.

Obs Number	$kT_{bbody}$ (keV)	$\tau$	$\chi^2$	Hardness <sup>a</sup> bbody	Flux <sup>b</sup> <sub>bbody</sub>
1	2.36 ± 0.30	2.72 ± 0.67	0.95	2.77 ± 0.10	1.84 ± 0.02
2	2.80 ± 0.21	2.49 ± 0.30	1.13	3.30 ± 0.09	3.37 ± 0.03
3	2.77 ± 0.21	2.76 ± 0.26	1.03	3.49 ± 0.08	5.10 ± 0.04
5	4.68 ± 0.30	2.17 ± 0.34	1.02	5.45 ± 0.08	22.59 ± 0.11
16	2.25 ± 0.03	0.13 ± 0.09	0.52	0.58 ± 0.01	40.97 ± 0.20
28	2.25 ± 0.04	0.11 ± 0.10	0.49	0.56 ± 0.01	28.96 ± 0.14
39	2.00 ± 0.03	0.06 ± 0.02	0.93	0.48 ± 0.01	16.36 ± 0.07
48	3.48 ± 0.45	1.63 ± 0.51	1.40	3.27 ± 0.13	4.06 ± 0.05
49	2.82 ± 0.40	2.83 ± 0.22	0.91	3.64 ± 0.11	4.00 ± 0.04
50	3.75 ± 0.65	2.30 ± 0.88	0.93	3.71 ± 0.19	3.71 ± 0.07
51	2.72 ± 0.48	2.84 ± 0.85	0.67	3.47 ± 0.15	2.49 ± 0.04
52	2.55 ± 0.56	2.98 ± 0.20	0.78	3.29 ± 0.15	1.07 ± 0.02

<sup>a</sup> Hardness parameters are obtained using the flux ratio of two different energy ranges;  $L(10 - 30 \text{ keV})/L(3 - 10 \text{ keV})$ .

<sup>b</sup> Unabsorbed flux of the bbody component in units of  $10^{-10} \text{ erg s}^{-1} \text{ cm}^{-2}$ .

**Table C.2 :** Same as Table C.1 but for the 2011 outburst.

Obs Number	$kT_{bbody}$ (keV)	$\tau$	$\chi^2$	Hardness <sup>a</sup> bbody	Flux <sup>b</sup> <sub>bbody</sub>
1	2.83 ± 0.31	2.57 ± 0.45	1.18	3.36 ± 0.07	5.27 ± 0.04
2	4.17 ± 0.42	3.89 ± 0.80	1.02	4.29 ± 0.06	14.16 ± 0.06
7	2.19 ± 0.03	0.09 ± 0.08	0.74	0.52 ± 0.01	55.90 ± 0.27
19	2.21 ± 0.03	0.06 ± 0.04	0.86	0.54 ± 0.01	73.73 ± 0.28
30	2.06 ± 0.05	0.07 ± 0.03	0.75	0.51 ± 0.01	27.71 ± 0.14
44	3.60 ± 0.60	2.66 ± 0.60	0.91	3.67 ± 0.12	3.64 ± 0.04
45	3.17 ± 0.47	3.15 ± 0.48	1.32	3.55 ± 0.04	3.06 ± 0.02
46	2.70 ± 0.30	2.68 ± 0.17	1.17	3.28 ± 0.08	2.40 ± 0.02

<sup>a</sup> Hardness parameters are obtained using the flux ratio of two different energy ranges;  $L(10 - 30 \text{ keV})/L(3 - 10 \text{ keV})$ .

<sup>b</sup> Unabsorbed flux of the bbody component in units of  $10^{-10} \text{ erg s}^{-1} \text{ cm}^{-2}$ .



## CURRICULUM VITAE



**Name Surname:** Can GÜNGÖR

**Place and Date of Birth:** İzmir/TURKEY 12.10.1982

**Address:** Technical University of İstanbul, Faculty of Art and Science, Department of Physics Engineering, L1-303, 34469, Maslak İstanbul

**E-Mail:** gungor.can@gmail.com; gungorcan@itu.edu.tr

**B.Sc.:** Department of Astronomy and Space Sciences, Science Faculty, Ege University

**M.Sc.:** Astrophysics Programme, Department of Astronomy and Space Sciences, Science Faculty, Ege University

## PUBLICATIONS/PRESENTATIONS ON THE THESIS

### *Publications*

- Classification and spectral evolution of outbursts of Aql X–1. **Güngör, Can;** Güver, Tolga; Ekşi, K. Yavuz. (2014MNRAS.439.2717G)
- Partial accretion in the propeller stage of accreting millisecond X-ray pulsar Aql X–1. **Güngör, C.,** Ekşi, K. Y., Göğüş, E., Güver, T., Neuhäuser, R., & Hambaryan, V., *in preperation*

### *Presentations*

- Poster presentation titled “Partial Accretion in the Propeller Stage of Accreting Millisecond X-ray Pulsars” in the meeting: “The 41st COSPAR Scientific Assembly”, İstanbul, Turkey (2016).
- Poster presentation titled “Partial Accretion in the Propeller Stage of Accreting Millisecond X-ray Pulsars” in the meeting: “The European Week of Astronomy and Space Science – The physics of accretion on compact objects”, Athens, Greece (2016).
- Oral presentation titled “The Partial Accretion onto Neutron Stars in the Propeller Stage” at Institute of Astronomy and Astrophysics of Tübingen University, Germany (2016).
- Oral presentation titled “The Partial Accretion onto Neutron Stars in the Propeller Stage” at Astrophysikalisches Institut und Universitäts–Sternwarte, Jena, Germany (2015).

- Oral presentation titled “Classification and Spectral Evolution of Outbursts of Aql X–1” at Astrophysikalisches Institut und Universitäts–Sternwarte, Jena, Germany (2015).
- Poster presentation titled “Classification and Spectral Evolution of Outbursts of Aql X–1” in the meeting: “The 40th COSPAR Scientific Assembly”, Moscow, Russia (2014).
- Poster presentation titled “Aquila X–1 in outburst” in the meeting: “The European Week of Astronomy and Space Science – The physics of accretion on compact objects”, Turku, Finland (2013).

## OTHER PUBLICATIONS/PRESENTATIONS

### *Publications*

- The ultraluminous X–ray source NuSTAR J095551+6940.8: a magnetar in a high-mass X–ray binary. Ekşi, K. Y.; Andaç, İ. C.; Çıkıntoğlu, S.; Gençali, A. A.; **Güngör, C.**; Öztekin, F. (2015MNRAS.448L..40E)
- What does a measurement of mass and/or radius of a neutron star constrain: Equation of state or gravity? Ekşi, Kazım Yavuz; **Güngör, Can**; Türkoglu, Murat Metehan. (2014 PhRvD..89f3003E)
- Possible ambiguities in the equation of state for neutron stars. Cheoun, Myung-Ki; Miyatsu, Tsuyoshi; Ryu, C. Y.; Deliduman, Cemsinan; **Güngör, Can**; Keleş, Vildan; Kajino, Toshitaka; Mathews, Grant J. (2014AIPC.1594..414C)
- Neutron stars in a perturbative  $f(R)$  gravity model with strong magnetic fields. Cheoun, Myung-Ki; Deliduman, Cemsinan; **Güngör, Can**; Keleş, Vildan; Ryu, C. Y.; Kajino, Toshitaka; Mathews, Grant J. (2013JCAP...10..021C)
- A new low-mass eclipsing binary: NSVS 02502726. Çakırlı, Ö.; İbanoğlu, C.; **Güngör, C.** (2009NewA 14 496C)

### *Presentations*

- Oral presentation titled “Analytical Representation for Equations of State of Dense Matter” in the “Physics of stars” summer school in International Advanced Research Schools in Physics, Marmaris, Turkey (2011).
- Poster presentation titled “Analytical Representation for Equations of State of Dense Matter” in the meeting: “Advances in Computational Astrophysics: methods, tools and outcomes”, Cefalu, Italy (2011).